ABSTRACT

Title of Document:	Carbon Nanotube Electronics: Growth, Imaging and Electronic Properties
	Todd Harold Brintlinger, Doctor of Philosophy, 2005
Directed By:	Michael Sears Fuhrer, Associate Professor, Department of Physics

This dissertation focuses on growth, fabrication, and electronic characterization of carbon nanotube (CNT) devices. A technique for imaging CNTs on insulating substrates with the scanning electron microscope (SEM) will be described. This technique relies on differential charging of the CNT relative to the surrounding insulator. In addition, it is not only quicker than using scanning probe microscopy (SPM), but is also useful for identifying conducting pathways within an assortment of CNTs and metallic contacts.

CNT field effect transistors (FETs) fabricated on strontium titanate gate dielectric show transconductances normalized by channel width of 8900 S/m, greatly exceeding that in Si FETs. Intriguingly, the transconductance cannot be explained within the conventional FET or Schottky-barrier models. To explain this, it is proposed that there is Schottky-barrier lowering due to high electric fields at the CNT/contact interface.

Exploring novel CNT-FET lithography, I demonstrate focused electron beam induced deposition (FEBID) of pure gold for CNT device electrodes. In examination of the CNT/electrode interface, equivalence between FEBID leads and leads

deposited using conventional electron beam lithography is found with the majority device resistance in the CNT.

Lastly, CNTs are suspended across wide trenches (>100μm). These trenches are formed without lithography or etching and have metallic leads on either side of the trench for electrical transport measurements. Using a mechanical probe as a mobile gate, electrical transport can be performed on these suspended CNT devices, which show minimal hysteresis consistent with the absence of charge trapping.

CARBON NANOTUBE DEVICES: GROWTH, IMAGING, AND ELECTRONIC PROPERTIES

by

Todd Harold Brintlinger

Dissertation submitted to the Faculty of the Graduate School of the
University of Maryland, College Park, in partial fulfillment
of the requirements for the degree of
Doctor of Philosophy
2005

Advisory Committee:

Professor Michael S. Fuhrer, Chair
Professor Steven Anlage
Professor Chris Lobb
Professor Ellen Williams
Professor John Melngailis, Dean's Representative

Foreword

This dissertation is the culmination of five years of work in Professor Michael Fuhrer's laboratory at the University of Maryland. It represents published and unpublished experiments completed at the University of Maryland along with other laboratories, especially Ecole Polytechnique Federale de Lausanne (EPFL) with the group of Patrik Hoffmann.

There is an introduction to carbon nanotubes in Chapter 1. While not necessary for those already familiar with the subject, it is included here for the reader with no background in carbon nanotubes who is familiar with basic condensed matter physics. Chapter 2 continues with introductory information concerning experimental techniques used in this dissertation. It also can most likely be skipped by readers that already have a working knowledge of basic carbon nanotube research.

Chapters 3 to 6 present the research undertaken toward completion of this dissertation. This work relies on a moderate understanding of basic scanning electron and probe microscopy as well as standard device physics concerning field effect transistors. Chapter 6 represents the only unpublished work of the dissertation and is more exploratory than the other chapters which represent more complete stories.

Additional information concerning experimental techniques, not outlined in the main body, can be found in the Appendices. Also, to avoid redundancy, some material which appears in the thesis of Tobias Dürkop is not repeated here. The papers published by Professor Fuhrer's group are available at, http://www.physics.umd.edu/condmat/mfuhrer/pubs.htm.

Dedication

To my mother Nancy Ryan, my brother Kirk, my father Dan, and my grandparents, the Ridenours and the Brintlingers.

Acknowledgements

I would like to thank my advisor, Professor Michael Fuhrer, for making this dissertation possible. His availability and expertise were indispensable to my development as a scientist. He has also been a good friend. In numerous lunchtime conversations and hallway meetings, I experienced the excitement that makes physics enjoyable. I should also apologize to Cynthia, Michael's wife, for all the times I made him late for dinner. They are both wonderful people, and they put on the best Halloween parties. It is fitting this dissertation would be written in the autumn.

I would like to thank all the members of my committee: Professors Steven Anlage, Ellen Williams, Chris Lobb, and John Melngailis, for taking the time to read this dissertation and for doing me the honor of serving on my committee. John Melngailis, in particular, has been an important part of my graduate career, coauthoring two of the papers in this work and always providing his time and equipment when it would help.

Thanks also to all the members of the Fuhrer group, past and present: Yung-Fu Chen, Enrique Cobas, Tobias Dürkop, Gokhan Esen, Adrian Southard, David Tobias, Dan Lenski, Tareq Ghanem, Anthony Ayari, Byong M. Kim, and Stephanie Getty. They filled my time in the lab with their humor, talents, and patience.

Obviously, all my collaborators were important to the experiments in this dissertation: John Barry for helping with the SEM in Chapter 3; the Motorola group in Arizona, for supplying the $SrTiO_3$, and Haimei Zheng, for the TEM images, in Chapter 4; and the groups of Patrik Hoffmann, for the gold deposition, and Pascal Doppelt, for the inorganic gold precursor, in Chapter 5. Erik Hobbie and Alma

Wickenden helped with some of the material in Chapter 6. I also worked with Atif Imtiaz on CNTs in a scanning microwave microscope in work not presented here.

Professor Dennis Drew gave me a chance to work in the lab before beginning with Michael. Present and former members of his group: Don Schmadel, Jeff Simpson, Greg Jenkins, and Matt Grayson helped me get started with experimental physics at Maryland.

The support I've received from all the departments, centers, and offices at Maryland has been wonderful: Russ Wood, Jane Hessing, Margaret Lukomska, Bob Dahms, Jesse Anderson, Al Godinez, George Butler, and Lorraine DeSalvo contributed in one way or another along with countless others.

Bradford Hill, Joe Philips, Rogerio de Sousa, Maria Aranova, Frederick Strauch, Rebecca Lippmann, and Edward Burns were all good friends as fellow graduate students at the beginning of my time at Maryland. Their help and support during introductory graduate classes made my later work possible, as did Susan Grasch. Analogously, my friends and teachers in Illinois: Michael Campbell, Marcus Slavenas, Matthew Walsh, Kory Charland, Professors George Gollin, Steve Errede, and Jeremiah Sullivan at the University of Illinois; and Charles "Chuck" Force and Julia Heiden at Eisenhower High School laid all the groundwork for my coming to the University of Maryland.

Stephanie Getty has supported me and made all the rest of my life in Maryland (and the District) a joy for the last several years. She is a wonderful woman and talented scientist and deserves my thanks for her help toward completion of this dissertation.

Lastly, my family and friends in Decatur, Illinois, were always there for me, and I want to acknowledge them here.

Table of Contents

List of Tables

List of Figures

Chapter 1: Introduction to Carbon Nanotubes

Carbon nanotube history and buckminsterfullerenes

Carbon nanotubes (CNTs) are extended hexagonal lattices of carbon atoms wrapped into seamless cylinders.[1] Their discovery followed years of intense research into a class of carbon compounds, buckminsterfullerenes, which added to a historically short list of known elemental compounds of carbon: graphite and diamond. In 1995, the discovery of buckminsterfullerenes garnered a Nobel prize.[2] A model of the C_{60} molecule, one of the first buckminsterfullerenes discovered, is shown in Figure 1.

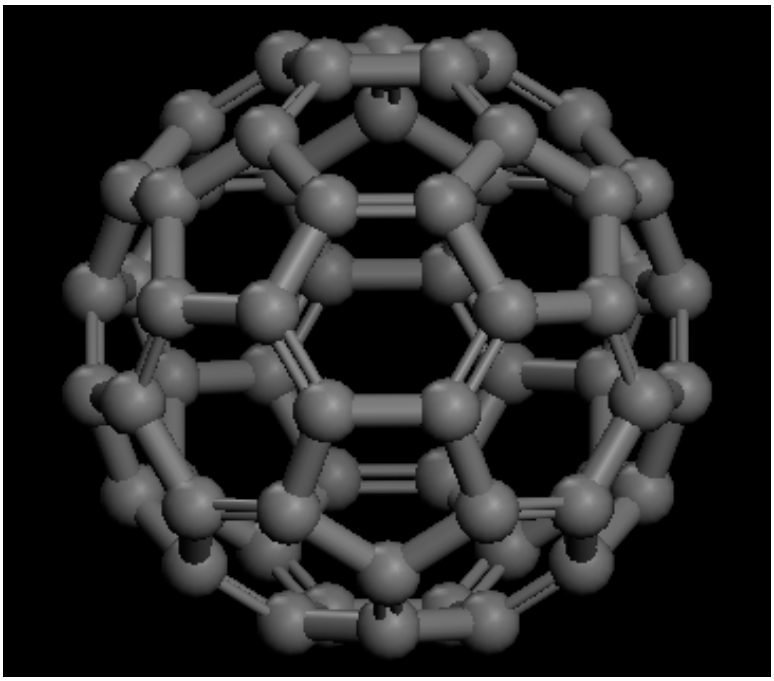

Figure 1. Schematic of the C_{60} molecule: Balls represent carbon atoms. Sticks represent orbital electrons. All carbon atoms have sp^2-hybridized orbitals making C_{60} a very chemically and mechanically stable molecule.

To put carbon nanotubes into context regarding buckminsterfullerenes, one simply has to imagine 'cutting' a C_{60} molecule in half and inserting a single rolled-up sheet of graphite between the half-spheres to get a carbon nanotube. A model of this is shown in Figure 2 along with typical length scales for CNT length and diameter. Although the discovery of CNTs is associated with fullerene caps, their presence is not presently an important component of CNT research. An exception is when CNTs are used as the active component in field emission devices, in which case the caps affect field emission behavior. Also of note, real CNTs often have capping structures that radically diverge from the fullerene molecules depicted here, with 'square edges' and sharp corners being commonplace in transmission electron microscope (TEM) images.[3,4] This feature of CNT research will not be treated here, but it is mentioned for completeness.

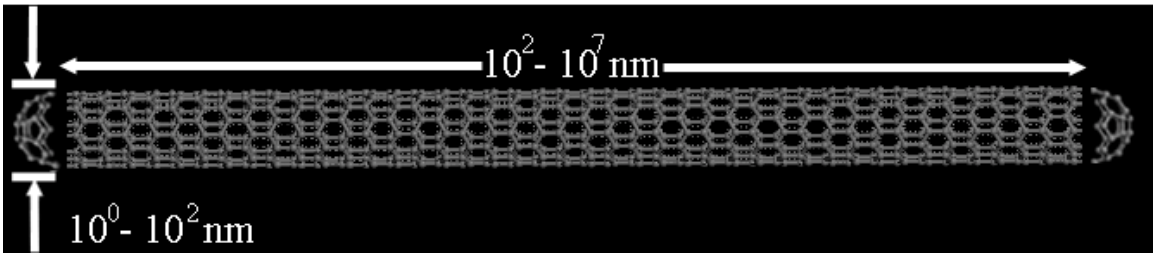

Figure 2. A depiction of an (8,0) carbon nanotube showing fullerene molecules as 'caps' to the cylindrical lattice in the middle. Experimentally realizable length scales are shown for length and diameter. The larger diameters are typical of multi-walled carbon nanotubes, while the longer lengths tend to be associated with single-walled carbon nanotubes. Note that 10 million -to-one aspect ratios are possible.

The experimental realization of this idea was verified by Iijima and was published contemporaneously with a group of theoretical papers that not only suggested the existence of such extended carbon lattices, but predicted some of their physical properties.[5-8] Upon further research following this discovery, it was

indicated that such 'carbon nanotubes' had been seen in transmission electron microscope images dating back to the 1970's albeit without realizing the structures were perfectly wrapped sheets of graphene.[9-11] While assignment of first recognition is an ongoing process, the complex behavior which results from such a readily defined and easily manufactured system is not. Carbon nanotubes are some of the most intensely researched materials of the last decade. This dissertation continues that research, particularly as regards the growth of carbon nanotubes, their behavior in scanning electron microscopes, and as channels in carbon nanotube field effect transistors.

Classification and electronic properties

To understand the discussions of the following chapters and in carbon nanotube research in general, it is useful to begin with the classification system used for carbon nanotubes. This nomenclature naturally leads into carbon nanotube electronic properties. The classification of carbon nanotubes begins with the definition of a unit cell based on an extended hexagonal carbon lattice. Following the formalism depicted in Figure 3 and Ref. 7, unit vectors, $\boldsymbol{a_1}$ and $\boldsymbol{a_2}$, are defined within a single sheet of graphite, also called graphene. A similar formalism is also laid out in Ref. 8. A carbon nanotube is formed by first extending these vectors to another point, $\boldsymbol{b} \equiv$ *circumferential vector*, within the graphene sheet such that $\boldsymbol{b} = \boldsymbol{n}\,\boldsymbol{a_1} + \boldsymbol{m}\,\boldsymbol{a_2}$, designated ($\boldsymbol{n}$, $\boldsymbol{m}$). Thus, the vector $\boldsymbol{b}$ shown in Figure 3 corresponds to an ($\boldsymbol{n}$, $\boldsymbol{m}$) value of (8,2). The vectors (8,0) and (5,5) are also displayed. This point is then folded onto the origin, imposing a new boundary condition and transforming the two-

dimensional graphene sheet into a one-dimensional carbon nanotube. If the graphene sheet is taken as infinite, it is understood that the resulting carbon nanotube would be composed of smooth, infinite cylindrical tubes of carbon atoms.

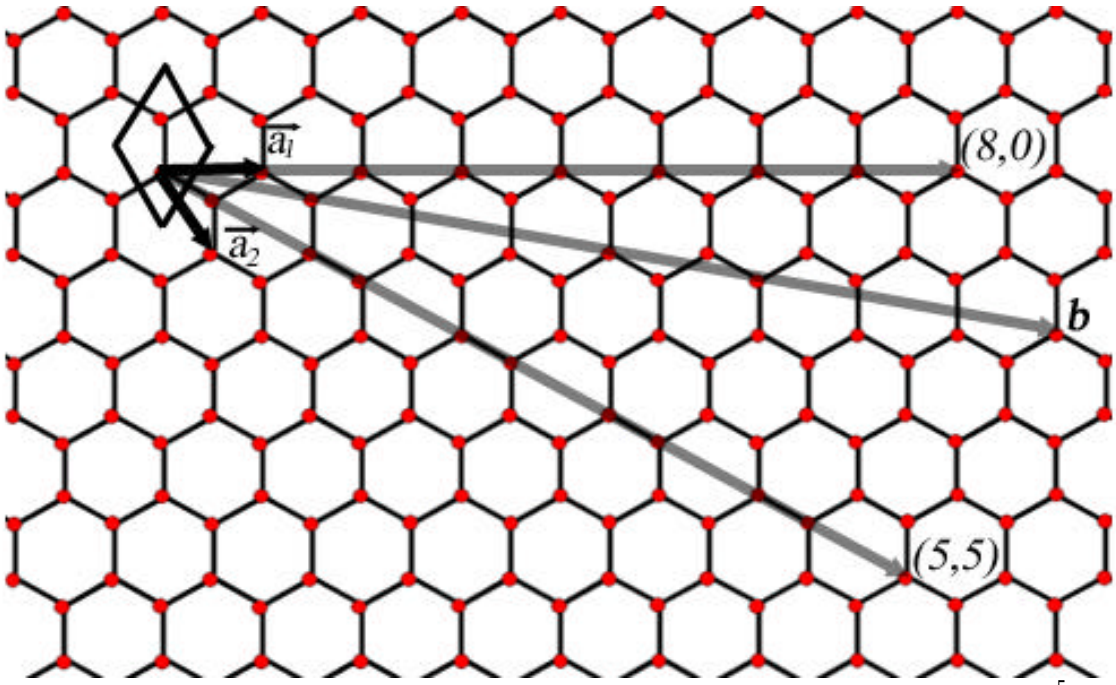

Figure 3. Hexagonal graphene sheet for classification of carbon nanotubes following Saito et al[5]: The diamond depicts the graphene unit cell, while the arrows a_1 and a_2 depict the unit vectors. Carbon nanotubes are classified by extending the unit vectors $n*a_1$ and $m*a_2$, where n and m are integers, to a given point, b, and then folding it back on to the starting point. This defines the carbon nanotube circumference. The nanotube with $b = n*a_1$ and $m*a_2$ is labeled (n,m).

This wrapping vector directly gives the diameter of the nanotube with

$$d = a\frac{\sqrt{3}}{p}\sqrt{n^2 + nm + m^2} \qquad (2.1)$$

where a = 0.142 nm is the carbon-carbon spacing. The carbon nanotube is then defined in terms of this wrapping vector; thus, the (8, 0) vector displayed in Figure 3 corresponds to the CNT pictured in Figure 2 while Figure 4 depicts a (9,0) nanotube. One can count the number of carbon rings wrapping the circumference to see the

connection between a vector and its corresponding carbon nanotube. Both these vectors are of a special type called 'zigzag' carbon nanotubes which receive their name from the 'zigzag' shape along the (x,0) vectors. The (5,5) vector, and nanotube, is also displayed. Often studied theoretically due to its small unit cell this is one of the 'armchair' carbon nanotubes, where $\boldsymbol{n} = \boldsymbol{m}$, so-called due to the armchair pattern of carbon-carbon bonds along the vector direction.

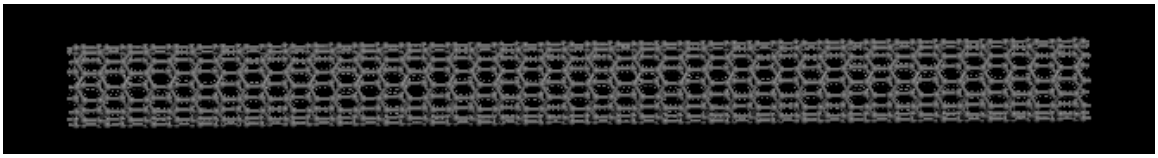

Figure 4. A (9,0) carbon nanotube without the capping fullerenes depicted in Figure 2.

The choice of this vector, and thus the chirality of the CNT, defines the electronic properties of the carbon nanotube. Carbon nanotube behavior divides into three classes: metallic, small-gap semiconducting, and semiconducting. This behavior is determined by the wrapping vector ***(n,m)***, or more specifically the value of $\boldsymbol{n - m}$. For $\boldsymbol{n - m = 0}$, metallic behavior is observed.[6-8] For $\boldsymbol{n - m = j*3}$ where $\boldsymbol{j}$ is a non-zero integer, a small-gap semiconductor or semi-metallic nanotube with a small gap, < 20 mV, is observed.[8] For $\boldsymbol{n - m \neq j*3}$, semiconducting behavior with a semiconducting gap, $\boldsymbol{E_g}$ = 700 meV/[$\boldsymbol{d}$($\boldsymbol{n}$,$\boldsymbol{m}$)] where $\boldsymbol{d}$ is the diameter of the CNT in nanometers.[6-8]

The folding of a vector back onto the origin is the equivalent of establishing an additional boundary condition. This condition requires that the electron wavefunction be single-valued at the origin. This constraint equivalently reduces the system from two dimensions to one. As will be seen in the subsequent chapters, this

will have important consequences for the electrical transport in carbon nanotubes. To understand these consequences, one can begin with the two-dimensional dispersion relation for an sp^2-bonded graphene lattice, just as one begins with this lattice in a geometrical interpretation. This relation was originally derived by P.R. Wallace in 1947 as the basis for an eventual description of graphite,[12] with the interaction between sheets of graphene being added after the description of the simple, two-dimensional band structure. At low energies near the band edge, the dispersion relation in two dimensions can be written:

$$E_{2D}(k_x, k_y) = \pm g_0(1 + 4\cos(\sqrt{3}k_x a/2)\cos(k_y a/2) + 4\cos^2(k_y a/2))^{1/2} \quad (2.2)$$

where $\boldsymbol{k_x}$ and $\boldsymbol{k_y}$ are the wavevectors, g_0 is a coupling constant, and $\boldsymbol{a}$ is the lattice parameter. Plotted in a three-dimensional mapping at low energies, this corresponds to a two-dimensional band structure as depicted in Figure 5. One sees six cones meeting six inverted cones meeting at the points of a hexagon.

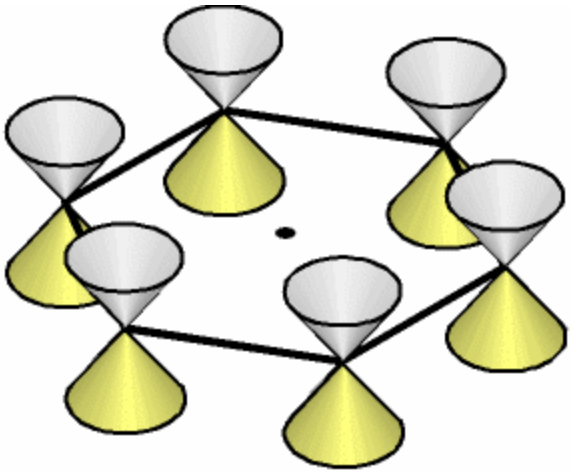

Figure 5. Schematic depicting two-dimensional band structure defined in Equation (2.2).

The boundary condition/wrapping described above is the equivalent of making slices through this band structure and projecting the slice into one-dimension as seen in Figure 6. If slices are made such that they intersect the apices of the cones, the 'crossing' is preserved and the resulting single-walled carbon nanotube is a metal; if the cut avoids the apices, the CNT is a semiconductor and results in Figure 7. The third class of nanotubes is small-gap, or semi-metallic, carbon nanotubes. These have $n-m = j*3$, but $\neq 0$. These are metallic in the simple picture above; however, more careful analysis[7,13] shows that the points of intersection of the cones in Figure 5 are shifted slightly due to curvature of the graphene sheet, introducing a small bandgap. Here, one can think of the curvature of these chiral nanotubes as introducing a small-gap (5-20 meV) to the nanotubes which remains well below room temperature thermal energies.

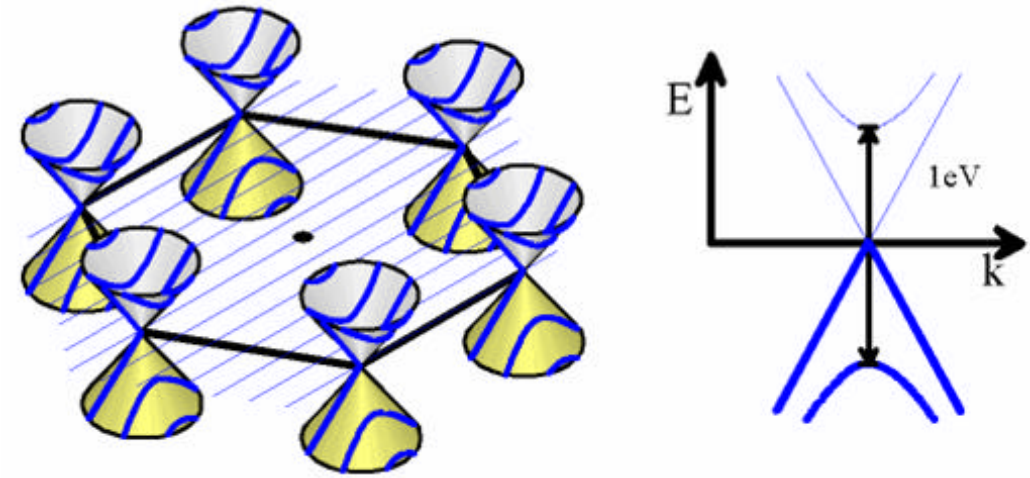

Figure 6. Two dimensional band structure of graphene with slices representing wrapping of vector to make carbon nanotube. Blue slices result in a metallic one-dimensional band structure depicted on the right.

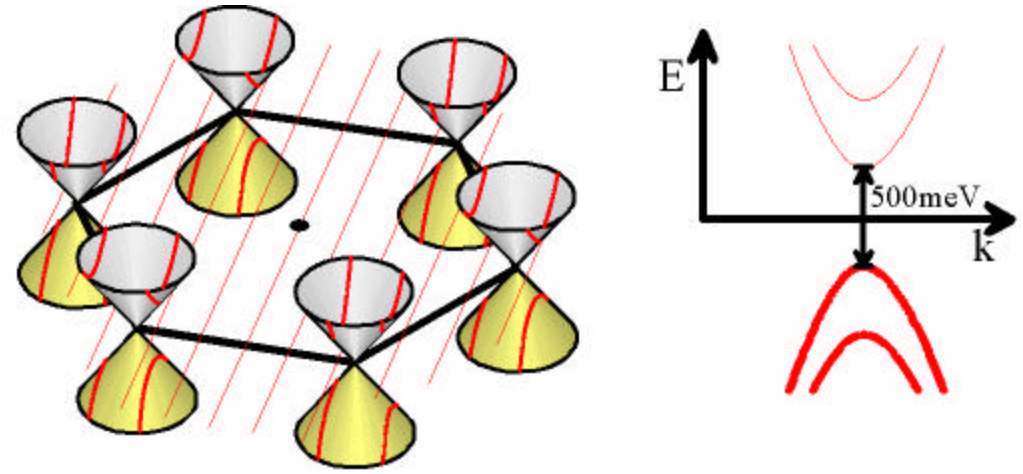

Figure 7. Two dimensional band structure of graphene with slices representing wrapping of vector to make carbon nanotube. Red slices result in a semi-conducting one-dimensional band structure depicted on the right.

Thus far, investigation of the electronic properties of carbon nanotubes has led to an essentially *one-dimensional* description. This allows one to use the Landauer-Büttiker formalism which is common in mesoscopic physics.[14,15] Usually confined to studies of high-purity heterostructures of GaAs, mesoscopic physics describes systems that bridge the divide between atomic and macroscopic systems; thus, the use of mesoscopic vs. nanoscopic to describe systems tends to have more to do with materials than with the underlying physics.

Following Datta's treatment,[14] conductance is found by first considering two conductors with transmission probability T_1 and T_2. Placed in series and considering the reflections *between* conductors as seen in Figure 8, one can begin to develop an expression for the total conduction, T_{12}.

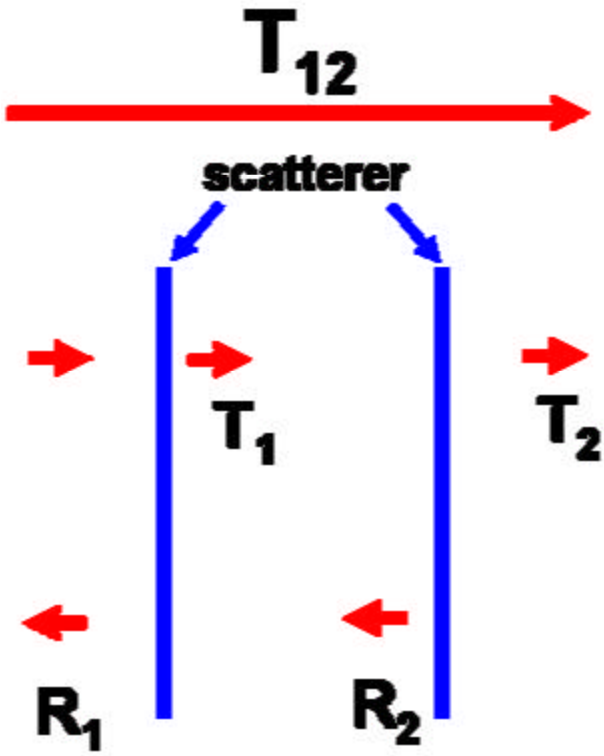

Figure 8. Schematic describing total transmission coefficient, T_{12}, in a one-dimensional conductor with two scatterers. The text describes the composition of this coefficient in terms of the transmission and reflection coefficients, T_1/T_2 and R_1/R_2, of each individual scatterer.

Thus, the total transmission T_{12} can be written

$$T_{12} = T_1T_2 + T_1T_2R_1R_2 + T_1T_2R_1^2R_2^2 + ... = \frac{T_1T_2}{1-R_1R_2} \tag{2.3}$$

Making use of the relation $T_1 = 1 - R_1$ and $T_2 = 1 - R_2$, this can be rewritten as:

$$\frac{1-T_{12}}{T_{12}} = \frac{1-T_1}{T_2} + \frac{1-T_2}{T_2}$$

This shows that two scattering sites in series add as (1-T)/T. Thus, the transmission probability for N scatterers $T(N)$ is given by:

$$\frac{1-T(N)}{T(N)} = N\frac{1-T}{T} \Rightarrow T(N) = \frac{T}{N(1-T)+T}. \tag{2.4}$$

If one imagines the number of scatterers N in a one-dimensional conductor of length L, the linear density of scatterers n then gives $N = n\,L$. This then makes

$$T(L) = \frac{L_0}{L + L_o} \text{ where } L_0 \equiv \frac{T}{n(1-T)}. \tag{2.5}$$

This length L_0 then corresponds to the mean free path, the distance the electron travels before scattering.

Utilizing the Landauer formalism, conductance G is written

$$G = \frac{2e^2}{h} MT \tag{2.6}$$

where M is the number of modes and T is the transmission probability as above. Thus for long one-dimensional conductors where $L >> L_0$, the conductance can be written

$$\frac{G}{G_0} \approx \frac{L}{L_0}. \tag{2.7}$$

Expressing $G = R^{-1}$, to find the mean free path in a long one-dimensional conductor, one has simply to multiply the total length and resistance and divide by the number of resistance quanta $R_0 = G_0^{-1}$ in the conductor. This allows comparisons between different lengths and types of materials.

Multiwalled carbon nanotubes and bundles of carbon nanotubes

The description has so far concerned an individual single-walled carbon nanotube (SWNT). As seen, this is a fairly simple system to describe theoretically; however, the experimental reality encompasses a larger family of carbon nanotubes than just SWNTs. Nanotubes can also be nested concentrically, giving rise to *multi-walled carbon nanotubes* (MWCNT) as seen in Figure 9. For MWCNTs having only

two shells, the moniker double-walled carbon nanotubes (DWCNTs) has been adopted; an image of these is seen in Figure 9. These have attracted interest as the smallest scale nanoelectromechanical system (NEMS) to date.[16] They are also useful for studying intrinsic SWCNT behavior with differing electronic properties being possible on the inner and outer shells. The larger diameter MWCNTs with numerous shells are of interest more for their mechanical properties, they are very stiff, because the unique one-dimensional properties of SWCNTs become obscured in MWCNTs by shell-shell interactions and defects.

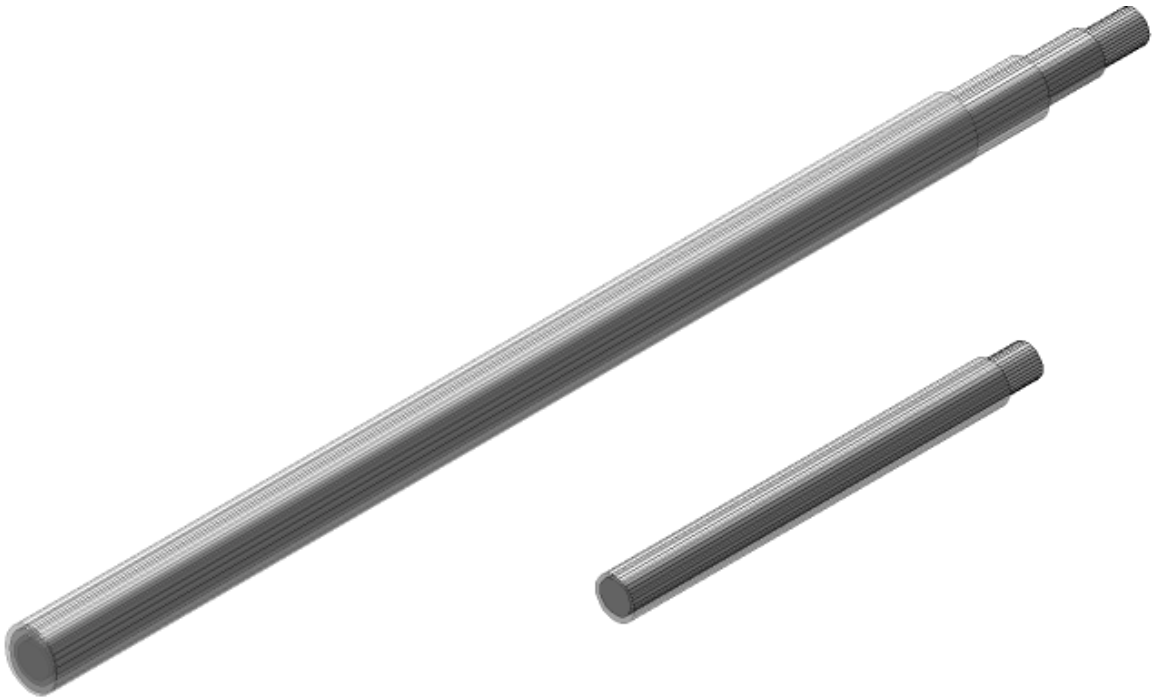

Figure 9. Schematic of a four-walled multiwalled carbon nanotube. Also displayed is the double-walled carbon nanotube: the smallest CNT in which one wall may rotate within or about the other, making a nanoscale bearing.

Yet another type of carbon nanotubes is the bundle. Bundles have larger diameters as do the MWCNTs, making identification through topography alone difficult. As per the nomenclature, bundles do not manifest larger diameters through

concentric shells of CNTs; rather they are overlapping bundles or ropes of nanotubes. This type of CNT makes characterization particularly difficult as the component CNTs in the bundle may change along the length of the bundle. This is demonstrated in Figure 10. If the bundle is investigated at point X for a given property, whether optically, electrically or in some other fashion, it may differ from a similar probe performed at point Y. This problem is ubiquitous to nanotube research and while it is only briefly addressed in the chapter on suspended nanotubes, the reader should be aware that such a difficulty does exist.

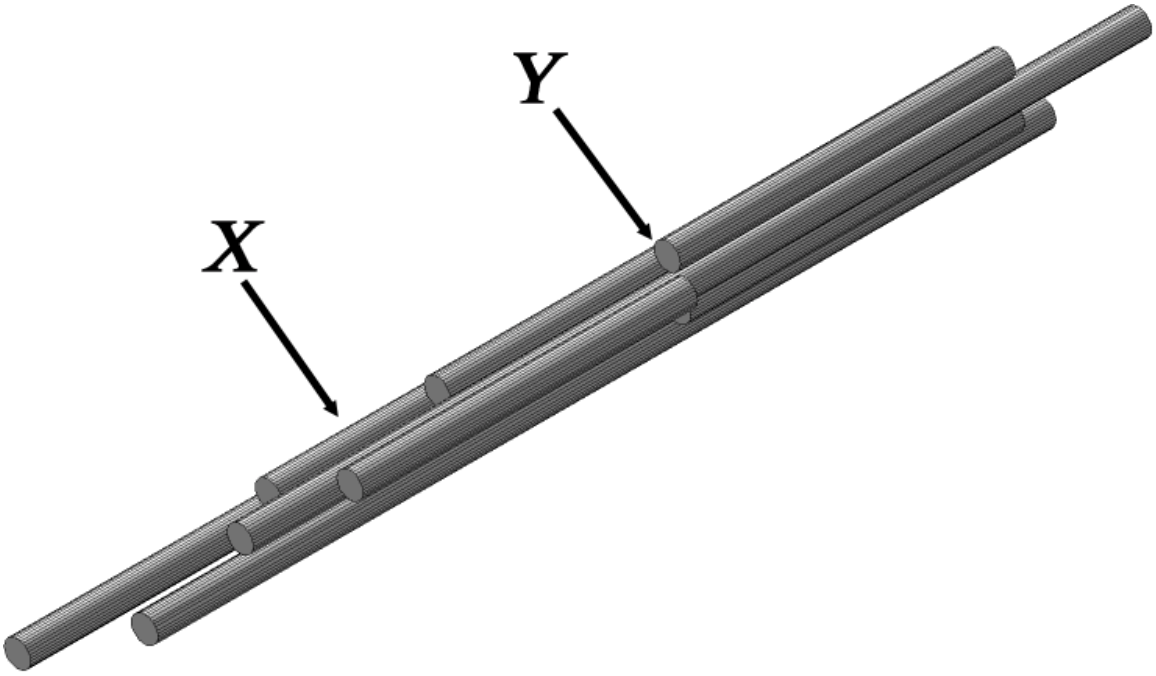

Figure 10. Depiction of bundle of carbon nanotubes. Individual nanotubes comprising the bundle may consist of SWNTs, MWCNTs, or both. Properties studied at point X may differ from those taken at point Y due to different constituent CNTs. This aspect of CNT aggregation/growth introduces an element of uncertainty into any CNT measurement.

Unique properties of carbon nanotubes

While the last several paragraphs deal primarily with the electronic properties, the mention of CNT mechanical properties in conjunction with MWCNTs is worthy of a brief discussion. A figure of merit for mechanical properties in a materials system is the Young's modulus. Along the axial direction, this value has been measured to be as large 1-2 TPa in CNTs.[17-22] Another figure of merit is the tensile strength, which may determine the feasibility of CNTs for use in materials systems in which strength-to-weight ratio is critical. Measured to be between 1-60 GPa depending on if CNTs are multiwalled, individual single-walled, or bundles, this value compares favorably to steel with 1.2 GPa.[23-25] This value also represents the ability of CNTs to withstand axial strain and indicates CNTs may be useful in making strong, lightweight systems.

Yet another intriguing property of CNTs is their chemical inertness in the presence of many chemical species even at elevated temperature.[26] The absence of dangling bonds due to the extended sp^2 hybridization in CNTs means that there are few routes for reactants to break apart or weaken CNTs. This allows CNTs to be considered for applications in which existing polymers may not be considered due to chemical incompatibility, i.e. CNTs would be applicable where Delrin® is not. In addition to their chemical inertness and unlike many polymeric compounds, CNTs do not melt at high temperatures (1000℃).

Carbon nanotubes, like graphite, are expected to have high thermal conductivity. An excellent review of thermal conductivity in carbon nanotubes is

provided in Refs. 27 & 28 with robust recent activity in the field.[29-34] The thermal conductivity in CNTs has been predicted to be as large as 3000 W/m-K in the axial direction at room temperature. This is due to a phonon mean-free-path of 0.5-1.5 μm.[35-38] This is another property of note in CNTs as they are considered for heating/cooling applications.

Carbon nanotube organization and nomenclature

An organizational chart is presented in Figure 11. This chart briefly outlines the types of carbon nanotubes in their most common categorization. This chart only deals with carbon nanotubes defined as being constructed of seamless tubes of graphite/graphene. There exist other carbon nanostructures with inner hollow space which should not be properly called CNTs. Many measurements have been done and papers published that presuppose a reader's knowledge of this classification of CNTs, and it is provided here to help properly place this work in context with other nanotube-related research. These are the basics of carbon nanotubes necessary to navigate this dissertation. The broad scope of nanotube research demands precision within descriptions of carbon nanotubes, and this introduction is merely intended to avoid confusion about which particular materials system is being studied: SWCNT, MWCNT, DWCNT, bundle, metallic or semiconducting CNTs. However, for purposes of this dissertation, a reference to CNT alone will imply the CNTs produced in this laboratory, which are narrow diameter (<5nm) and presumably single-walled, although it is possible that DWCNTs or bundles may have been studied in some of these cases. Where important for interpretation of the results, this will be noted.

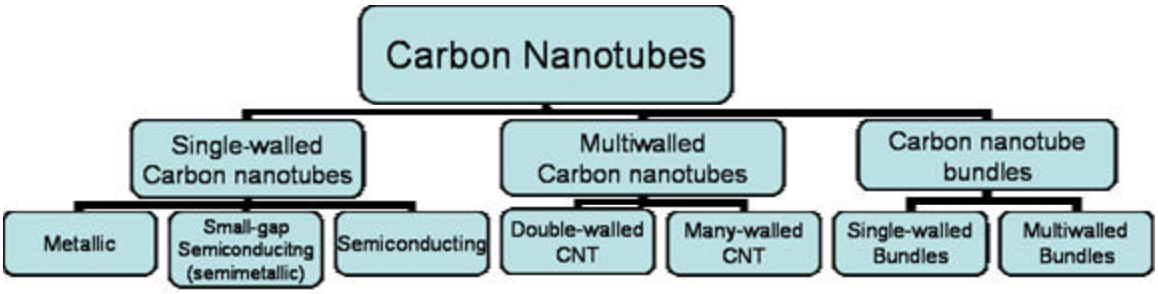

Figure 11. Organizational chart depicting general CNT classification. This chart is meant as a rough guide. Each of the single-walled nanotube can further be classified by its (*n*,*m*) structure (see text), and the bundles can easily consist of SWNT/DWNT mixtures. The nomenclature for carbon nanotubes is undergoing continuous transformation, but the monikers above have received wide enough usage to merit inclusion here.

Chapter summaries

This thesis will describe efforts to facilitate existing and develop new methods for fabricating devices consisting of individual SWCNT, and to study the electronic properties of such devices. Refs. 39-45 represent publications in which the work of this dissertation was treated in the open literature. A brief summary follows:

Imaging CNTs on insulating substrates is a major bottleneck to device fabrication. Here it will be shown how, in a scanning electron microscope (SEM), CNTs can interact with the surrounding oxide to produce a dynamic voltage contrast.[39] This feature allows for more rapid characterization of CNTs than in previous techniques and allows for device manufacture using long (>100μm) CNTs. It also has implications for measurements of CNT diameters taken solely from SEM imaging. A version of this chapter is published in the open literature as Ref. 39.

Another promising feature of CNTs was that their nanometer scale would allow channels to be approximated as infinitely thin, ballistic conduction

channels.[44,46] This has not shown to be the case as the component materials in CNT devices can actually scale to the point that the CNT diameter must be considered to understand their electrical transport. This understanding results from experiments detailed in this dissertation in which CNTs are integrated into a field-effect transistor geometry with high-dielectric-constant $SrTiO_3$ as gate dielectric and CNT as channel. These devices show the highest transconductance per unit width of any CNT-FETs at the time of publication in the literature, as seen in Refs. 44 and 47.

The understanding of contact effects will be extended to include focused-electron beam induced deposition (FEBID) of pure gold for contact to nanotubes. This is a specialized, serial technique for *in situ* fabrication of metal lines which are placed on a surface utilizing a scanning electron beam to achieve a direct write of patterned solid gold electrodes. For CNT experiments, the behavior of metals in terms of contact resistance has been a primary barrier to understanding CNT behavior. Within the lithography community, it has been a challenge to create solid metal lines using FEBID. These two questions are brought together here as the contact resistance of solid gold FEBID lines on small-diameter SWNTs is studied utilizing two-probe electronic transport measurements and electrostatic force microscopy.

It is also often assumed that the strength of the carbon-carbon sp^2 bonds would prevent the formation of defects within the carbon lattice, and thus they could be considered 'pristine' materials. When utilizing semiconducting SWCNTs in transistors, this would prevent the complications associated with substitutional dopants (e.g. Na^+) in silicon devices. This is still an open question as the role of

defects in both the SWCNT and the surrounding substrate are still under study. This is investigated here in preliminary measurements on long CNTs which are suspended in vacuum between two metal electrodes. The growth and manufacture of these devices will enable experiments which may shed light on the intrinsic properties of CNTs absent the effects of a surrounding substrate, and the fabrication method for such studies has been a general focus of the research detailed in the entirety of this dissertation.

While not treated in this dissertation, some work on use of nanotube field-effect transistors in the detection of charge was also contributed by the author and can be found in Ref. 43 and the thesis of Tobias Dürkop.[48]

Chapter 2: Experimental techniques

Having examined the origins of carbon nanotubes in terms of their theoretical structure, this section shall discuss growth of carbon nanotubes in the laboratory along with lithography techniques for manufacturing carbon nanotube field-effect transistors and scanning probe techniques for characterizing. A brief description of the historical context of CNT discovery will provide an insight into the serendipitous nature of experimental physics research. Lithography and electrostatic force microscopy are further detailed in Appendices 1 and 2.

Historical techniques for CNT production

The larger examination of sp^2-bonded carbon actually resulted from initial experiments on linear carbon-chain molecules discovered in interstellar space.[49] In trying to reproduce solar conditions in the laboratory for further study of these molecules, mass spectrometry of the resulting molecules coupled with careful control of the growth environment allowed for conditions which showed a marked predilection for the carbon molecules to come in groups of sixty atoms with little other residual carbon masses present. These signatures led to a description of the C_{60} molecule.[2]

As mentioned in Chapter 1, CNTs can be thought of as a long cylinder of graphene between two capping C_{60} molecules. Indeed, the synthesis of carbon nanotubes derived directly from research on C_{60}. In Ref. 50, Kratschmer *et al* discovered a process of producing macroscopic quantities of C_{60} from the purified soot produced in evaporated graphitic rods.[50] This became the starting point for

research on CNTs. Iijima's investigations into soot produced in a similar fashion yielded the first unambiguous determination of CNTs as long graphitic microtubules present in high resolution transmission electron micrographs.[5] The 'tubules' came in 2-50 nesting concentric shells: a departure from the long, twisting structures common in the formation of carbon black.[51,52] These were the so-called multi-walled carbon nanotubes (MWCNTs) described in the previous chapter, and they were the primary 'tubules' produced in the soot.

Subsequent studies of CNTs focused on the importance of transition metals in the graphite used in the so-called arc-discharge method, the name given to the procedure in Ref. 53 in which graphite rods are used to spark an arc in an inert or reducing atmosphere.[54-56] The presence of Fe, Ni, Co, and other metals resulted in higher yields of single-walled carbon nanotubes. Laser ablation studies,[1] which followed the development of the arc-discharge method, showed this same dependence as transition metals in the laser targets produced higher yields of SWNTs. In our studies, the term "SWNTs" will be used to refer generally to narrow diameter (<5nm) CNTs which may have one *or a few* shells.

The usefulness of these techniques in producing large quantities of CNTs was also their main drawback: CNTs were only being studied in ensembles. To investigate individual nanotube behavior, macroscopic quantities of CNTs had to be separated and dispersed. There is an entire line of CNT research devoted to this effort which will not be discussed here,[57-69] but an informative review can be found in Ref. 70. While robust and productive, these efforts further led to complications in describing the impact of the separation techniques on the eventual device behavior.

To avoid this problem of 'sort and search,' some CNT researchers, the author included, began to focus on the use of catalytic chemical vapor deposition (CVD) for the production of carbon nanotubes which entails minimal handling and treatment. Carbon nanotubes produced in this manner can also more reliably be called 'pristine,' due to the lack of handling in the separation processing. Thus, the use of CVD-grown CNTs to attempt to study intrinsic properties of CNTs is preferable to using CNTs which may have process-dependent defects.[71] This is not to say that the performance in an intrinsic device will outperform those that have specifically been doped or otherwise altered to achieve better performance. The purpose in such a study is the determination of underlying CNT behavior, absent the influence of defects, dopants and environmental effects.

Chemical vapor deposition

The essence of nanotube growth is the combination of high temperatures, the presence of catalyst, and carbon-containing feedstock gases. It as an amalgam growth procedure derived from Refs. 72 and 73. The substrates are typically SiO_2-capped, degenerately-doped silicon or single-crystal quartz. The catalyst is prepared as a solution of anhydrous iron (III) nitrate in isopropyl alcohol in concentrations ranging from 0.010 to 1 g/mL. The substrates are dipped in this solution, after which they are transferred to pure hexanes, and then blown dry with nitrogen. The hexanes cause the iron nitrate to precipitate out of the isopropyl solution and onto the substrate. This deposits catalyst over the entire substrate in a roughly uniform fashion which results in CNTs similarly distributed on the surface: in a random, but mostly uniform way.

This necessitates the use of a "find-and-wire" technique which is described in the lithography subsection.

Aside from this step, it is also possible to 'drop cast' high concentrations of the iron-nitrate/isopropyl solution directly onto the substrate for a macroscopic "patterned growth." This is accomplished with the protruding fiber of a broken wooden dowel for drops with 500-1000μm radius on the substrate. For truly microscopic placement of CNT catalyst, some form of lithography may be used to pattern where the catalyst will be located[72] or the drop casting method can be scaled down with the use of microscopic tips laden with catalyst.[74] Otherwise, the dipping and precipitation method results in substrates with catalyst particles randomly dispersed across their surface. The catalyst-laden chips are then transferred to a growth oven, seen in Figure 12.

Figure 12. Picture of growth oven used in chemical vapor deposition type growth of carbon nanotubes: Quartz tube inserted through insulation at ends passes through one growth "zone" represented by thermocouple present outside the quartz tube in the middle of the oven. Coils surrounding tube provide uniform axial temperature. Radial gradient is ~50 K due to quartz tube, location of thermocouple, and flowing gases.

The CNT growth furnace is assembled from modular components specifically for use in CNT growth. The system's primary component is a single-zone, LindbergBlueM tube furnace with a nominal maximum temperature of 1100°C, indicated in Figure 12. It is run by an external Omega temperature controller through a pulse-modulated feedback loop (not shown). All the growth gases are UHP/Zero grade, and they run through high purity regulators and Omega rotameters which give flow rates to ±1% (not shown). All flows are quoted in the gas-density-corrected actual standard cubic centimeters per minute (sccm), not the sccm air values provided by the manufacturer. The conversion is given

by: $SCCM_{actual} = SCCM_{air} * \sqrt{(\frac{spec.grav_{gas}}{1.0})}\sqrt{(\frac{pressure_{gas}[psi]}{14.7})}$ where 1.0 and 14.7 are the specific gravity and ambient pressure of air. The gases mix in a stage following the rotameters. They then pass through a 1200mm long, 22mmID x 25mmOD GE 214 Quartz tube seen in Figure 12.

Substrates are typically cm-size chips cleaved from single-crystal polished silicon wafers capped with an oxide or single-crystal quartz wafers, both 500μm thick. These are placed inside custom-made quartz 'boats' which are designed to minimize the amount of turbulence near the substrates, as seen in Figure 13. The samples are positioned inside the quartz tube such that they are underneath the thermocouple which is seen protruding from the top insulation of the oven in Figure 12. The tube is then sealed and purged under ~700 sccm of argon.

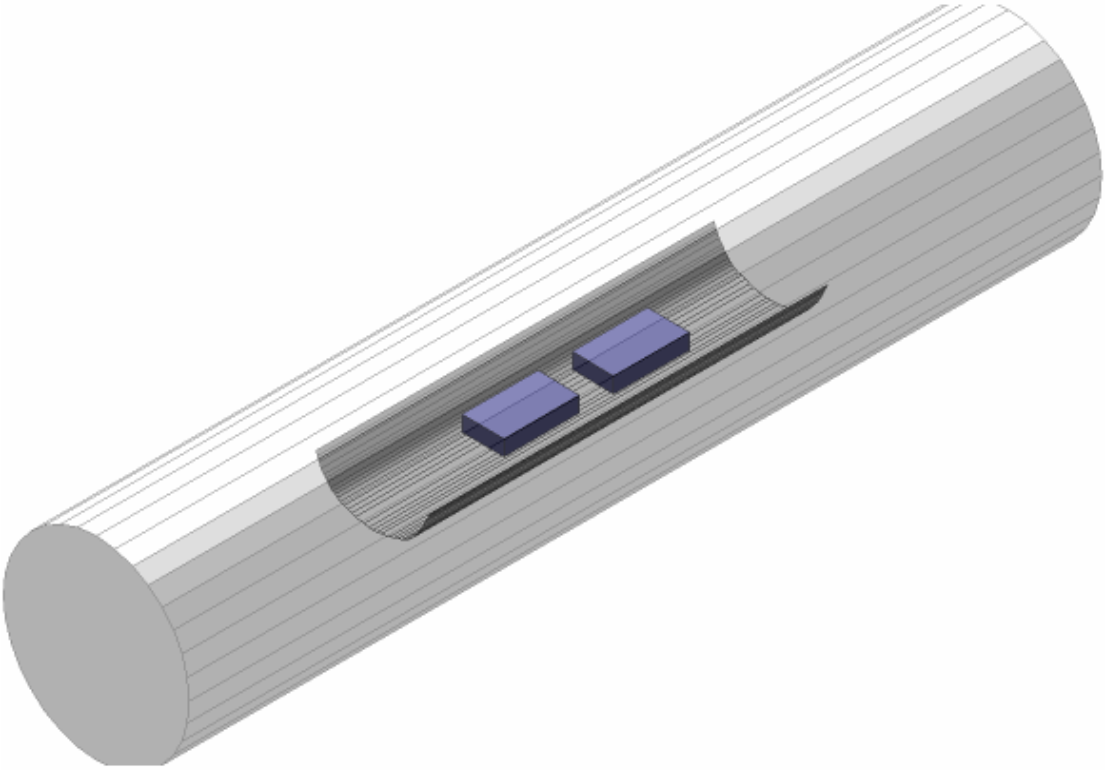

Figure 13. Schematic picturing the quartz tube and quartz boat inserted in growth oven depicted in Figure 12. The boat is shown with two substrates placed along the length of boat. Width of substrate determines vertical placement in boat.

Following a ~10min purge, the temperature is raised to the growth temperature. This is done with either a ramping routine which 'soaks' at intermediate temperatures before reaching the eventual growth temperature (~60min total ramp time) or by directly setting the temperature controller to the growth temperature (~15min total ramp time). The nominal growth temperatures, as indicated by the thermocouple, ranged from 850-950°C. It should be noted that the actual temperature at the sample is different than the nominal temperature indicated at the external thermocouple; the actual temperature changes with growth gas and flow and nominal temperature. Following Ref. 75 for CNT growth, growth gases are typically a

methane/hydrogen/ethylene co-flow with flow rates of ~1500, ~2000, and ~20 sccm respectively. This produces long, >100 μm, CNTs with diameters less than 2nm, as measured by atomic force microscopy (see scanning probe microscopy section in this chapter and/or Appendix 2).

An example of a typical CNT growth is shown in Figure 14. Here, catalyst particles are seen in the top of the image. The CNTs roughly align to the gas flow direction (top to bottom in this image) and can be very long, where aspect ratios of 10^4-10^5 are not unusual. This feature of CNTs is one of primary interest. Recent reports indicate that it may be possible to grow CNTs to almost arbitrarily long lengths.[76-80]

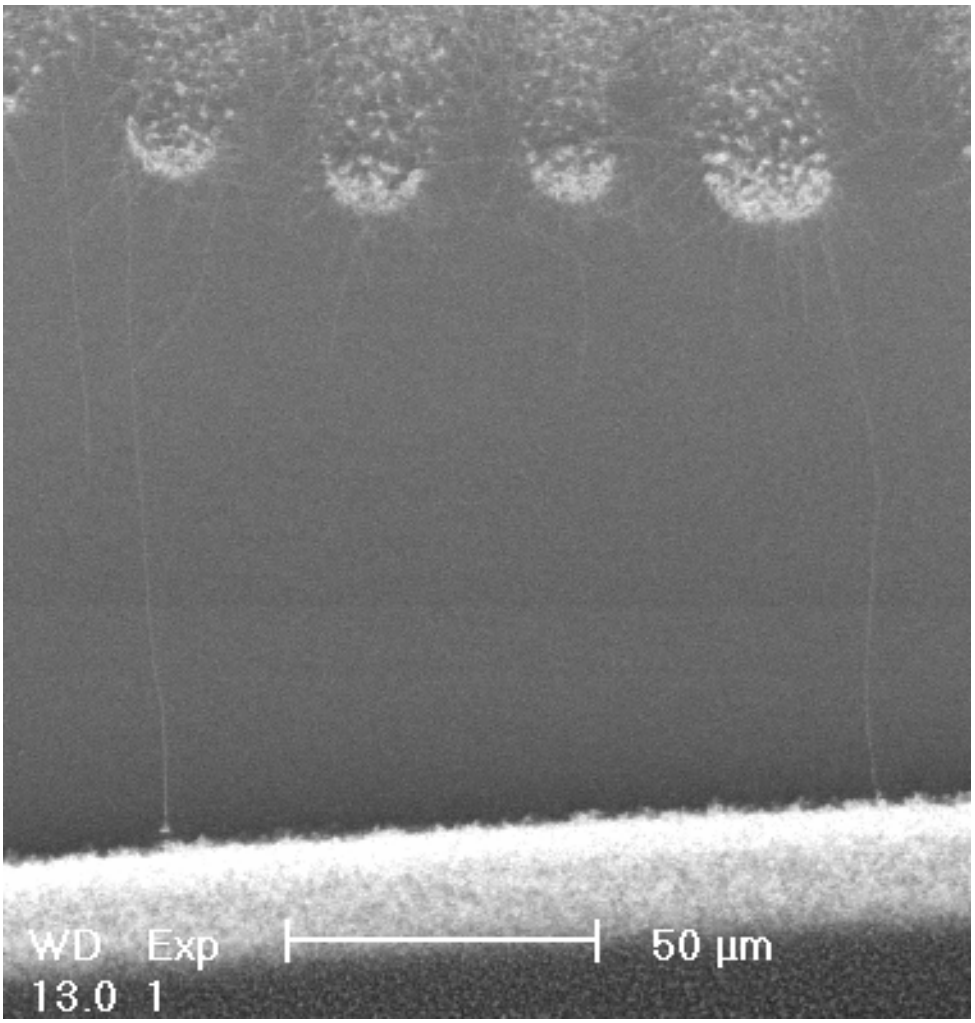

Figure 14. Picture of carbon nanotubes growing from a drop cast solution of catalyst particles. Iron nitrate dissolved in isopropyl alcohol is deposited onto a flat substrate. Drying rings at edge of macroscopic drop produce smaller ordered catalyst islands. Following growth procedure described in this chapter, long CNTs can be seen growing from these catalyst islands. Material at bottom of image is pre-deposited platinum electrodes.

As an aside, it should be noted that other researchers have suggested that long CNT growth may solve the problem of CNT (n,m)-type uniformity in the following way: It is possible to divide a specific (n,m) type of CNT into segments, then open the segment, and 'seed' new CNT growth from segments of known (n,m) type.[81] Utilizing both properties, the random distribution of electronic properties could be avoided through proper choice of the initial 'seed' CNT and through iteration of long CNT growth.

The CNTs described herein grow with a distribution in terms of electronic properties, with a large majority (>70%) showing some response to a gate, thus nominally semiconducting, and few showing no response, or metals. The distribution in (n,m) type devices has also been seen, and more rigorously characterized, by Oron-Carl *et al*.[82] The distribution happens because there is almost no energy or conformal barrier to the formation of one (n,m) configuration versus another. There seems to be some relation between catalyst particle size and eventual CNT diameter[83-86]; however, even similar diameter tubes can have very different (n,m) values. On this subject, results are inconclusive, and research is ongoing.

This means that there must still be a type of search involved in the manufacture of CNT devices. The CNTs roughly align to the flow direction in the growth chamber, but they must still be located in order to put electrodes on top of them. This "find-and-wire" philosophy has both advantages and drawbacks. The production of unique, custom-made CNT devices can take place in as little as a few days and be done by a single researcher with standard skills concerning growth, lithography, imaging, evaporation, and electrical characterization. Therein lays also the main drawback. Although a few selected devices can be produced quickly, yields are quite low and the process requires dedicated interaction with a highly trained researcher. Thus, this technique is readily adaptable to most types of novel nanoscale research, yet it leaves all the problems of 'scaling up' for others to solve.

Depending on the initial concentration of iron nitrate catalyst and location within the quartz tube and on the substrate, CNTs have a surface density ranging from 0.01-100 CNTs/μm^2. Expressed in terms of typical microscope imaging conditions,

this translates into several nanotubes per 10µm x 10µm square for lower concentration with the higher concentrations leaving behind a mat of tubes crossing to the point that individual tube identification becomes moot. An example of such tubes at the threshold of becoming a mat is seen in Figure 15. In sparser concentrations of CNTs, isolated CNTs can be located so pairs of electrodes can be placed along the CNT length. The spacing between electrodes ranges from 50nm to over 200µm. This process is described in more detail in the following section on lithography.

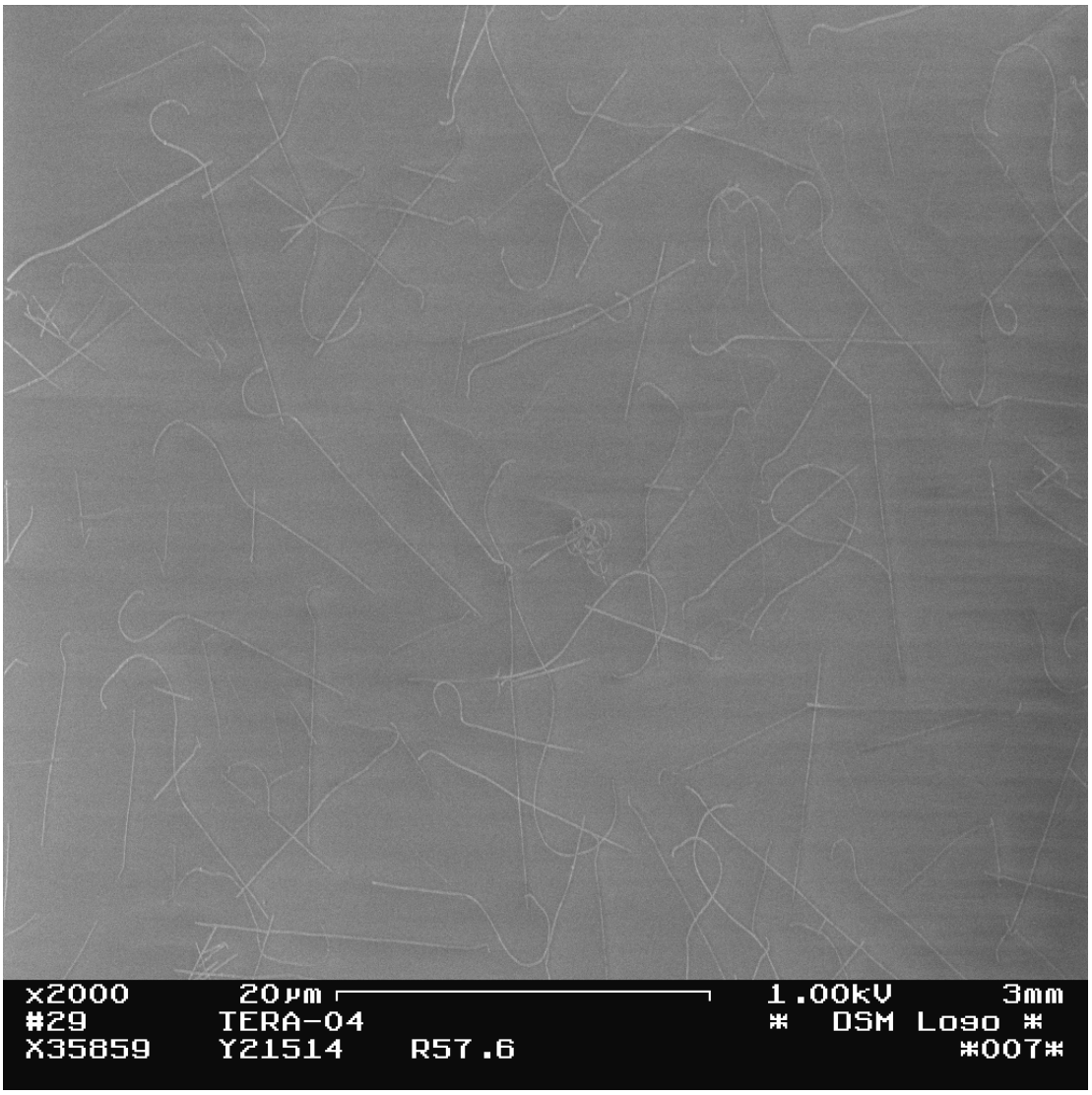

Figure 15. Carbon nanotubes on silicon oxide surface. Carbon nanotubes of length ~20µm can be seen randomly dispersed on the oxide substrate. This results from the random, approximately uniform distribution of catalyst particles on the substrate.

The CNT growth described thus far has only involved growth on substrates. This technique depends on substrates which do not appreciably alter in reducing, high temperature atmospheres. It is also possible to utilize 'substrates' of smaller nominal length scales. This will be described in Chapter 6.

As mentioned, the main ingredients of carbon nanotube growth are carbon containing feedstock gases, catalyst, and high temperatures. The growth process is

robust to even minimal amounts of catalyst. An example of this is seen in Figure 16. Here, single iron atoms within the hemoglobin molecule, present in dilute concentrations within a typical human hematic system, provide the necessary catalyst for CNT growth. This is verified by the presence of CNTs at the edges of the drop cast solution while none appear on the bare oxide. As has been shown, there are many different ways of combining these ingredients for different types of CNT growth, but the procedures and equipment detailed in this chapter have, unless otherwise stated, produced the CNTs under study in this dissertation.

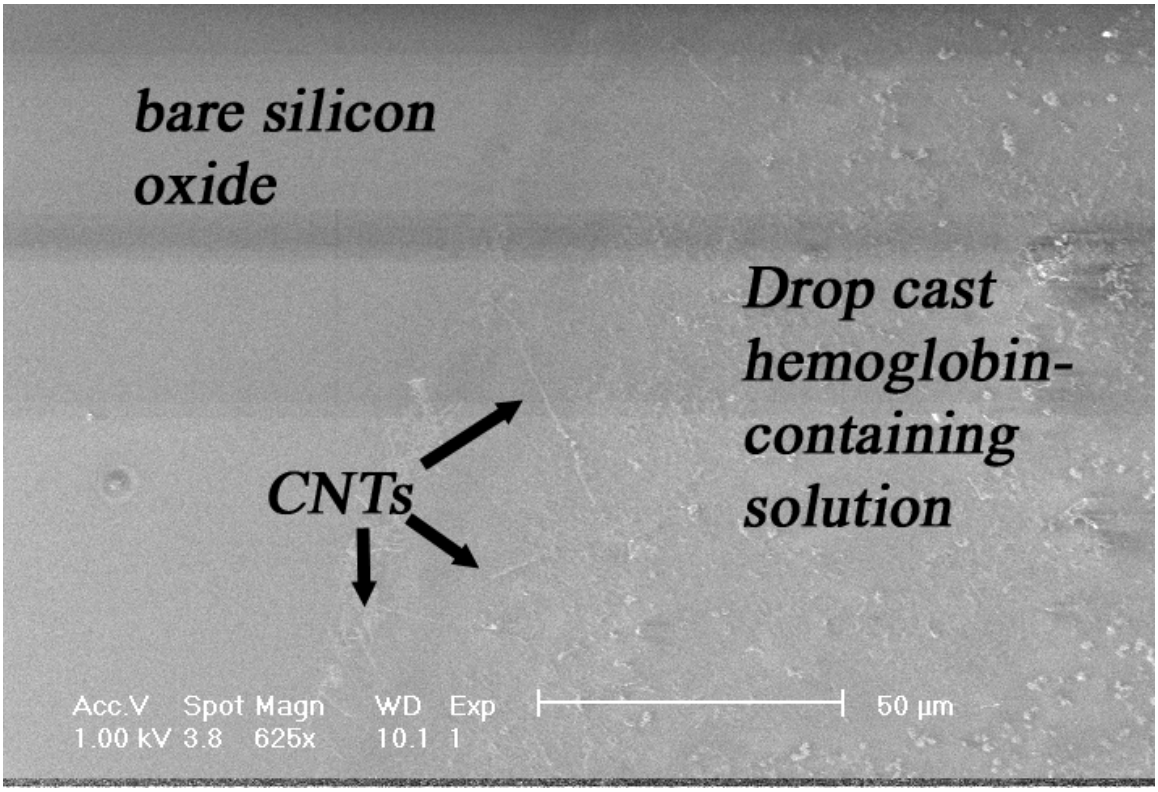

Figure 16. SEM image showing the robustness of CNT growth to minimal amounts of catalyst: The single iron atoms (presumably aggregated during catalysis) present in hemoglobin provide enough catalyst for CNT growth.

Lithography

Following growth, an essential tool for making CNT devices is lithography. Originally conceived by a Bohemian painter in Austria, lithography means 'writing on stone' and was used to make patterns on stone which could then be transferred to paper.[87-89] In this work, it refers to the process of putting metals into defined locations on a substrate. Methods and techniques are covered in several general references as well as in the Appendix 1.[90-92]

Find-and-wire

Herein, there are two general methods for manufacturing CNT devices. One is called 'find-and-wire'. As the name implies, in this technique CNTs are located and then wired with electrodes positioned on top of the CNTs. The other is 'wire-and-find.' Again as the name implies, the CNTs are dispersed or grown on the substrate, after which electrodes are put into arbitrary locations on the surface. Already-wired, complete devices are then found using microscopy or electrical probing. Each technique has advantages and disadvantages. With find-and-wire, device geometry and CNT morphology can be precisely controlled. However, separate steps are needed for producing alignment/coordinate markers and for locating the CNTs. Conversely, wire-and-find skips both these steps. Electrodes are simply evaporated onto a CNT-laden substrate. An essentially random process, wire-

and-find does not control device geometry and CNT morphology to the same extent as find-and-wire, which would be its main disadvantage.

Mentioned in connection with the find-and-wire technique above, *alignment* is essential to this type of CNT device synthesis. Alignment generally means the ability to put down one lithography pattern with respect to another pattern. The existing layers define a coordinate system which the following layers can be *aligned to* using a series of fiduciary marks. These marks are at known locations in the existing pattern while the pattern which is *being aligned* includes complementary marks which allow the calculation of an alignment matrix and an offset. It is also useful for making devices at arbitrary locations on a substrate, something of particular pertinence for carbon nanotube research. This is because CNTs are randomly dispersed across the surface of the substrate, making alignment necessary for device fabrication. Hence, the find-and-wire moniker: to distinguish it from other CNT fabrication methods that rely on predetermining the location of CNTs by controlling the location of the catalyst particles.

Figure 17 shows the type of matrix used in CNT device fabrication in which alignment was necessary. The large pairs of squares at the four corners of the pattern are the actual 'alignment markers.' In subsequent alignment, crosses are positioned such that they overlap the crossing point in the pairs of squares. This provides both the offset and the rotational matrix necessary to translate the coordinate system on the substrate into that of the computer doing the writing (or vice versa). The pattern shown is typically 90x90 μm^2. The figures in the middle of the pattern actually define the coordinate system of the 'alignment' reference frame. The squares present

to the left of the individually unique markers are there to allow the electron beam to 'settle' as it jumps from coordinate marker to coordinate marker. These squares have the additional benefit of providing orientation at intermediate magnification (100-1000x) within an optical microscope, but could also be eliminated from the pattern if desired. The intersection of the shorter vertical line (nominally 500nm long) with the longer horizontal one (~1μm long) present in the middle of each coordinate marker defines a point to within the accuracy of the microscope's linewidth (~100nm).

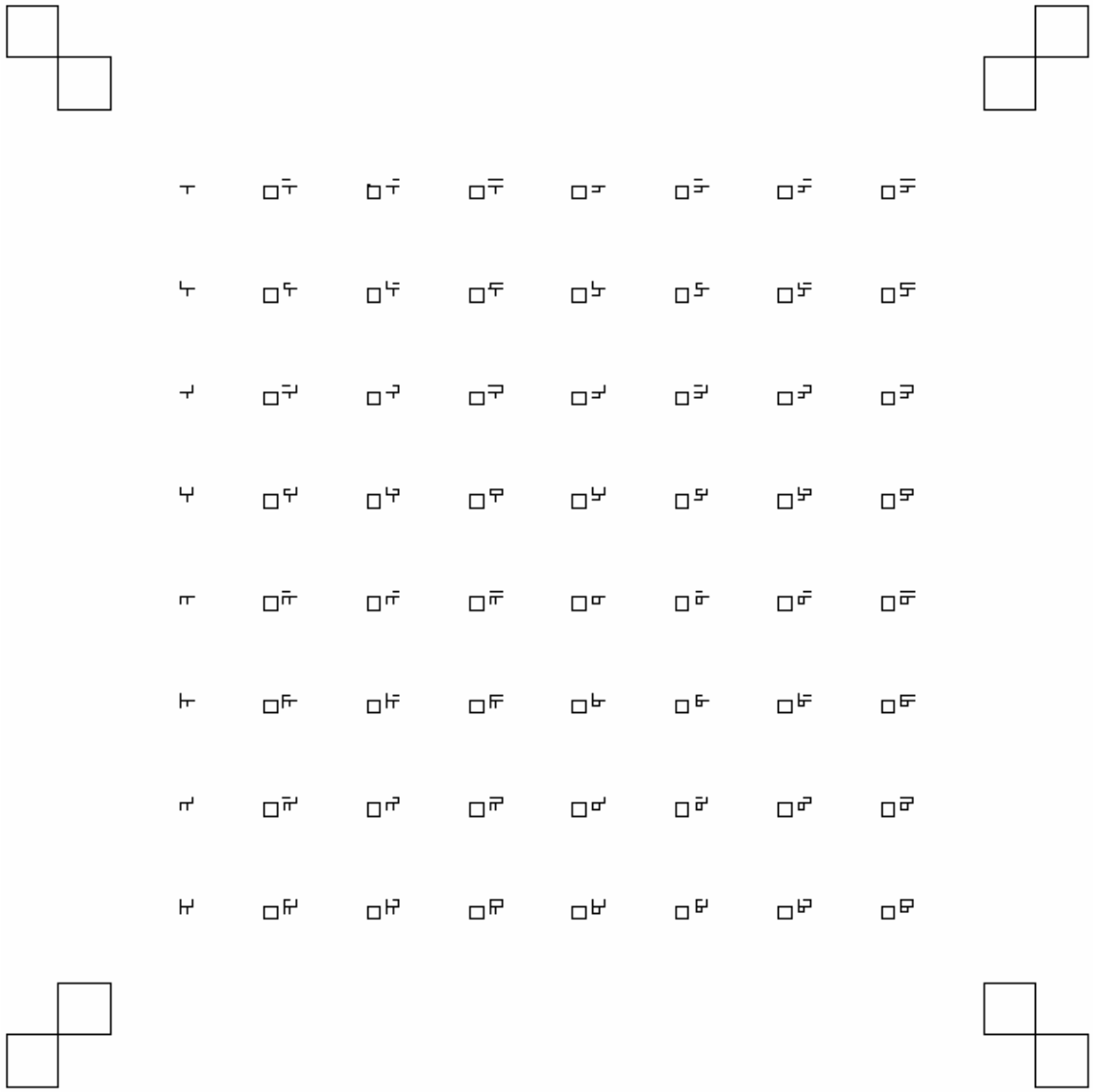

Figure 17. Alignment and coordinate markers used for 'find-and-wire' technique of CNT device fabrication. The outer alignment markers exist at well defined points within the coordinate system whose points are more precisely defined by the T's in the middle of each of the unique coordinate markers lying in the interior of the square defined by the alignment markers. The position of each coordinate marker is uniquely determined through a base two system which in principle allows for a 16x16 grid of markers (only an 8x8 grid is implemented here).

The coordinate markers are then uniquely identified by a base-2 system. The top horizontal line is broken into two pieces, with the presence or absence of these sections representing “0” or “1” respectively, forming the first two digits. The bottom line is also broken into two sections, defining the next two digits. Thus the set

of horizontal lines can be used to represent a number from 0 to 15, giving the column index. Likewise with the top vertical lines and bottom vertical lines, an additional number between 0 and 15 may be represented, giving the row index. Thus a 16x16 grid of unique markers is possible (only an 8x8 grid is implemented here) allowing a picture of one marker to be used to determine a location within a 16x16 grid. Note that the "T" in each marker breaks rotational symmetry, such that a picture of one marker is sufficient to locate the marker, without knowing the orientation of the picture. These aspects are particularly useful when the marker system is used in conjunction with scanned-probe imaging, in which images are taken rather slowly, over small areas. This system was designed to make each marker identifiable while using minimal surface area for this identification. Other methods exist for achieving the same end,[93] but this particular layout has proven robust and simple for the purposes of the 'find-and-wire' technique utilized for CNT device manufacture.

The coordinate/alignment marks are deposited on the substrate after CNT growth. Thus, CNTs lie underneath the metal evaporated for the alignment markers. An SEM micrograph of a CNT together with coordinate and alignment markers is seen in Figure 18. The CNT can then be 'mapped' out through use of either an atomic force microscope (see Chapter 2) or a scanning electron microscope (see esp. Chapter 3). After mapping CNT location within the defined reference system, a second lithography pattern can be defined which will place electrodes on top of the CNTs. This process is very adaptable to the length and orientation of the CNTs. The electrode separation can vary from 0.1-1000μm. Thus, the patterning of the electrodes can change for each substrate, depending on CNT length and

concentration. While robust to such variation, the principle drawback in such a system is limited throughput due to the need for user feedback in the electrode patterning. Thus, each CNT pattern is custom made.

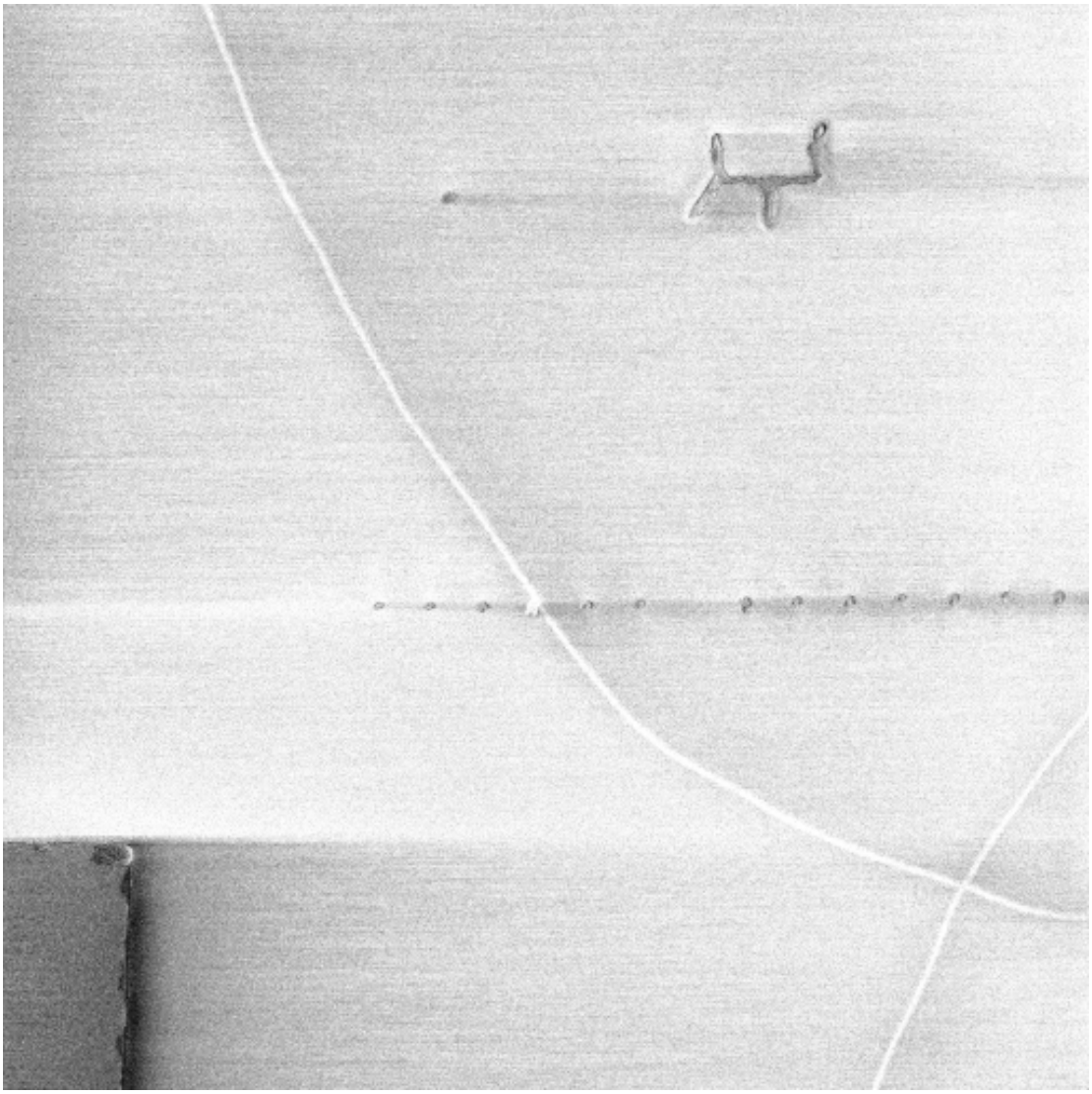

Figure 18. Scanning electron micrograph typical for locating CNTs in the find-and-wire technique: The coordinate marker from the bottom left of the array appears in the image. A CNT can be seen between the coordinate marker and the edge of the square of an alignment marker. Alignment markers allow for precise alignment to this coordinate system. A second step can be performed to put electrodes on top of the CNTs.

An example of a completed pattern is shown in Figure 19. Following the mapping of Figure 18, a second lithography step is completed to deposit electrodes

perpendicular to the direction of the CNT. Such a device is typical of those produced using the find-and-wire technique. These define a geometry in which the CNT acts as the transistor channel. The oxidized silicon acts a dielectric, while the degenerately doped silicon behaves as a universal 'back gate.' Figure 19 shows the same region as Figure 18 after the second lithography step as seen by the presence of electrodes on top of the CNT. This represents a completed CNT-FET. Comparing to typical complementary metal oxide semiconductor (CMOS) transistors, the electrodes act as source and drain. Unlike CMOS however, the CNT lies on top of the dielectric instead of being buried beneath it. This allows for important applications in the interaction of the CNT with its environment.

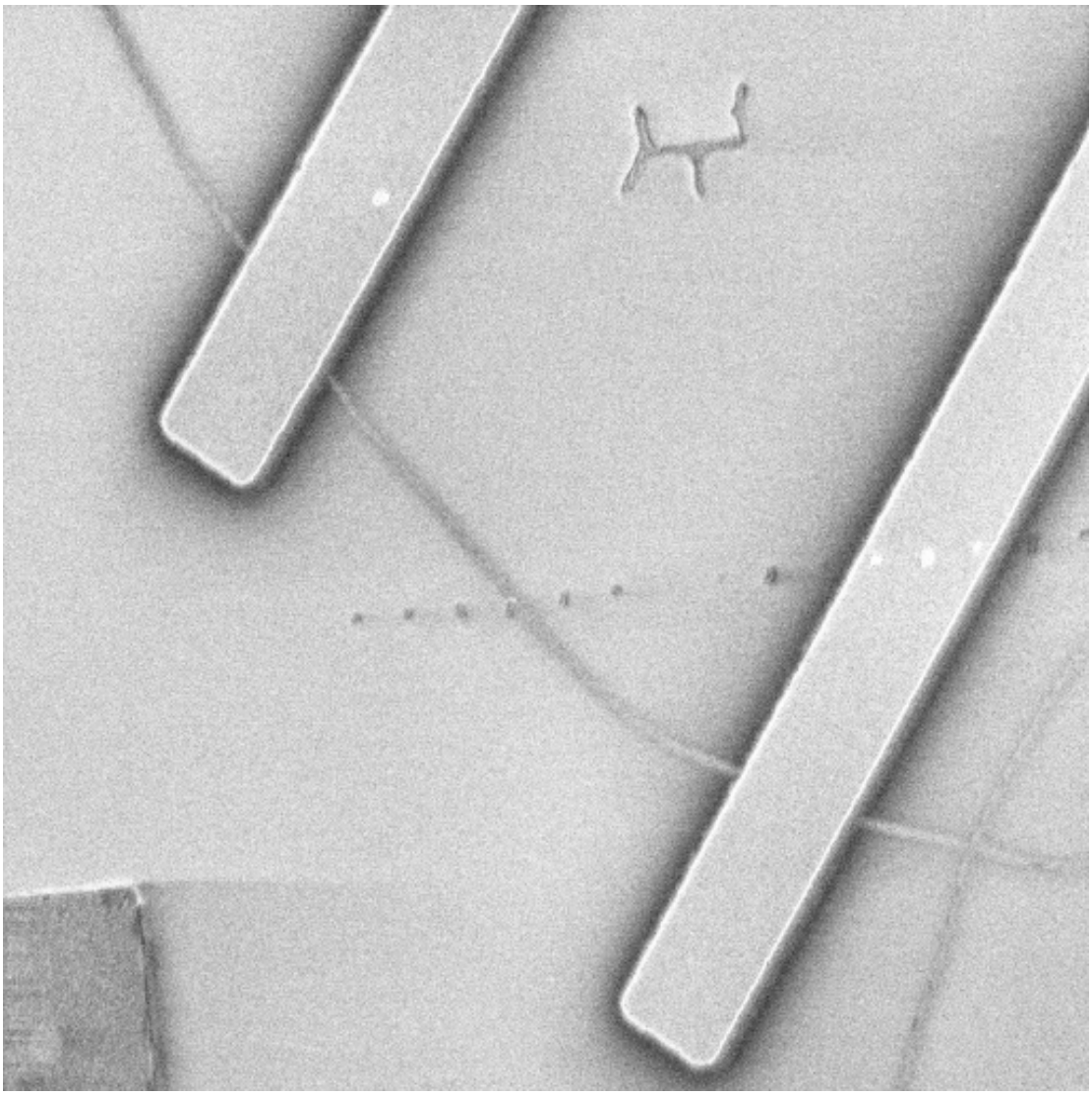

Figure 19. Metal electrodes covering the CNT depicted in the previous figure. The electrodes are defined in a second lithography step utilizing the alignment marks depicted in the corners of Fig. 17. Utilizing these marks and the coordinate system defined by the coordinate markers, the electrodes can be positioned on top of the CNT to arbitrary channel lengths (or electrode separation).

Wire-and-find

The wire-and-find technique lacks the versatility of find-and-wire, but throughput is greatly enhanced. A good example of wire-and-find is seen in Figure 20. The array of gold electrodes have been evaporated through a stencil mask (see

Appendix) without previous knowledge of CNT location. The substrate is single crystal quartz diced into a ~1cm^2 piece. CNT lengths exceeding several hundred microns actually enable this technique; shorter CNTs would not span the electrode spacing shown in this device. As described in the introduction to the subject, the electrode spacing tends to be more rigid in wire-and-find where large arrays of identical electrodes are produced in parallel. Another point that is particularly useful with a stencil is that it avoids problems associated with charging insulating substrates, particularly important for the quartz substrate pictured here.

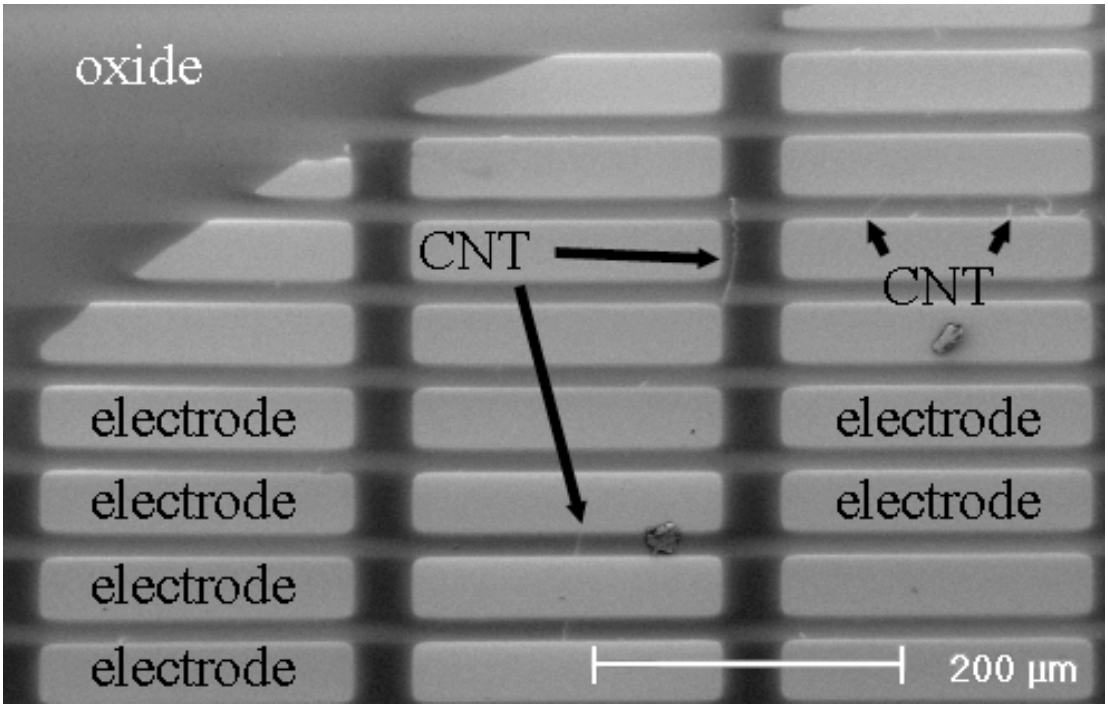

Figure 20. Example of wire-and-find technique: Gold electrodes are evaporated through a stencil grid. CNT location is not known previous to electrode deposition. Micrograph shows CNT spanning electrodes to the right of the image. Image courtesy of Tony Przybysz.

These lithography techniques enable the study of materials at the nanoscale, and the studies described here utilize these techniques. Lithography provides researchers with a tool to put materials of nominal length scales ~10nm almost any

where on an extended flat surface. Although the experiments herein never required that electron beam lithography below ~50nm, it has been an important component of much of the work here.

Scanning probe microscopy

Another tool in the investigation of material systems is the scanning probe microscope (SPM).[94,95] As a tool for nanotechnology, the SPM is indispensable in its ability to map out two-dimensional surfaces, not only in qualitative terms that change laterally, but also their topography. This chapter will deal with SPM and how it relates to the study of CNT devices. Most of the information in this chapter and additional study materials can be found in standard introductions to scanning probe microscopy, tutorials, or user manuals for specific microscopes.[96-99] Also, there is additional material in Appendix 2 concerning the use of electrostatic force microscopy to study CNT devices which is covered later in this chapter.

Scanning probe microscopes generally refer to a class of microscopes that utilize a piezoelectric positioner to scan a "tip" (which may be a sharp wire or a microfabricated cantilever) in two dimensions over a sample surface. The piezoelectric positioner also controls the height of the tip over the surface, and this height is determined using a feedback loop. For example, scanning tunneling microscopy (STM), as given in Ref. 95, relies on a tunneling current between the tip and the sample to investigate the surface. The feedback loop acts to keep the tunneling current (and thus roughly the height) constant. While an important tool, STM requires conducting samples.

Atomic force microscopy

The atomic force microscope (AFM) works on the principle of mechanical amplification in that the interaction of a microscopic object with a nanoscopic one can be detected using a precisely aligned optical system. The optics magnify the mechanical interaction of the tip of a microscopic silicon cantilever as it drags across or oscillates over a surface. This is seen in Figure 21. This detection method does not require conducting samples, and thus is more widely applicable.

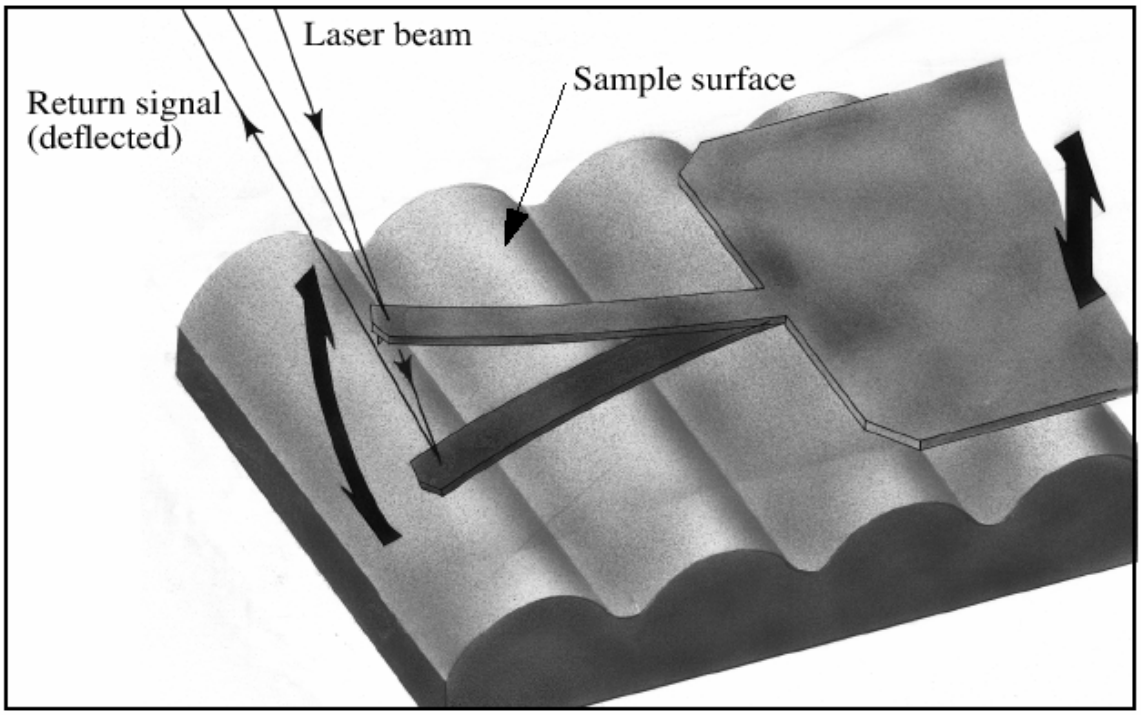

Figure 21. Scanning probe microscope cantilever interacting with a scanned surface. Image courtesy of Digital Instruments Veeco Metrology Group.

In Figure 21 one sees the cantilever, which has a tip protruding from the end of a singly-clamped beam, can be driven into oscillation by a piezoelectric element (not shown). As it does so, a laser reflects off the cantilever shines onto a

photodetector. A feedback loop can then be used to move the cantilever up and down (through use of a piezo tube) as the cantilever interacts with the surface. The photodetector is divided into four quadrants, labeled A, B, C, and D as in Figure 22. The vertical and torsional deflections of the cantilever can then be measured by taking the signals (A+B)-(C+D) and (A+C)-(B+D) respectively.

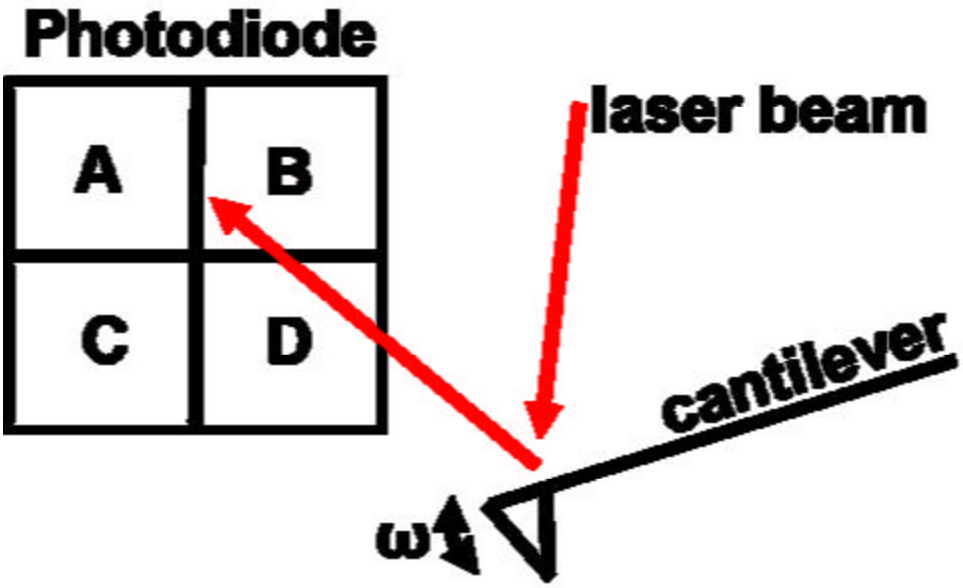

Figure 22. Laser reflecting off of SPM cantilever onto 4-quadrant photodetector.

In this work, the AFM imaging used is called alternatively "TappingMode™", "intermittent-contact", and "ac mode." This mode utilizes a cantilever which is excited at a frequency slightly lower than its resonant frequency, such that when it is brought into contact with the surface and feels the repulsive tip-surface potential, the resonance frequency increases, and the amplitude decreases. The piezos then act to move the sample and cantilever apart until a previously defined setpoint is reached. In cases of depressions on the surface, the total amplitude increases and the piezo tube acts to bring the sample and cantilever closer together. The topography of a

surface is then given by the voltage (which corresponds to a distance) on the piezo tube for each point in the 2-dimensional region being scanned.

Obviously, the feedback loop producing the topography information is very sensitive to the feedback parameters. The most user-dependent aspect of scanning probe microscopy is the tuning of the feedback parameters for acceptable topography images. Processing the information recorded in each scan of a surface is the last step in scanning probe microscopy. The information recorded for each surface is the voltage on the piezoelectric tube for each point on the surface being scanned; thus, the background, or flat surface, must be defined and gleaned from each individual scan.

The completed version of such a scan is shown in Figure 23. In this image, a carbon nanotube is shown along with the two alignment markers described in Chapter 2 and Appendix 1. Even without reference to external fiduciary marks, this single image can accurately locate the nanotube within the coordinate system of the alignment marks. The CNT diameter can be determined by taking successive line traces and comparing the CNT height, or diameter, to the flat silicon dioxide surface on which it lies. The evaporated metal alignment markers provide a further calibration and/or reference as their thickness is known independently.

Figure 23. Atomic force microscope image of alignment markers and carbon nanotube. The nanotube has a smaller height profile than the Cr/Au alignment markers, as indicated by the grayscale color of the CNT.

Electrostatic force microscopy

The use of scanning probe microscopes extends beyond simple topography. The interaction of the cantilever with the sample is not limited to mechanical means. The cantilever can also be coated with a metal to allow for an entire range of techniques that fall under the moniker of conducting-tip atomic force microscopy. These tend to be long-range interactions of the cantilever with assorted electric fields being produced at or near the surface under investigation. The cantilever can also be coated with a ferromagnetic material to perform magnetic force microscopy, but this application will not be discussed here.

Electrostatic force microscopy (EFM) is the moniker used to describe this non-contact, long-range mapping of the electric field on a sample. This technique relies on placement and control of the cantilever at a fixed distance above the surface, regardless of topography. This is described schematically in Figure 24. An initial

scan of the surface maps out the topography for an individual line scan, while a subsequent pass lifts the cantilever at a fixed distance above the surface while tracing out the topography determined in the preceding scan.

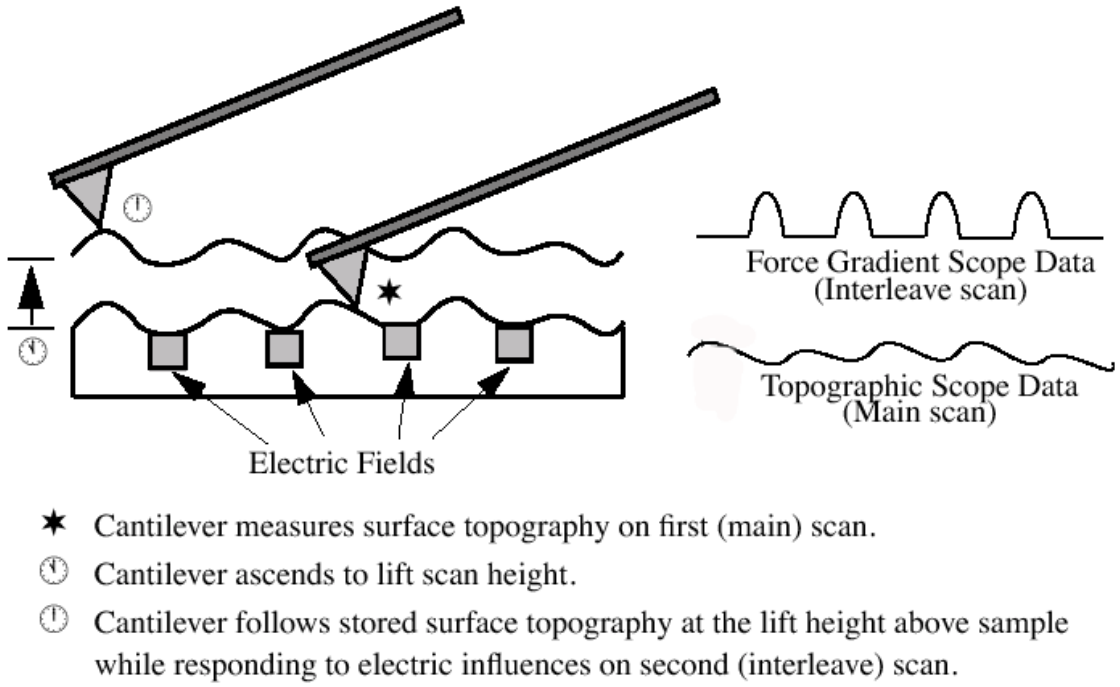

Figure 24. Schematic describing the "lift" scan which enables electrostatic force microscopy (EFM): In a separate "interleave" scan following a conventional topography scan, the cantilever traces out the topography of the previous scan at a fixed above the sample surface. Image courtesy of Digital Instruments Veeco Metrology group.

The long range forces which drive the cantilever at its resonant frequency are electric and derive from the expression for the force, $F = -\frac{dU}{dz} = -\frac{1}{2}\frac{dC}{dz}(\Delta V)^2$, where F is the force on the cantilever, U is the energy, z is the direction normal to the sample surface, C is the capacitance between tip and sample surface, and V is the potential. This comes from the expression for the energy stored in a capacitor. Expressing the voltage with both DC and AC components, $\Delta V = \Delta V_{DC} + \Delta V_{AC} \sin wt$,

substituting this into the force equation, and utilizing the relation, $2\sin^2 x = 1 - \cos(2x)$, gives $F = -\frac{1}{2}\frac{dC}{dz}(\Delta V_{DC}^2 + \frac{1}{2}V_{AC}^2) + \frac{dC}{dz}\Delta V_{DC}V_{AC}\sin wt + \frac{1}{4}\frac{dC}{dz}V_{AC}^2\cos 2wt$. If the sample is driven with a frequency, w, equal to that of the resonant frequency, w_0, of the cantilever, the cantilever response at w_0 is such that the amplitude at the photodetector is proportional to the electric field at a given location. The lift mode serves to keep the capacitive gradient constant while a separate scan with the entire sample at $\boldsymbol{V_{AC}}$ allows for calibration of the overall cantilever response.[100] A graphical depiction of the technique appears in Figure 25.

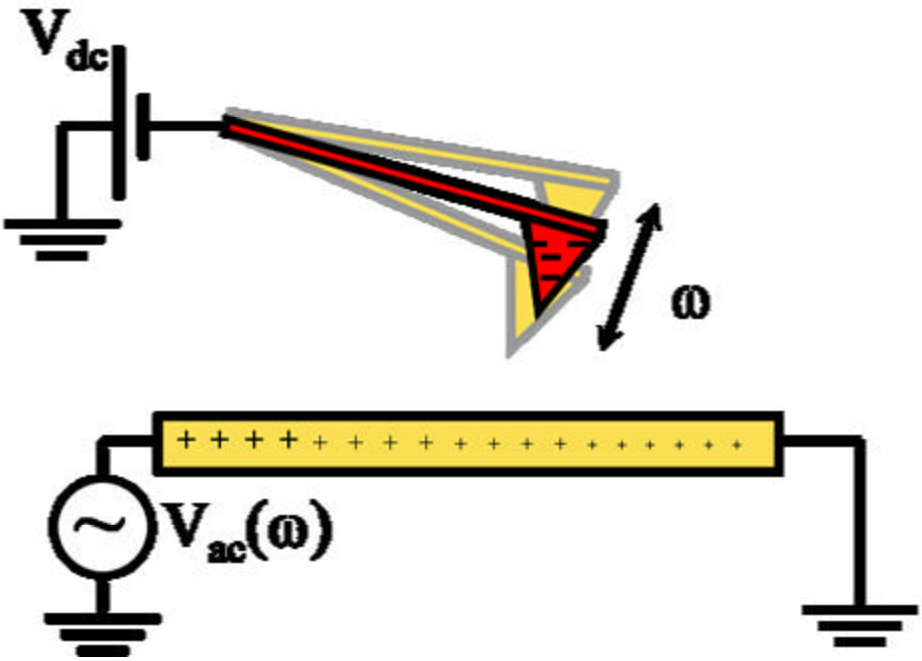

Figure 25. Electrostatic force microscopy: The cantilever is held a set distance above the surface of the sample. The piezo drivers are turned off so the cantilever is not oscillating. An ac bias at the resonant frequency of the cantilever is applied to the sample while a larger dc bias is applied to the conducting tip. The cantilever oscillates proportional to the local electrostatic potential as described in the text.

An image of an EFM scan is given in Figure 26. This is a two-dimensional map of the electrostatic potential acquired using the means described in the preceding paragraphs. This image is of a large gold electrode, the large rectangle oriented diagonally, attached to a CNT, which begins underneath the electrode and extends to the bottom of the image. The electrode is biased at 400mV. The CNT seen underneath the electrode is grounded through another electrode outside the scan range depicted in the image. This image shows the electric potential at each point as reflected in the amplitude response at the photodetector. The line scan depicts the potential difference at both the large gold electrode and the CNT. With the entire device biased at 400mV, the increased capacitance between the cantilever and electrode (or decreased capacitance between the cantilever and the CNT) can be subtracted. A large potential drop at the contact implies a large contact resistance while "transparent" electrodes show little to no transition between the electrode and the material being studied. Further explanation of background subtraction and EFM is provided in Appendix 2.

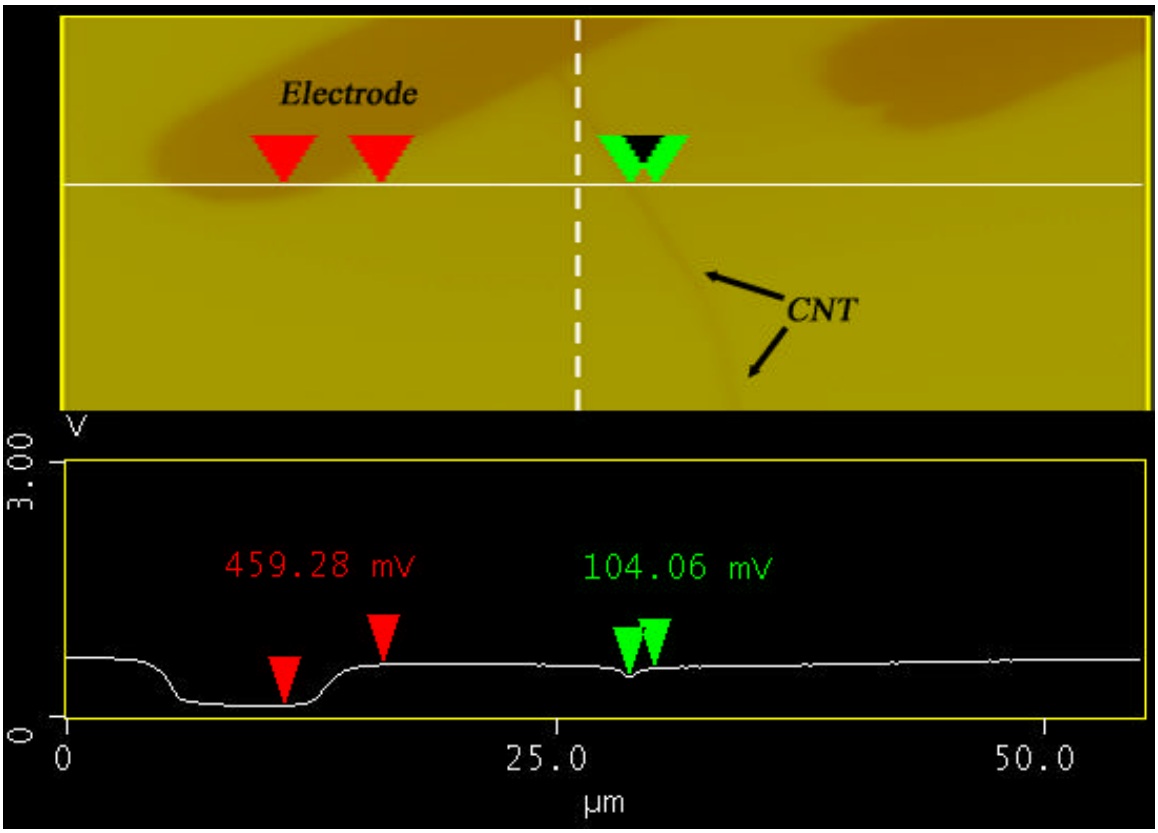

Figure 26. Electrostatic force microscopy image and line scan: The top image shows the amplitude measured at the photodetector for each point in the plane. The line scan below indicates the quantitative value at each point along the white line in the plane image above. The red and green arrows in the planar image correspond to those in the line scan while the values reflect the difference between each pair of arrows.

Contact resistance through EFM

EFM thus allows for a non-invasive detection of the contact resistance in a two-terminal device. If the two-terminal system is modeled as a series of resistors such that, $R_{tot} = R_{contact1} + R_{sample} + R_{contact2}$, the voltage drop at each contact is proportional to the contact resistance at the contact. A series circuit describing this concept is shown in Figure 27.

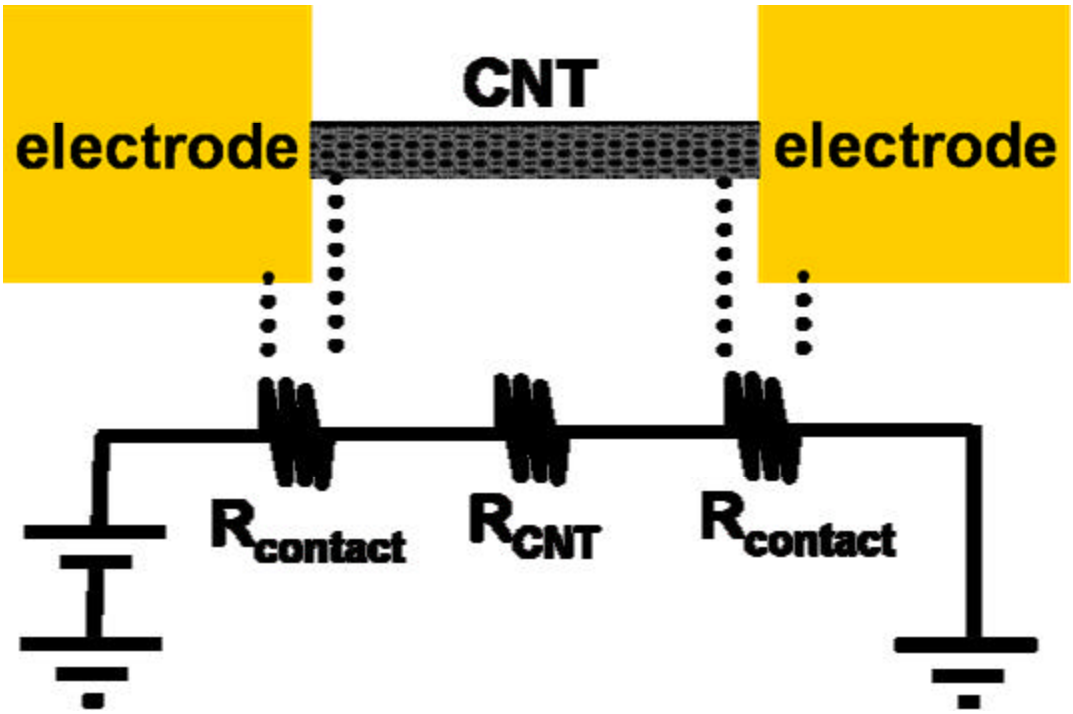

Figure 27. Contact resistance circuit for two-terminal CNT device.

This is an important tool for studying one-dimensional electrical transport as it is impossible to insert a "non-interacting", three-dimensional probe into a one-dimensional system. The typical technique for resistance measurement which avoids the influence of contact resistance involves insertion of a set of "voltage probes" into a system that is already being biased by another set of "current probes." This is known as a four-probe measurement. However, it is difficult to realize in a one-dimensional system because the voltage probes necessarily perturb the one-dimensional system: scattering from the one-dimensional system into the voltage probes is necessary to achieve chemical potential equilibrium, but also causes an increased resistance in the system being studied. EFM provides an electrostatic method to measure the potential along a current-carrying device, and is hence much less invasive (though it cannot be completely non-invasive, since the local charging of the device caused by capacitance to the tip is a perturbation). EFM will thus figure

prominently in Chapter 3 to determine the contact resistance of solid gold leads deposited by use of a focused electron beam.

Chapter 3: Imaging of carbon nanotubes on insulating substrates using scanning electron microscopy

While very effective, using an SPM to assay the production of CNTs or their placement on a substrate is time-consuming, and is often a bottleneck in CNT device research. In this chapter, I show how a scanning electron microscope (SEM) can also image the locations of CNTs. This technique benefits from the quicker scan rates and acquire times of an SEM, typically 2-3 orders of magnitude quicker than an SPM. Additionally, an SEM shows the electrical connectivity of CNTs to each other and any metallic leads. The technique relies on the differential charging of the conducting CNTs and insulating substrate, and is therefore much more robust to surface defects and contamination than the SPM. It also allows for CNT characterization where SPM is not applicable. I present and describe the technique in this chapter along with supporting images and a general description of the usefulness of the technique.

Figure 28a) is an SEM image of a CNT spanning two different substrates. Fabrication of similar devices is detailed in Chapter 6, but the images are provided here in light of discussion of the imaging of CNTs in an SEM. The contrast in this image is as-produced. No conducting coating is used on the sample in this image, or any other sample discussed in this chapter. This is noteworthy, as thin layers of metal or carbon are often used to decrease surface charging in insulating samples[101]. The CNT is clearly visible on the oxide at the top and bottom of the image. It is difficult to discern the CNT in the middle of the two substrates however. The number of secondary electrons collected, as reflected in the overall brightness, is less when the beam is scanning over the suspended portion of CNT than when over substrate-bound

portions of CNT. To see that there truly is a CNT spanning the two substrates, the contrast is enhanced for the middle region in Figure 28b). This is evidence that the primary mechanism for contrast production does not rely on secondary-electron production in the CNT due to interaction with the primary electron beam. Instead, as will be explained below, the increased contrast can be entirely explained by differences in surface potential of the SiO_2 substrate due to the presence of the conducting CNT which arise dynamically under the electrical charging induced by the primary electron beam.

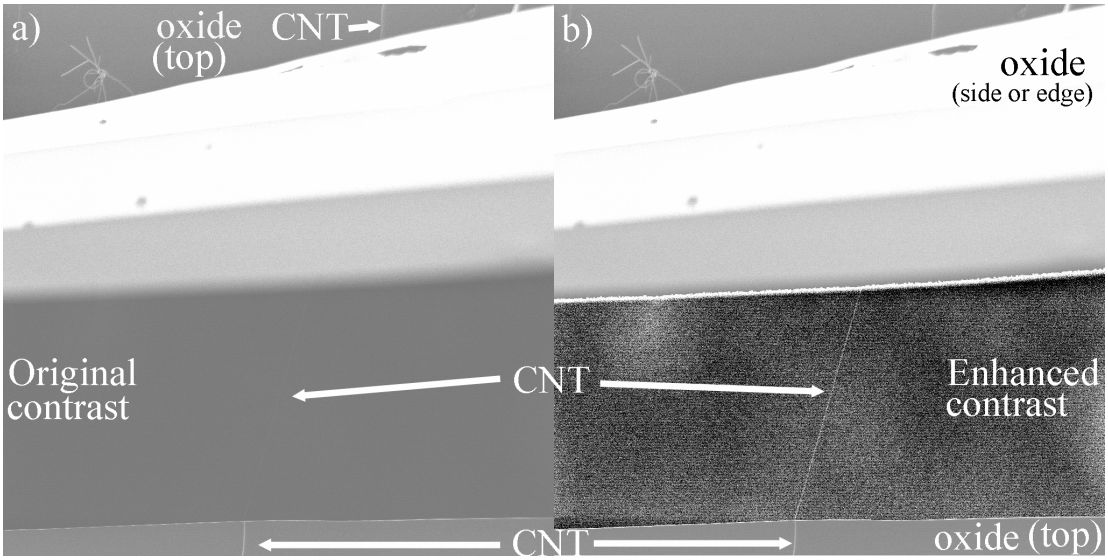

Figure 28. SEM images showing dissimilar contrast for suspended vs. substrate-bound CNTs: Parts a) & b) are the same images with different processing. Part a) is the unprocessed image of a CNT suspended above a trench while being anchored on the substrates at the top and bottom of the image. The CNT shows little to no contrast with the background in the trench; thus, less secondaries are being produced in this region. Part b) shows the same trench region, but here the contrast has been enhanced.

Lastly, it is worth noting that Figure 28 demonstrates an additional advantage of the ability to image CNTs via SEM; such an image would be difficult or impossible in an SPM as the trench in the middle is much deeper than the 'Z range' of a typical SPM.

The CNTs devices featured in the rest of the chapter were synthesized following procedures described in Chapter 2; however, the previous example is provided as a starting point to understand the overall contrast mechanism. As described previously, the process tends to produce 1-5 nm diameter, ~1-100 μm-long CNTs distributed randomly on the surface. In order to locate individual CNTs, alignment markers are placed on the substrate in a pattern resembling Figure 17. Before the development of the SEM technique to image CNTs described here, the atomic force microscope (AFM) was the standard tool used to locate CNTs relative to alignment marks in our research group and in other groups. This would tend to be the most time consuming step in fabricating individual CNT devices, prompting an exploration of other imaging techniques. As mentioned, AFM also has inherent restraints on depth profiling that SEM does not.

To further explore the contrast mechanism of CNTs in an SEM, Figure 29a) shows two sets of CNTs and alignment markers taken with an SEM, while Figure 29b) shows characterization using intermittent-contact mode AFM. Two isolated, individual CNTs may be seen in each image as well as the Cr/Au alignment markers. The CNTs and alignment markers lie on 500 nm of SiO_2.

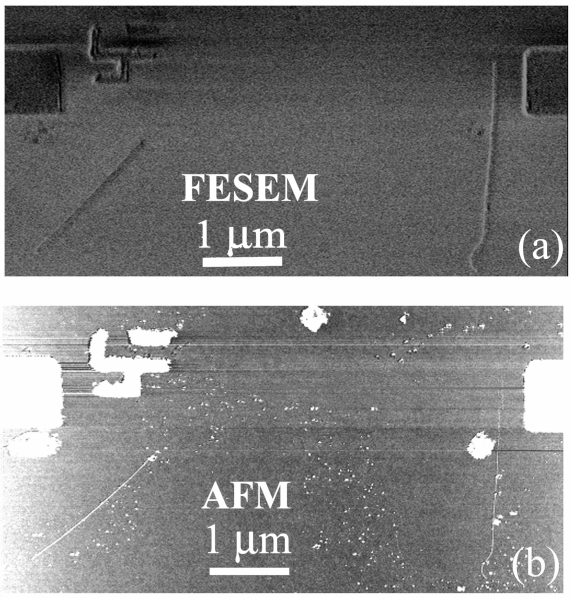

Figure 29. Comparison of atomic-force microscope (AFM) and field-emission scanning electron microscope (FESEM) images of the same CNTs. (a) Zeiss DSM982 FESEM operating at 1kV with 20 pA beam current using in-lens secondary electron detector. The entire 12 x 12 µm^2 image was acquired in ~10 seconds; a portion is shown. (b) Topograph from JEOL JSPM-4210 AFM operating in intermittent-contact mode. The entire 10 x 10 µm^2 image was acquired in ~700 seconds; a portion is shown. Both images show two isolated CNTs (lengths 2 and 3 µm, and diameters 2.2 and 0.9 nm, respectively, for the left and right CNTs), as well as 1 µm^2 gold pads and gold alignment markers.

In the SEM scan, the CNTs appear in the same location as in the AFM scan, but their apparent diameters (~50 nm) are much larger than the AFM height profile indicates (1-2 nm), in fact, they are larger than the spot size of the electron beam. This follows the results of Figure 28. Also in Figure 29, the general surface contamination appearing in the AFM image does not appear in the corresponding SEM image. This behavior is seen often and is a common feature of our AFM vs. SEM images of CNTs on insulating substrates: SEM detects contrast for conducting areas on the substrate (corresponding to the CNT location), but not for other non-conducting areas, even those with considerable surface roughness. These facts

further suggest that the contrast mechanism does not depend on direct interaction of the primary electron beam with the carbon atoms of the CNT or surface contaminants, which are likely organic polymer resist residue and/or amorphous carbon.

Figure 30 offers additional insight into the mechanism by which the SEM image contrast arises. This figure shows an SEM image of a CNT connected to a gold pad on top of the silicon dioxide, but isolated from the grounded, conducting silicon beneath. The beam is scanned from left to right at a linear speed of ~500 μm/s, and sequential line scans are taken from top to bottom. I draw attention to two line scans, represented by the horizontal arrows in Figure 30. In the upper line scan, a CNT is scanned without simultaneously scanning a large conducting pad; the CNT appears brighter than the surrounding substrate. In the lower line scan in Figure 30, a large pad is scanned previous to a CNT connected to that pad. The CNT now shows the opposite contrast, appearing darker than the surrounding substrate.

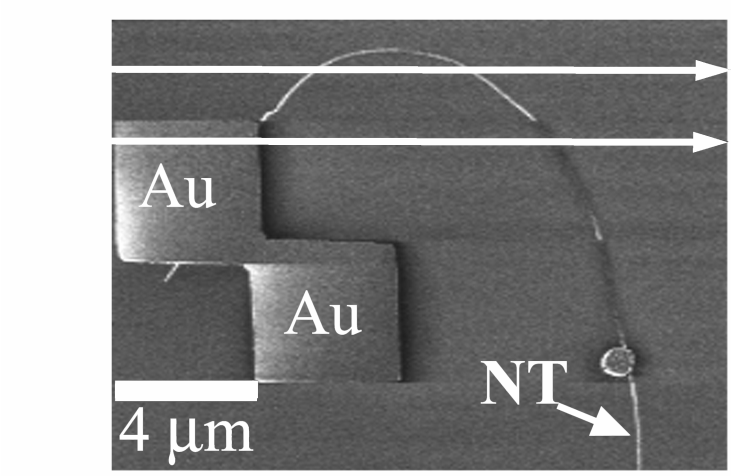

Figure 30. FESEM image of CNT connected to a gold pad. The beam is moving left to right at a linear speed of ~500 μm/s, and slowly from top to bottom. The horizontal arrows draw attention to particular scan lines: during the line scan corresponding to the upper arrow, the beam crosses the CNT, but not the gold pad. The CNT appears brighter than the surrounding oxide substrate. During the line scan corresponding to the lower arrow the beam crosses the gold pad before crossing the CNT, and the CNT appears dark in comparison with the surrounding oxide.

Contrast mechanism

First we discuss secondary-electron generation in insulating SiO_2 and detection by the SEM to produce an image. Figure 31 shows the ratio s of emitted secondaries to incident primaries as a function of primary beam energy E_0 for different thicknesses of silicon in steady state. In general, s (E_0) shows a peak at low energies where $s > 1$, and decreases to $s < 1$ at energies above the "second crossover" of SiO_2 ($E_{2C,SiO2}$).[102,103] When the primary beam initially interacts with the SiO_2 substrate, the s (E_0) curve is similar to the thin SiO_2 (d = 10 nm) curve. However, if s differs from unity, charging of the substrate occurs. For $s > 1$ ($E_0 < E_{2C,SiO2}$) the substrate charges positively. This reduces the effective energy of the primary beam until, for thick substrates, equilibrium is achieved at s = 1; this occurs at a substrate potential $eV_{substrate} = E_{2C,SiO2} - E_0$ at which the effective incident beam energy is $E_{2C,SiO2}$. For thinner substrates the equilibrium potential may differ from that above, in this case there is charge supplied by the conducting silicon under the SiO_2. For $s < 1$ ($E_0 > E_{2C,SiO2}$) the substrate charges negatively, again until $s = 1$ and $eV_{SiO2} = E_{2C,SiO2} - E_0$. Thus the equilibrium condition for very thick oxides (i.e. charge cannot be replenished from the substrate) is that the ratio of secondaries to primaries is constant.

In the typical operation of the scanning electron microscope, there is no intentional energy filtering, and the electron detector is held at a positive potential; essentially all secondaries that escape the surface are collected at the detector (in practice not all secondaries are collected, because some may have momenta such that

their trajectories take them to the wall of the chamber, etc.). Within the assumption that all secondaries are collected, there is *zero* contrast on thick insulating substrates in equilibrium; the number of secondary electrons is constant and equal to the number of primary electrons.

SEM imaging on insulating substrates must then be performed out of equilibrium, i.e. when the substrate is still charging dynamically. The time to reach equilibrium depends on the charging rate (given by the beam current, the dwell time, and the difference between s and unity) and the capacitance of the substrate. In practice, imaging of insulators is accomplished by increasing the time to reach equilibrium by operating close to $s = 1$, i.e. close to $E_0 = E_{2C,SiO2}$. Conducting objects can show contrast on thin insulators over a ground plane because their larger capacitance to the ground plane causes them to charge more slowly.

In light of the above, the contrast changes observed in Figure 30 are interpreted as follows. I assume that the production of secondaries by direct interaction of the electron beam and CNT is negligible (as supported by Figure 28) and that all secondaries which escape the substrate are collected at the in-lens detector, positioned directly above and parallel to the substrate. I further assume that the SEM is operating in the region $E_0 < E_{2C}$ (operating at $E_0 > E_{2C}$ would reverse the contrast in the images by a similar argument to that below, and which is in fact sometimes observed). In the top scan line, as the beam scans across the insulating SiO_2, the SiO_2 charges positively, reducing the number of secondaries, and $eV_{SiO2} \sim E_{2C,SiO2} - E_0$. However, when the beam reaches the location of the CNT, the SiO_2 in this region charges more slowly, as some charges can move to the CNT, which has

larger capacitance to the substrate. Thus the SiO_2 adjacent to the CNT has a relatively negative surface potential ($eV_{SiO2} < E_{2C,SiO2} - E_0$) compared to the surrounding substrate, and hence $s > 1$ in this region, and it appears relatively bright.

In the bottom line scan, the beam first scans the gold pad. The leading edge of the gold pad is bright, but as the beam continues to scan over the gold the brightness is reduced to that of the surrounding oxide, indicating that the gold charges to equilibrium. But in this case equilibrium is reached when the gold potential $eV_{Au} = E_{2C,Au} - E_0$, where $E_{2C,Au}$ is the second crossover energy for gold. We observe that the SiO_2 substrate on the trailing edge of the gold electrode appears dark: this indicates that $E_{2C,Au} > E_{2C,SiO2}$, such that the $eV_{Au} > eV_{SiO2}$ in equilibrium. In the region of the SiO_2 substrate near the trailing edge of the gold electrode the effective beam energy is larger because of the attractive potential of the gold; therefore $s < 1$ and the SiO_2 appears dark. The CNT is electrically connected to the gold pad, so it too is at a potential $eV_{Au} > eV_{SiO2}$, so the SiO_2 substrate around the CNT also appears relatively dark.

The observations above show clearly that differences in surface electrostatic potential, arising dynamically under charging by the primary beam, are responsible for the contrast between CNT and substrate observed in the SEM. This has important consequences. Decreasing scan speed, increasing magnification, or increasing beam current is found to *reduce* the image contrast. These changes all enhance the rate of charging, causing the CNT to come closer to potential equilibrium with the substrate, thus decreasing contrast. I also find that the image contrast is highest at beam energies $E_0 \approx$ 1-2 kV; dropping significantly for voltages > 3kV.

$E_{2C,SiO2} \approx 2$ keV, so at $E_0 \approx$ 1-2 kV the ratio of secondaries to primaries is nearest unity, and the rate of charging is slower.

Although samples contain both metallic and semiconducting CNTs, I have not seen evidence for two different types of CNTs in SEM images. The contrast mechanism requires that charge disperses along the CNT more rapidly than charge arrives at the CNT. To distinguish semiconducting from metallic CNTs requires that the charging times somehow differ in the two types of tubes. I estimate that the characteristic time for the CNT to reach potential equilibrium with the oxide is greater than 10 μs, the longest dwell time of the beam near the CNT for which contrast is still observed. Experimentally, measurements by myself and others in the group working with the same CNTs and substrates observe a resistance on order 10^5 Ω/μm at zero gate voltage for semiconducting CNTs, while the off-state resistance is typically $<10^{10}$ Ω/μm. The capacitance per length of the CNTs is approximately 10^{-17} F/μm, from which we obtain a time constant of $<10^{-9}$ seconds for a 100-nm section of CNT (approximating the area over which secondary collection is affected by the surface potential). This is significantly less than the equilibration time, thus even the most resistive semiconducting CNTs should appear conductive.

A more rigorous estimate of the maximum resistance object observed by this technique would require more detailed knowledge of the proper length scale to consider above. However, the order-of-magnitude estimates above indicate the technique may be useful for discriminating between insulators and materials with low but finite conductivity (on order 10^{15} Ω/μm). In this light it would be interesting to

image low-conductance one-dimensional systems (e.g. DNA, or polymer fibers) using the same voltage-contrast conditions to see whether conductivity is detectable.

This imaging technique does have unique advantages. Figure 31a) shows a regular array of gold coordinate and alignment markers, some of which are connected to CNTs. The gold islands which are contacted by CNTs are brighter than uncontacted ones (compare markers indicated by lower two arrows). Following the rationale outlined in regards to Figure 30: because gold islands connected by CNTs have a larger total capacitance than uncontacted islands, the same amount of charge results in less change in potential. This produces a larger potential difference relative to the oxide, which produces more contrast. In Figure 31b), a low magnification image shows a rather long CNT shorting two gold leads between CNTs within the alignment mark grid and larger bonding pads (outside the field of view). The large wires and pads charge the connected CNTs, causing them to appear dark. This image displays the usefulness of such a connectivity probe for detecting long range electrical shorts: long conducting CNTs connected to metal pads may be imaged at very low magnification. Such large scan areas would be prohibitively time-consuming with conventional AFM scanning. The enhanced contrast for small conducting objects when they are connected by CNTs (e.g. Figure 31a) also hints that CNTs might provide an alternate conducting coating when spun on a non-conducting sample from solution; in some circumstances this may be less invasive than the evaporation of conducting films such as gold or carbon.

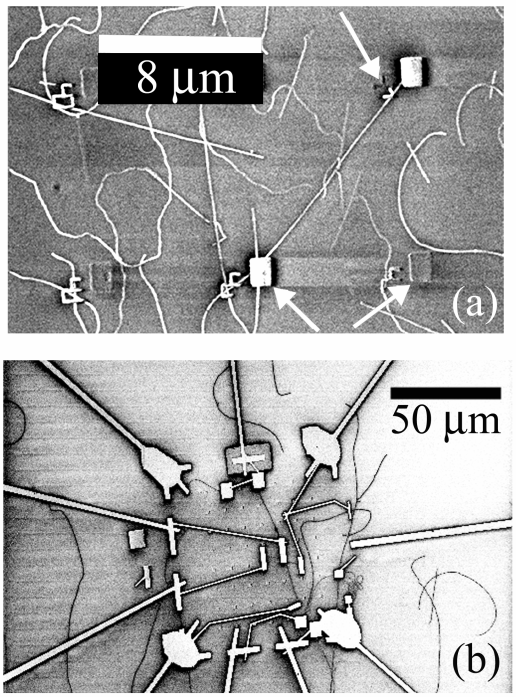

Figure 31. Electrical connectivity imaging with the FESEM. (a) Image of substrate with CNTs and a regular array of 1 µm^2 squares and coordinate markers. The squares which are contacted by CNTs show significantly greater contrast with the oxide substrate (compare markers indicated by two bottom arrows). Alignment markers which are not connected to CNTs are nearly undetected. The small symbols are made up of 150 nm wide gold lines. One symbol is connected to a CNT (arrow on upper right) and shows evidence of an electrical break: only a portion of the symbol shows contrast with the oxide. Scale bar = 8 µm (b) Low magnification FESEM image of substrate with large gold bonding pads and interconnects. A long-range electrical short caused by a single CNT is visible on the left side of the image. Scale bar = 50µm. Aside from a difference in background due to autocontrasting, a comparison of (a) and (b) also shows evidence for the contrast inversion displayed in Figure 29: the CNTs connected to large pads in (b) appear very dark after they have been charged by the beam, while the CNTs in (a) are lighter as they discharge to CNTs and pads outside the scan area.

Imaging long CNTs on insulating substrates at low magnification

Imaging of CNTs in the SEM has been used extensively by members of our research group[104] and other research groups[105] in locating and fabricating CNT devices that would be difficult or impossible to fabricate otherwise. One example is imaging and establishing electrical contacts to extremely long CNTs.[106] It has also been extended to the imaging of CNTs on single crystal quartz. Figure 32 shows an example of long CNTs on quartz, combining the two useful aspects of the technique:

low magnification imaging of long CNTs being done on a highly insulating a quartz substrate. This image shows the utility of the technique. It works even in a most challenging imaging environment: narrow diameter objects on highly insulating substrates at low magnification.

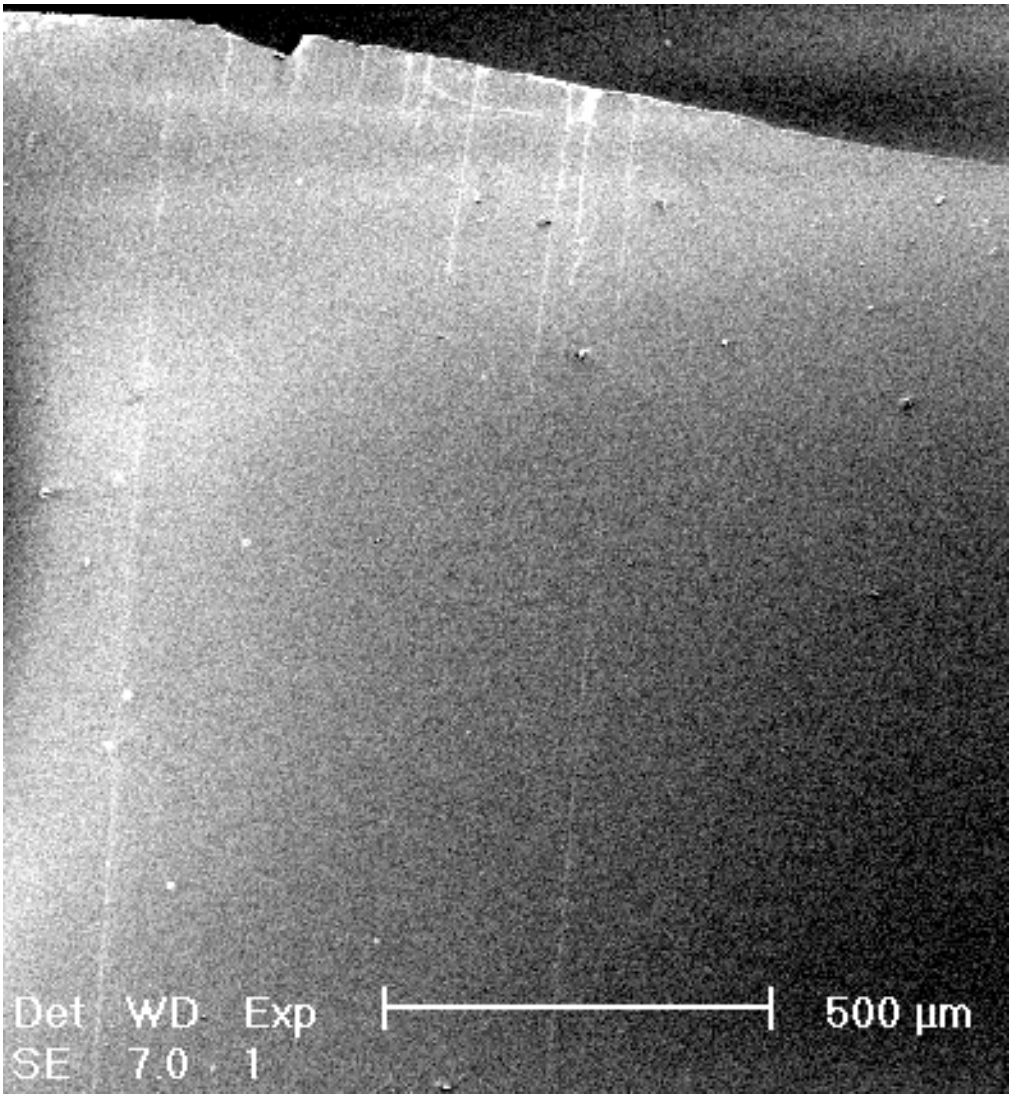

Figure 32. SEM image of long CNTs on quartz substrate: Even the low magnification and insulating quartz substrate do not prevent the CNTs from being imaged.

Chapter 4: High performance carbon nanotube transistors on $SrTiO_3$/Si substrates

As alluded to in previous chapters, one exciting promise inherent to CNTs is the possibility of using semiconducting CNTs as a replacement for, or complement to, silicon within a field effect transistor (FET) architecture. The intrinsic nanometer scale and pristine quality of the carbon lattice in SWNTs offers a great hope for a semiconducting, ballistic, easily manufacturable nanoscale material for use in FETs.[107] A quantifiable figure-of-merit that looks promising for such applications is the CNTs' room-temperature hole mobility: the highest recorded to date in any material[106] (in work conducted in this group at the University of Maryland). Hoping to further improve device performance, researchers have attempted to improve the performance of CNT-FETs by using thin, high-dielectric-constant (high-κ) dielectrics.[46,108,109] However, the presence of a Schottky barrier at the SWNT-metal interface has necessitated engineering solutions to obtain high transconductances, such as electrolytic gating[110] and local top-gating.[109] Ohmic contacts have also been achieved for the case of Pd[111] or Au[112] contacts and large-diameter nanotubes, but this solution may fail for the technologically-relevant small-diameter nanotubes that may be mass-produced.[111]

This chapter reports here the integration of high-k $SrTiO_3$ on Si substrates (STO/Si) with CNT-FETs, work published in Ref. 44. Complementing the aforementioned references on high-performance CNT-FET devices, the high transconductance per channel width (8900 $\mu S/\mu m$), limited number of lithography steps, and use of small-diameter CNTs described in this chapter indicate an alternate

avenue to Refs. 109-111 for high-performance CNT-FET fabrication. The chemical vapor deposition (CVD) described in Chapter 2 of high quality SWNTs on STO/Si leaves the STO/Si intact with its desirable properties, and the CNT-FETs demonstrate a high transconductance per width (8900 μS/μm), exceeding that reported for any other CNT-FET.[46,108,111,113-115] It will be shown that the increase in transconductance cannot be explained by an increase in the gate capacitance; the gate capacitance is largely limited by the quantum capacitance of the nanotube in our devices as well as other CNT-FETs on high-κ dielectrics.[46,108,116] I instead propose that the high transconductance of our devices is due instead to lowering or elimination of the Schottky barrier at the nanotube-metal interface by the high electric field at the dielectric-metal interface.

Device manufacture and strontium titanate characterization

The starting substrate consists of nominally 20-nm-thick epitaxial strontium titanate ($k \approx 175$) on ~500μm thick silicon. Details on the growth and characterization of $SrTiO_3$ on Si have been reported elsewhere.[117-119] SWNTs were grown by CVD following the procedures outlined in Chapter 2 excepting that substrates are strontium titanate on silicon instead of silicon oxide on silicon. However, alumina-supported Fe/Mo catalyst was patterned in islands on the substrate by electron-beam lithography closely following the procedures in Ref. 72 instead of randomly-dispersed iron nitrate catalyst. The alumina-supported catalyst was thought to reduce leakage through the $SrTiO_3$ dielectric observed when the randomly-dispersed iron nitrate catalyst was used. The reduced leakage could result from less diffusion of the catalyst when supported on alumina, or smaller surface area of

$SrTiO_3$ dielectric exposed to the catalyst. CVD synthesis was carried out in a 1 in. diameter tube furnace for 11 min at 900 ºC using a methane flow of ~1900 ml/min and a hydrogen co-flow of ~480 ml/min.

To ensure the STO/Si remained intact after growth, transmission electron microscopy (TEM) and electron diffraction were performed to confirm the integrity of STO following growth. In Figure 33a) the STO and Si are readily identified in the TEM micrograph, along with an amorphous layer between. In Figure 33b), the electron diffraction pattern shows both Si and the STO reproducing results[120] for untreated STO/Si.

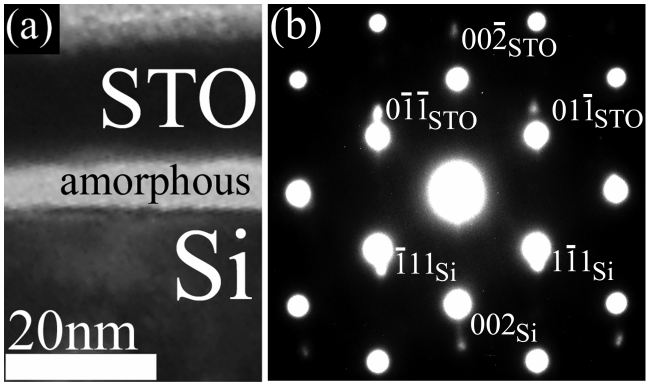

Figure 33. Transmission electron (a) micrograph and (b) diffraction pattern. In (a), the crystalline $SrTiO_3$, amorphous interface layer, and crystalline Si substrate are resolved in profile. In (b), two sets of diffraction spots reveal the presence of $SrTiO_3$ and Si.

Evaporated Cr/Au electrodes were used to make source and drain contacts to the SWNTs following the alignment and lithography defined in Chapter 2 and in Appendix 1. No annealing step was used to treat the electrodes. The Si served as a bottom gate electrode. The diameter *d* of each nanotube, determined from atomic force microscopy (AFM) described in Chapter 2, ranged from 1-10 nm. Presumably the sample comprises both single- and multi-walled nanotubes, but the smallest (*d* <

1.3 nm) nanotubes chosen for study of their device characteristics are most likely SWNTs.[121]

In Figure 34, FESEM and AFM micrographs illustrate nanotube growth from a catalyst island and the structure of the CNT-FET. In Figure 34a), one sees a rough catalyst island, two Au/Cr leads, and several nanotubes, one which spans the leads. Figure 34b) shows a similar nanotube device visualized by FESEM. In Figure 34c), the same area is imaged by AFM, more clearly resolving the nanotube. From the AFM topography, a diameter of ~1.0 nm is determined for this nanotube, indicating it is single-walled. The gate length is 1.8 μm. The dielectric integrity of the $SrTiO_3$ was verified by measuring the current-voltage characteristic from the large-area (2.4×10^4 μm^2) source and drain pads to the gate electrode for the device shown in Figure 34b) and (c). The gate leakage current does not exceed the noise level (~200 pA) for $V_s < \pm 2$ V, and rises exponentially with V_s for $V_s > \pm 2$ V, to 2×10^{-4} A/cm^2 at 4 V, comparable to published leakage currents for similar substrates.[117]

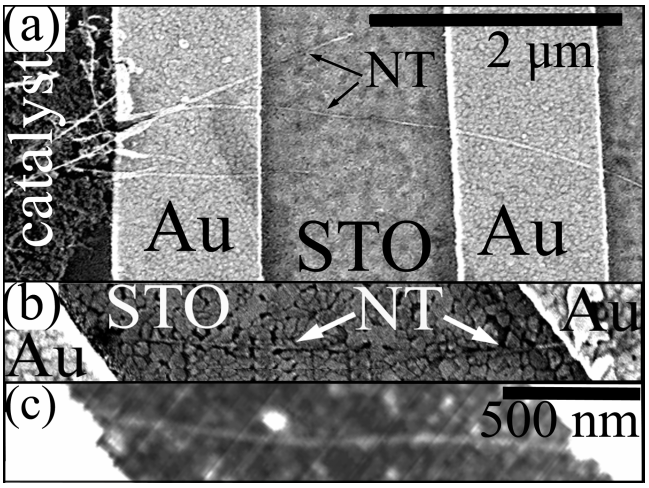

Figure 34. Images of CNT-FETs grown on SrTiO3 (STO) substrates by chemical vapor deposition. Part (a) shows patterned catalyst (left) on STO, as well as several nanotubes extending from the catalyst island. One nanotube has been contacted by two Cr/Au electrodes. (b) Field-emission scanning electron micrograph of a semiconducting nanotube on STO bridging two Cr/Au contacts with 1.8 um separation. (c) AFM image of the nanotube in (b), giving a CNT diameter of 1 nm.

Results

Figure 35 shows the drain current (I_d) vs. gate voltage (V_{gs}) of the device shown in Figure 34b) and (c). We numerically differentiate the data to calculate a transconductance.

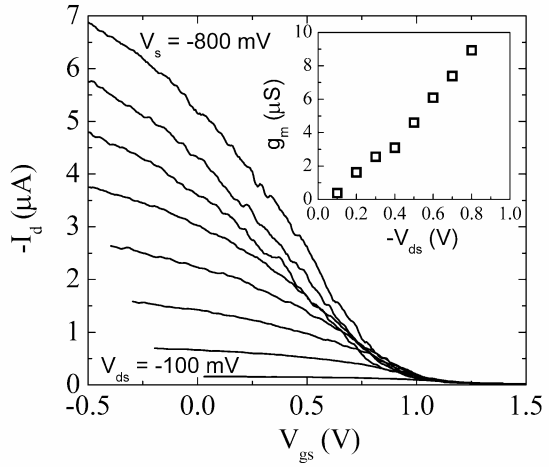

Figure 35. Drain current (I_d) vs. gate voltage (V_{gs}) at different bias voltages (V_{ds}) for a 1 nm-diameter CNT-FET. Inset shows peak transconductance (g_m) vs. V_{ds} through numerical differentiation of the curves in the main graph. The value g_m = 8.9 μS at 800 mV bias is one of the highest reported to date.

$$g_m = dI_d/dV_{gs}. \tag{4.1}$$

The $I_d(V_{gs})$ curves are sigmoidal, leading to a peak in g_m as a function of V_{gs}. The inset of Fig. 35 shows this peak value of g_m for each source voltage. The transconductance is approximately 8.9 μS at V_{ds} = -800 mV. This value exceeds any reported for a globally-gated solid-state CNT-FET[46,108,111,115] and is comparable to the value g_m = 12 μS at V_{ds} = -1200 mV for a locally-top-gated CNT-FET with ZrO_2 dielectric.[109] In order to compare this value with other transistor technologies, we normalize by the device width,[122] d. This leads to a transconductance per device width of g_m/d = 8900 μS/μm. As seen in Table 1, g_m/d exceeds all values in the literature for globally-gated CNT-FETs, and also exceeds that for the locally-gated CNT-FET[109] and electrolytically-gated CNT-FET.[110]

In a one-dimensional diffusive FET, the transconductance in the saturation region is given by

$$g_m \approx mc_g V_d/L, \tag{4.2}$$

where c_g is the gate capacitance per length. Thus for a given material system (with a given m) the transconductance can be increased through increasing c_g or V_d, or decreasing L. In practice, however, the product mV_d/L is expected to have a maximum value v_s,[104] the saturation carrier velocity, and the maximum transconductance is

$$g_{m,\max} = c_g v_s. \qquad (4.3)$$

This velocity has been measured by researchers in this group, and is shown to be 2 x 10^5 m/s. Thus increasing c_g becomes the goal for obtaining higher transconductance.

Comparison to previous results

Table 1 compares the performance of the CNT-FET on STO with other high performance CNT-FETs. The transconductance of our CNT-FET, 8.9 μS, is more than an order of magnitude greater than the values for CNT-FETs on Al_2O_3 and HfO_2 dielectrics, 0.3 and 0.6 μS respectively. However, these differences in transconductance observed in CNT-FETs cannot be explained by increased gate capacitances within the diffusive FET model, as follows. The electrostatic gate capacitance per length may be approximated by

$$c_{g,el} = 2\pi\kappa\varepsilon_o/\ln(4t/d) \qquad (4.4)$$

where t is the dielectric thickness, and κ the dielectric constant (this formula somewhat overestimates the capacitance, due to the lack of dielectric above the nanotube).

The total gate capacitance c_g must take into account the quantum capacitance c_q of the nanotube.[123-126] Quantum capacitance, also known as semiconducting capacitance, is an idea that was first proposed for mesoscopic systems and which

follows readily into carbon nanotubes; it measures the shift in Fermi level with addition of charge. Following directly from Ref. 110, quantum capacitance is simply $c_q = e^2 * g(E)$ where $g(E)$ is the density of states. For the CNT device here,

$$g(E) = \frac{8}{hn_f} \frac{\sqrt{E^2 - (E_g/2)^2}}{E} \tag{4.5}$$

where $E > E_g/2$ is the energy of the electron measured relative to the center of the band gap. For occupancy in one subband, a fair assumption here and near the band edge, $c_q = 8e^2/hu_f$ = 4pF/cm. Taking this capacitance into account, the total capacitance to the gate, c_g becomes

$$c_g = c_{g,el}c_q/(c_{g,el} + c_q), \tag{4.6}$$

Thus c_g is dominated by the smaller of $c_{g,el}$ and c_q; as $c_{g,el}$ is increased, c_g tends to the value 4 pF/cm. Table 1 gives values for t, d, L, V_{sd}, $c_{g,el}$ and c_g. For the high-dielectric-constant devices,[46,108,109] $c_{g,el}$ is comparable to or exceeds c_q, and hence c_g is on order c_q. Thus the observed ~15-30x variation in g_m cannot be explained by a ~3-5x variation in c_g in the standard, diffusive FET model. If we further consider that the transconductance has not reached its saturation value in our experiment or in Refs. 108 or 46, the greater L and smaller V_d of our device compared to those in Refs. 108 or 46 should result in an even lower transconductance. For short devices, the calculated mobility is not constant, but gets smaller with smaller L, (like 1/L presumably) and greatly underestimates the true CNT mobility. This also indicates that contacts dominate and L is unimportant.

Table I: Device parameters for high-transconductance nanotube field-effect transistors in this work and other works. The columns display the dielectric material and dielectric constant κ, dielectric thickness t, nanotube diameter d, gate length L, electrostatic gate capacitance $c_{g,el}$, total gate capacitance c_g, transconductance g_m, source-drain bias V_{sd} and transconductance per width. The symbol ‡ denotes electrolytic gating, * local top gating, and † Ohmic contacts.

Author	Dielectric (κ)	t (nm)	d (nm)	L (μm)	$c_{g,el}$ (pF/cm)	c_g (pF/cm)	g_m (μS)	V_{ds} (V)	g_m/d (μS/μm)
Appenzeller (Ref. 46)	HfO_2 (11)	20	1-2	0.3	1.6	1.1	0.6	-1.5	300-600
Bachtold (Ref. 108)	Al_2O_3 (5)	2-5	1	0.2	0.9-.3	0.7-1.0	0.3	-1.3	300
This work	$SrTiO_3$ (175)	20	1.0	1.8	22	3.4	8.9	-0.8	8900
Javey* (Ref. 109)	ZrO_2 (25)	8	2	2.0	5.5	2.3	12	-1.2	6000
Rosenblatt‡ (Ref. 110)	Electrolyte (80)	~1	3	1.4	70	3.8	20	-0.8	6700
Javey† (Ref. 111)	SiO_2 (3.9)	500	3.3	0.3	0.34	0.31	5	-0.6	1540

The failure of the diffusive FET model in CNT-FETs is not surprising; as other researchers have pointed out, the transconductance of CNT-FETs is often controlled by Schottky barriers at the nanotube-metal interface. This readily explains the much higher transconductances observed in Refs. 108 and 46, where the effects of the Schottky barriers at the nanotube-metal contact were circumvented through local-top-gating or Ohmic contacts to the nanotube, respectively. A simple electrostatic model predicts that the transconductance for Schottky-barrier CNT-FETs scales as the inverse square-root of the dielectric thickness, $g_m \sim t^{-1/2}$, and surprisingly is independent of the dielectric constant where the effect of a high-k/low-k interface at the position of the nanotube is found to decrease the effective gate voltage by at most a factor of ~2.[127]

This result is also inadequate to explain the differences in transconductances[18] in Table 1; our device has t comparable to or larger than Refs. 108 and 46. One explanation for the discrepancy is that we have made Ohmic contact to the nanotube. This is in contrast to Schottky-barrier-FET behavior observed for similarly small d nanotubes in Ref. 46, and as-deposited (not annealed) Cr/Au contacts in Ref. 112. It should be noted also that the subthreshold swing in the devices is ~400 mV/decade at room temperature, much larger than the 150-170 mV/decade observed for Ohmically-contacted CNT-FETs in Ref. 111, though this could also result from a larger interface trap density in $SrTiO_3$.

Another possibility is that vertical scaling has a pronounced effect on the Schottky barriers. The model of Ref. 46 may be inadequate for two reasons. First, Ref. 46 ignores the charge in the nanotube channel. A self-consistent treatment of charge in the on-state does show increases in device on-current for increased dielectric constants.[128] Second, Ref. 46 treats the nanotube as infinitely thin.

We expect that the details of the electric field at the contacts will be substantially modified when the effective thickness of the dielectric $t' = t/\kappa$ becomes significantly less than the nanotube diameter d (the dielectric constant of the nanotube is unity). In the devices described here, $t'/d \approx 0.1$, significantly less than the values of $t'/d \approx$ 0.2-0.6 and 1-2 in Refs. 108 and 46 respectively. (For typical devices fabricated on thick SiO_2, $t'/d \approx 100$.) When $t'/d << 1$, the potential drop *across* the nanotube diameter for the portion of nanotube underneath the electrode becomes a large fraction of the applied gate voltage.

This is depicted visually in Figure 36. When the voltage drop across the radius of the nanotube is equal to the Schottky barrier height, population of the valence band with carriers should become energetically favorable, allowing Ohmic contact with the channel. Stated another way, at moderate gate voltages the shift in electrostatic potential of the nanotube relative to the metal electrode can be greater than the Schottky barrier height, eliminating the barrier. In our devices this would occur at an applied gate voltage of a few hundred mV from threshold.

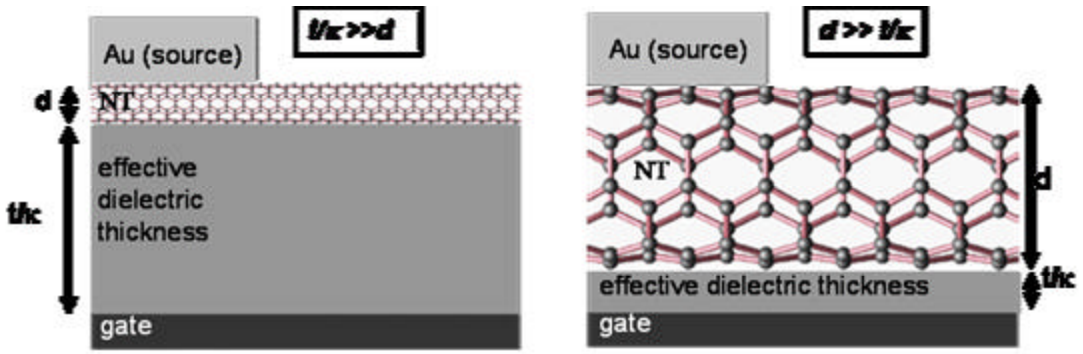

Figure 36. Visual model of different vertical length regimes within the Schottky barrier model. The left image shows a picture of the length regime described in Ref. 46, while the right image describes the length regime in this work.

This model also offers an alternate explanation for the observation of high transconductances (even in small diameter nanotubes) in FETs with an electrolyte dielectric ($t'/d \approx 0.01$).[110]

Chapter 5: Electrodes for carbon nanotube devices by focused-electron-beam induced deposition of pure gold

The carbon nanotube devices[113,114,129] described thus far rely on conventional electron-beam or optical lithography for their manufacture, for details see Chapter 2 and Appendix A. As can be seen in its description, this type of lithography requires nominally flat substrates for resist spinning, constraining many CNT devices to two-dimensional (2D) templates; etchants can free the CNT-metal devices, but the initial template remains essentially 2D. However, interesting new devices based on the mechanical or electromechanical properties of nanotubes[16,60,130,131] or nanotubes as electrically-active scanned-probe elements, will require new methods of making electrical and mechanical connections on three-dimensional (3D) structures. Of similar importance, exposure to air, water, and other gases, as well as solvents and resists, affects the substrate/CNT/contact interface and device performance[132] making *in situ*, pristine contact desirable to study inherent CNT behavior absent impurity effects. The focus of this chapter is studying the use of focused electron beam induced deposition (FEBID) as a possible means to overcome the aforementioned problems associated with conventional electron beam and optical lithography.

Focused-electron-beam induced deposition

FEBID is a direct-writing method of making electrical contacts using a scanning electron microscope and a variety of metal-containing precursor gases. In essence, a beam of focused electrons is used to dissociate or dissemble the metal atoms from a metal-containing precursor gas. After dissociation, the metal atoms aggregate on or near a substrate surface. This aggregation is controlled by the

location of the electron beam; thus, the process results in metal lines at pre-defined locations on, or above, a substrate through control of the beam path during writing. The actual mechanism behind this dissociation encompasses a separate, ongoing research effort and will not be addressed here.

Similar to FEBID, focused ion beam (FIB) induced deposition[133] has also been used for *in situ* contacts to CNT devices,[134] but FIB damages CNTs and affects the substrate/CNT/contact interface through momentum transfer and ion implantation.[134,135] Environmental electron-beam-induced deposition (EEBD) of gold-carbon composites to multi-walled nanotubes (MWNTs) has also been demonstrated in the making of *in situ,* 3D CNT devices with good contact resistances.[136,137] However, EEBD requires high (> 0.8 torr) water vapor pressure, undesirable for pristine CNT devices, and has been studied using only large-diameter MWNTs, not the more technologically-interesting SWNTs, which can be mass-produced and more reliably controlled for chirality type.[54,55,73,81,84,138-143]

These considerations lead to the employ of FEBID to make contact to individual metallic single-walled carbon nanotubes (SWCNTs). Of note, the precursor gas used to provide the metal for the contact is an inorganic metallic molecule, chloro(trifluorophosphine)gold(I) or $AuClPF_3$,. This molecule avoids the co-deposition of a carbonaceous matrix which occurs with the more common organometallic precursor gases.[144-148] It also has an advantage over EEBD in that it takes place in high vacuum.[147,149] Some current uses include *in situ* fabrication of magnetoelectrical devices[148] and nanoscopic 4-point thermal measurements.[150] It will be shown in this chapter that SWCNT/FEBID-gold devices have equivalent one-

dimensional resistivities to SWCNT devices with chromium/gold contacts deposited using conventional electron beam lithography (EBL). Electrostatic force microscopy (EFM), see Chapter 2 and Appendix 2 is used to directly measure the contact resistance between FEBID gold deposits and SWNTs, which is found to be comparable to or less than the contact resistance of electron beam lithography (EBL) defined electrodes on the same SWCNT.

Experiment

Using the growth procedure from Chapter 2, we first deposit carbon nanotubes using chemical vapor deposition (CVD). The starting substrate is 500nm of wet-oxidized SiO_2 on degenerately doped silicon, where the silicon acts as a universal back gate allowing determination of metallic or semiconducting SWNTs after device manufacture. The catalyst is dispersed and precipitated iron nitrate, as described. The chips are then heated under argon to 900°C in a tube furnace, and the growth gases, ethylene, methane, and hydrogen at ~100, ~1300, and ~2000 sccm respectively, are turned on for 10 minutes after which the gases are turned off, and the chips are allowed to cool under argon. This chemical vapor deposition growth tends to deposit long (~1-300μm), randomly positioned SWNTs (diameter: ~1-3nm),[75,140] as seen previously.

Following SWNT growth, we use conventional EBL and lift-off methods to deposit chromium/gold bonding pads and leads on top of and near to SWNTs following procedures outlined in Chapter 2 and in Appendix 1. The pads and leads are thermally evaporated from 99.99% pure gold to typical thickness of 50-70 nm

after deposition of a 2-3 nm chromium adhesion layer. The geometry of the pads and leads together tends to incorporate 3-20 SWNTs per 1 mm x 1mm area that also includes 16 different leads attached to large bonding pads. The SWCNTs are then imaged using both scanning electron microscopy (SEM; Philips XL30 or Zeiss DSM982) to determine SWNT locations and atomic force microscopy (AFM; Digital Instruments Dimension 5000 or JEOL JSPM-4210) for SWNT locations and diameters before FEBID. Because FEBID entails simultaneous alignment with imaging and deposition happening concurrently, these steps may be either omitted or completed after SWNT device manufacture using FEBID.

We continue with the FEBID of gold leads to connect SWNTs to the EBL-defined gold leads, shown in Figure 37. Following Ref. 147, the sample is inserted into a scanning electron microscope dedicated for FEBID (Cambridge S100). A small syringe-like reservoir of chloro(trifluorophosphine)gold(I), $AuClPF_3$, is inserted into the SEM chamber. Deposition is done at room temperature, avoiding usage of heated stages and *in situ* annealing.[146,150-152] The precursor flux at the syringe exit was about $1x10^{17}$ molecules/cm^{2}s as measured from weight loss, and the backpressure during deposition was maintained at $6x10^{-6}$ mbar with a cryogenic cooling system. Imaging in the SEM follows. In Figure 37, the labeled CNT is visible at the top, bottom, and between the FEBID electrodes. It shows varying contrast due to the tilt of the SEM and the history of the beam scan; the CNT is charging and discharging the nearby substrate which causes the local contrast effect described in Chapter 3.[39] After finding locations for gold deposition on top of SWNTs, a lithography system (NPGS) controls the electron beam during FEBID. At an accelerating voltage of 25

kV and 100 pA beam current, the beam diameter is about 80 nm at the focus. The beam is scanned with 11.6 nm/s (corresponding to a line dose about 86 μC/cm or $5x10^7$ electrons/nm) across regions containing SWNTs attached to the surface, depositing solid gold leads on top of the SWNTs by stripping off all the ligands from the chloro(trifluorophosphine)gold(I) molecule releasing pure gold.[147,149] In Figure 37, these appear as ~150 nm wide and ~20 nm thick lines connecting the larger EBL leads with a SWNT. The inset is a higher magnification view of the region where the FEBID-gold attaches to the EBL contact. While it appears that it may be disconnected, it is still electrically conducting. Additional FEBID-deposited gold lines were also deposited between EBL contact pads without nanotubes, in order to investigate the resistivity of the FEBID gold deposit. After FEBID, the samples are removed from the SEM for further imaging and electrical transport measurements.

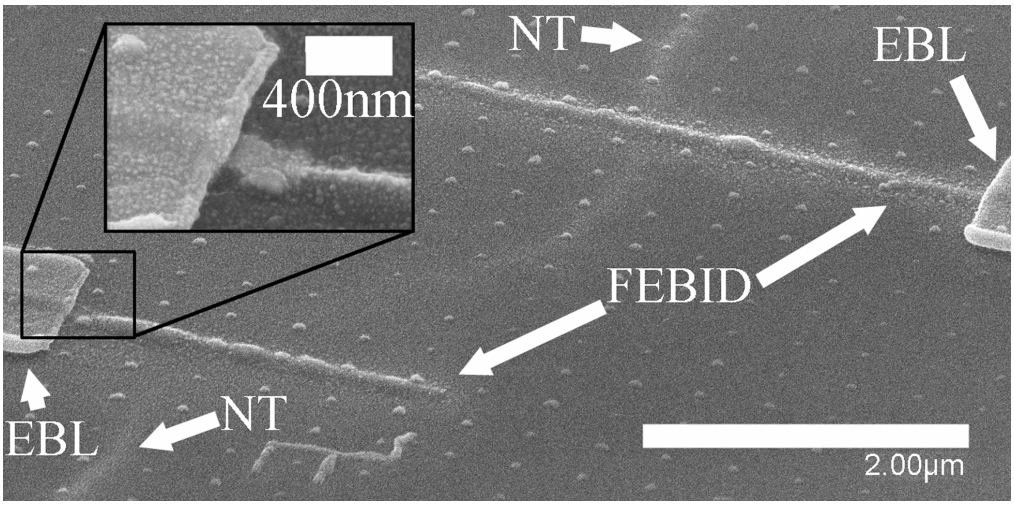

Figure 37. Carbon nanotube with focused electron beam induced deposition (FEBID) of gold lines on SiO_2. Large leads (~1µm wide; labeled "EBL") at left and right of image were pre-deposited using conventional electron beam lithography (EBL) and thermal evaporation. (An array of gold dots defined by EBL can also be seen; it is unrelated to this experiment.) Carbon nanotube (SWNT) runs from top to bottom of image. Focused electron beam induced deposition (FEBID) of ~150nm, solid gold lines (labeled "FEBID") was done in a scanning electron microscope to connect the SWNT to the EBL leads. Inset shows region of overlap between FEBID and EBL lead.

Results and discussion

Figure 37 also allows the resolution of individual grains of gold within the FEBID deposit, more easily seen in the inset of Figure 38. The ability to resolve individual grains with ~20-50 nm separation indicates lack of a carbonaceous matrix typical with organometallic precursor deposition, which prevents such resolution due to charging in the insulating carbon matrix.[149] A separate deposition from that of Figure 37 is featured in Figure 38. A high-magnification image showing gold grains formed in this separate deposition is in the inset. Figure 38 also shows energy dispersive x-ray analysis of the FEBID-gold lines with strong gold M-line peaks at 2.20 keV for both FEBID and EBL gold and negligible/non-existent signatures for the non-gold inorganic precursor elements, fluorine and chlorine, at 0.7 and 2.7 keV, respectively. As a phosphorus K peak at 2.05 keV would overlap the large Au band,

the presence of some P impurities cannot be excluded, but would correspond to low concentrations (<10%). This is further indication of solid gold FEBID leads contacting the SWNT.

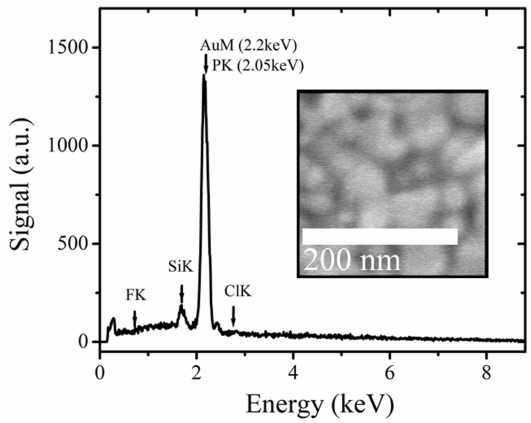

Figure 38. Energy dispersive x-ray analysis of focused-electron-beam-induced deposition (FEBID) of gold from chloro(trifluorophosphine)gold(I). Labelled peaks indicate the presence of gold (M-line), but little to no fluorine or chlorine. The presence of phosphorous can not be ruled out due to overlap with the M-line of gold. Inset is a high magnification scanning electron micrograph of individual grains of the analyzed deposition material. Such resolution (<50nm) also suggests pure gold deposits, see text for discussion.

Two FEBID gold lines connecting EBL pads without nanotubes were deposited at line doses of 86 μC/cm. These lines had resistivities of 43 $\mu\Omega$ cm (measured by two-point contact). We note that the resistivity value obtained at low dose is about three orders of magnitude lower than in Ref. 149 due to an improved precursor supply used in the present experiments, but remains ~20x larger than the resistivity of bulk or thin-film gold deposited by sputtering or evaporation.

After applying a bias voltage to such SWNT devices, we find one-dimensional resistivities of $r \approx$10-15 kΩ/μm for both lithographically defined and FEBID gold leads on the same SWNT. Also, the current changes little with variations in (back) gate voltage, indicating metallic SWNTs, with no significant change in behavior for

FEBID, FEBID/lithographic, or purely lithographic leads. These values represent measurements of several contact pairs fabricated on two long carbon nanotubes. Assuming a scattering length much less than the device length and a constant intrinsic resistivity in the SWNT, this equivalence in 1D resistivities indicates a rough equivalence in contact resistance, as discussed in Chapter 1. (The EBL lead includes a chromium adhesion layer in contact with the nanotube; however, other researchers have shown that chromium/gold contacts are similar to pure gold.[153]) We note that our 1D resistivities correspond to mean free paths $l = (2G_o r)^{-1} \approx 0.4\text{-}0.7$ μm, which is on order of, but somewhat lower than, estimates in the literature.[100,153-155] The lowest 3D resistivity of electron beam deposited leads reported to date is still 5-10x that of conventional gold[149] again making noteworthy the equivalence of FEBID gold and EBL chromium-gold displayed here on the same SWNT.

Figure 39 displays both topography and electrostatic force microscopy (EFM) images comparing FEBID contacts on a single SWNT also contacted using EBL gold leads. Topography scanning and EFM, as used here, are described in Chapter 2 and in Appendix 2. Figure 39 shows a topographical image of a SWNT, diameter = 1.4 ± 0.5nm, spanning an EBL lead at top left and a FEBID lead at the bottom of the image. Figure 39b) illustrates the simultaneously acquired electrostatic potential map using electrostatic force microscopy.

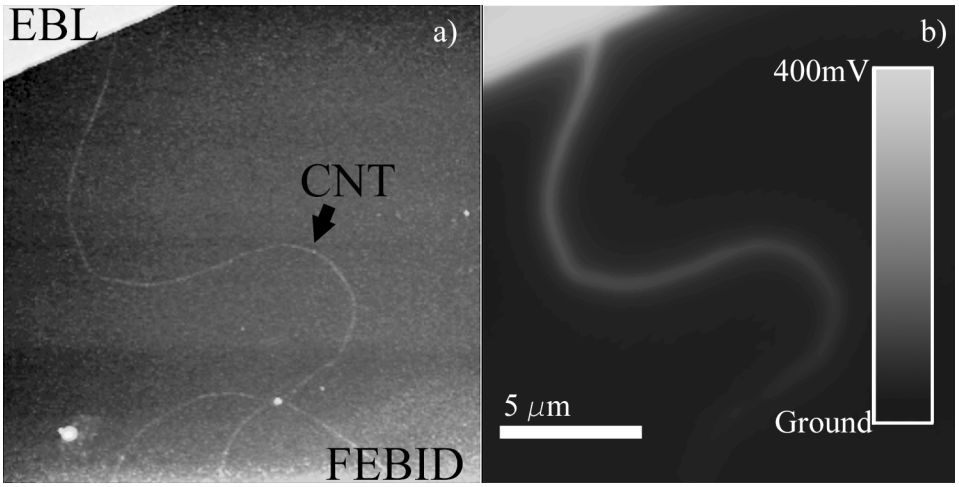

Figure 39. Scanning probe microscopy of single-walled carbon nanotubes (SWNT) device synthesized using both focused-electron-beam-induced-deposition (FEBID) and conventional electron beam lithography with thermal evaporation (EBL) of chromium-gold leads. (a) Topography image showing FEBID lead on the bottom and EBL lead at top left, heights = 5 and 20nm, respectively. Visible between the leads is a SWNT, height = 1.4nm. (b) Electrostatic potential map acquired simultaneously with (a) using electrostatic force microscopy. Brightness corresponds to potential at a given point, with a driving voltage of 400mV on the EBL lead.

Figure 40 plots the local electrostatic potential along the length of the tube, taken from Figure 39b). The red triangles and black squares represent a bias being applied to either the FEBID or EBL lead, respectively. The symmetry with respect to reversal of the vertical axis in these data (as expected for an AC bias voltage) is a useful check on the linearity of the EFM potential measurement. It also exhibits the CNT functioning in a diffusive regime as resistance drops along the length of the tube. The total resistance in this SWNT device is 430 $k\Omega$. The drop in potential at each of the leads quantitatively illustrates the contact resistance at that lead, 10 (±6) and 54 (± 6) $k\Omega$, for FEBID and EBL leads, respectively, with most voltage dropping across the long metallic SWNT. This is further verification of the two probe measurements already mentioned, which suggest that the contact resistance between SWNTs and FEBID materials is similar to that of thermally-evaporated EBL material. Of note, the contact resistance of the FEBID/SWNT junction is close to the

theoretical minimum for a single SWNT contact, $1/(4G_0) \approx 3\ \mathrm{k}\Omega$, where $G_0 = h/2e^2$ is the conductance quantum. Electrostatic force microscopy on the device in Fig. 37 (not shown) showed somewhat higher contact resistances (~100 $\mathrm{k}\Omega$), but again the FEBID contact resistance was less than that of EBL leads on the same SWNT.

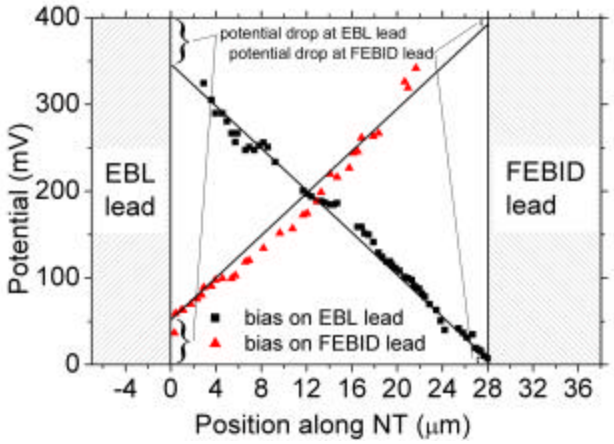

Figure 40. Electrostatic potential along length of carbon nanotube in Fig. 37. The red/triangles and black/squares are for biases applied to the FEBID and EBL lead, respectively. The symmetry indicates uniform response to local potential, regardless of bias or ground lead. The drop at the leads indicates 10 (±6) and 54 (± 6) k Ω contact resistances, for FEBID and EBL leads, respectively, with most voltage dropping across the long metallic SWNT, total resistance = 430k Ω.

Also of note, measurements of EEBD on MWNTs showed resistances of 9-29 $\mathrm{k}\Omega$ and no correlation with length,[137] indicating that the measured resistances were largely contact resistance to the (more conducting) MWNT. Such contact resistances are on the same order as in this experiment, even though the contact resistance to large-diameter MWNTs may in principle be much lower due to the larger number of 1D subbands available for conduction.

Summary

We have shown the conductance of SWNTs contacted through FEBID gold leads to be equivalent to EBL gold leads. Although not demonstrated here, this technique allows for *in situ* contact to SWNTs on not only 2D substrates, but in 3D architectures as well. FEBID can be performed without the application of resists or solvents to the SWNT, and it does not require a separate alignment step before contact is made. While FEBID is an unlikely candidate for large-scale production of SWNT devices (due to line doses that exceed conventional EBL doses by three or more orders of magnitude), we feel its equivalence to EBL gold leads for contacting SWNTs introduces a new tool for the broad and continuing research on the physics and applications of carbon nanotube devices.

Chapter 6: Long, suspended carbon nanotubes for electrical transport

As stated before, the two-dimensional nature of carbon nanotubes (CNT) makes them uniquely sensitive to their local environment. 'Bulk' values are difficult to define because CNTs can not be treated as having both surface *and* bulk values, as for crystalline materials that do. These values are synonymous in CNTs because they are surface-only structures. One striking example is the Luttinger-liquid interaction parameter *g*, which depends on the screening of the electrostatic interactions of the electrons even by very distant electrodes. This makes interactions between individual CNTs and their surrounding media important. It is also a major focus of present research on CNTs to quantify the effects of different environmental components on CNT behavior. This then allows numerical comparisons for improved device designs if improvements in FET performance are desired.[44,111,116,156-158] Another exciting aspect of CNT environmental response is in their use as sensors of charge or chemical species.[132,159-167]

Substrate effects

The supporting substrate, often serving simultaneously as gate dielectric, affects electrical transport through charge traps and residual adsorbates both of which change local electrostatic potential along the CNT.[43,168] Finally, the presence of contamination from processing on the CNT itself remains a concern in interpreting transport data on CNT devices. To study inherent electrical transport in CNTs

without interference from the above, we demonstrate the growth of individually addressable long, suspended carbon nanotubes without the use of etchants or resist.

The presence of charge traps in SiO_2 causes hysteresis in device behavior. This allows for single-electron memory in CNT-FETs,[43,168] but it also masks intrinsic CNT behavior through switching noise and quantization of the local electrostatic potential near the CNT. These values exceed the case in which the CNT breaks into multiple quantum dots due to variations in local potential along its length. This feature is intrinsic and is thus more of a concern than the switching noise. In work by Jarillo-Herrero *et al*,[169] semiconducting CNTs suspended above substrates in CNT-FET geometries displayed an absence of noise typical for substrate-bound CNTs so that individual holes and electrons can be seen entering the CNT acting as a Coulomb island. Cao *et al* also suspend tubes to study transport,[170] and there have been reports of Rayleigh scattering from individual suspended CNTs.[175] To extend work on long CNTs done by Dürkop,[106] we grow and study transport on CNTs in the diffusive regime ($L > 10$ μm) with a movable gate, allowing investigations of long, suspended CNT in the diffusive regime and with tunable gate capacitance.

Device manufacture

To eliminate contamination from resists typical for electron beam and optical lithography, evaporation of ~20nm x 120μm wide electrodes (Cr/Au, W/Pt, and W/Pd) is accomplished using stencil masks (commercially available copper grids fro transmission electron microscopy) on ~1 cm^2 substrates consisting of either 100nm SiO_2 on Si or quartz. The 500μm thick substrates are then cleaved leaving electrodes

extending to the edge. Following Chapter 2, one of these substrates is then dipped into a solution of iron nitrate in isopropyl alcohol (0.1-1 g/L), followed by a dip in hexanes. Using silver paint as an adhesive, both substrates (one dipped in solution, one not) are affixed to a third substrate leaving a 10-200 μm gap or trench between them, avoiding the use of etchants in the creation of the trench, and inserted into a tube furnace. Carbon nanotubes are grown using a methane-hydrogen-ethylene co-flow at 900°C following Kim *et al*. All growth happens at near ambient pressures and without the use of the fast-heating method of Ref. 171 and produces CNTs with diameter < 3nm.

Figure 41 shows the result of this process. Carbon nanotubes grow from catalyst particles and across trench and pre-deposited electrodes. In Figure 41a), a scanning electron micrograph displays a CNT crossing a ~120μm gap between two substrates with residual, out-of-focus silver paint visible on the underlying substrate 500 μm below the in-focus CNT; the Pd electrodes are also visible at top and bottom, reaching to the edge of each substrate. In Figure 41b), an optical micrograph shows Pd electrodes at top and bottom along with catalyst particles. We stress that this synthesis is entirely 'dry' after CNT growth, a quality of synthesis necessitated by evidence of the presence of contamination on wet-processed tubes changing the nature of electrical transport.[172] The overall length scale in these devices (L > 10μm) is also of note as the conventional micro- or nanoelectromechanical systems' wet-etch processing used in fabrication of micro- or nanoelectromechanical systems has proven difficult for for production of suspended CNTs for L > 10 μm, even with critical point drying.[173]

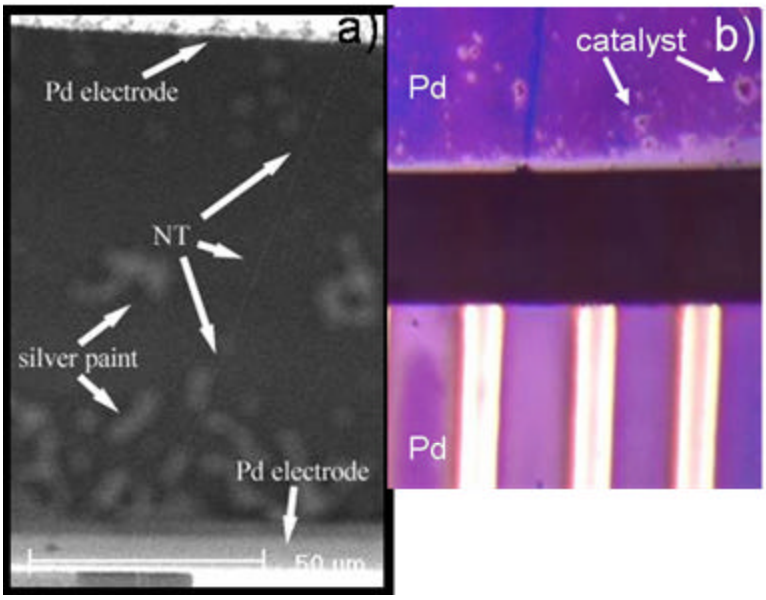

Figure 41. Long, suspended carbon nanotube devices. a) Scanning electron micrograph showing pre-evaporated Pd electrodes and CNT crossing trench. Out-of-focus silver paint used as adhesive is visible 500 μm below focal plane. Scale bar is 50 μm. b) Optical micrograph showing multiple electrodes and catalyst.

In Figure 42, the top/upstream substrate (100nm SiO_2 on Si) lies above the bottom/downstream substrate, both absent the electrodes present in Figure 41, demonstrating the three dimensional nature of CNT growth. Catalyst particles are visible on the top chip along with numerous CNTs with five CNTs spanning the length and height from the top chip to the bottom. The dark 'plume' at the point of CNT contact to the bottom substrate indicates an interaction between the CNT suspended above the surface and the secondary electron collection, obviously differing from that of the bright, substrate-contacted CNT. This is described schematically in the right hand image in a hypothetical side view. This suggests that CNT growth does not follow the surface topography, but rather that CNTs grow off the substrate and eventually fall onto the substrate and adhere. The adhesion energy of the CNTs to the substrate is significant,[174] and apparently produces suspended

CNTs that are always under tension as evidenced by the ubiquitous observation of straight CNTs crossing trenches (see e.g. Figure 42a).

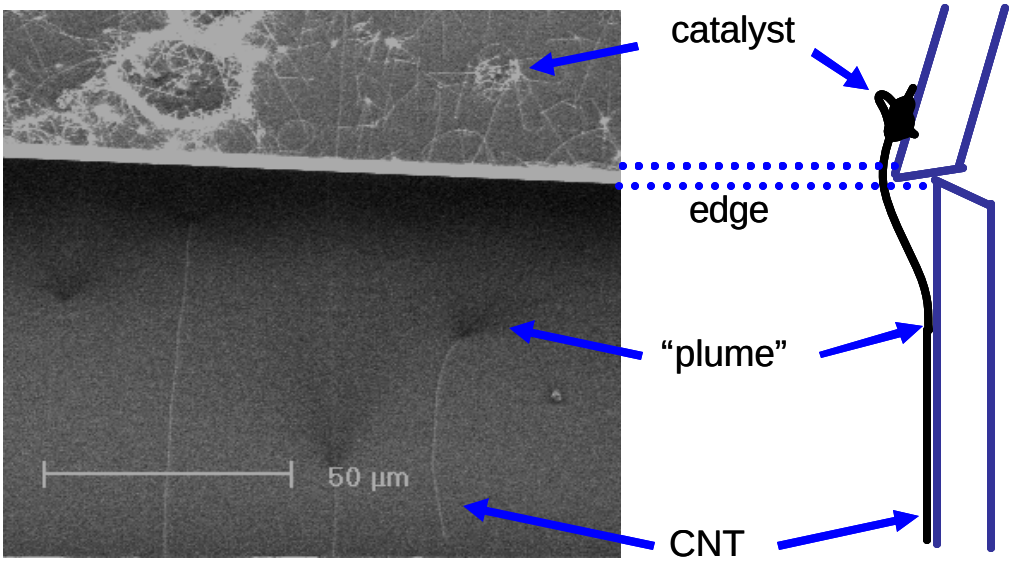

Figure 42. a) Scanning electron micrograph indicating three-dimensional nature of CNT growth: Gas flow during growth is from top to bottom. Upstream oxidized Si substrate rests on top of downstream one. CNTs change contrast upon contacting downstream substrate with a dark 'plume' upstream of point-of-contact, revealing CNT is above downstream substrate. b) Schematic illustrating side view of a).

Electrical transport measurements

We follow CNT growth with transport measurements. To prevent capacitive breakdown of the surrounding gas (which is enhanced due to the high electric field near the narrow diameter CNTs), electrical measurements are done in a vacuum, using a cryogenic probe station (1.5 K DesertCryo TT-Prober) on quartz substrates. After initial difficulties with capacitive breakdown of the dielectric substrate in the case of SiO_2 on Si substrates, single-crystal quartz substrates were used. Substrate breakdown may have been due to enhanced electric field at the substrate edge, or simply due to excess nanotubes which draped over the substrate edge causing shorts.

Figure 43 shows room temperature transport for differing gate heights at constant bias voltage for a suspended CNT. In the same geometry of Figure 41, source/drain voltage probes are applied to Pt electrodes underlying CNTs spanning the ~60 μm gap between substrates. A third probe is used as a wide-range (gate distance or thickness, t = 10μm-8), movable gate. This allows for a spatially varying gate coupling. Here, the gate probe is swept in a two-dimensional plane >100 μm above the plane of the CNT with voltages applied to both gate and drain electrodes. It is first positioned midway in the trench, then moved perpendicular to the CNT to maximize drain current I_d at 20 nA for a bias voltage V_d = 500mV and gate voltage V_g = -10V. The gate probe is then left stationary, and V_g is swept from -10 to 10V (dashed line). Leaving the gate probe fixed in its planar position, it is then lowered to <50μm separation from the CNT, and V_g was swept again (dotted line) with a noticeable change in threshold voltage (V_g at which I_d is minimum) and CNT response, giving a maximum drain current of 25 nA. Finally, the gate probe was lowered to <30 μm separation, with I_d vs. V_g now showing more response to the gate, minimal hysteresis and symmetric ambipolar conduction (solid line) without fully turning off. Such transport can be a qualitative indication of a small bandgap semiconducting CNT.[170] The non-hysteretic behavior over channel length ~ 40 μm reinforces the hypothesis that charge traps in the substrate contribute to hysteresis.

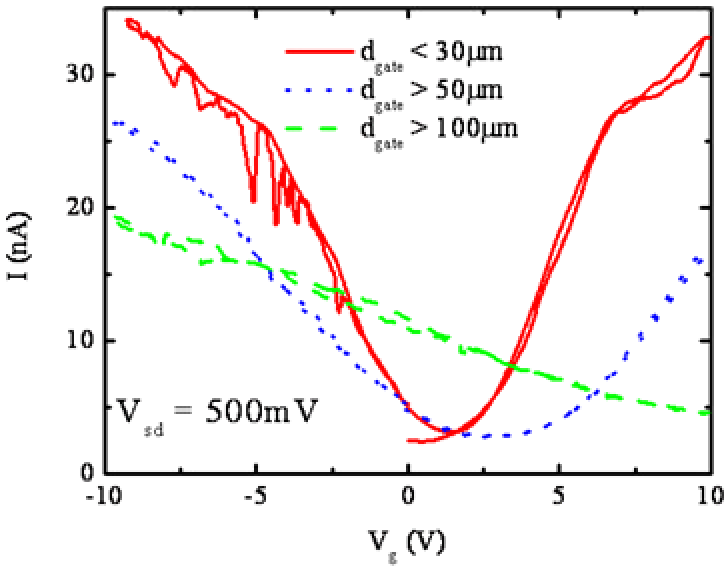

Figure 43. Drain current (I_d) vs. gate voltage (V_g) for different gate probe heights and constant bias voltage: In an evacuated probe station, electrical probes (tungsten with radius < 50μm) were applied to platinum source and drain electrodes. A third probe at -10 V, acting as a gate, was then swept in-plane above CNT in trench. After maximizing signal at V_g = -10V, V_g was swept to +10 V and back to -10 V. Different sweeps represent different approximate gate probe height above CNT. Sweeps display little to no hysteresis due to lack of substrate under long CNT.

We next investigate the temperature dependence of electrical transport in long, suspended CNTs with Pt electrodes. Figure 44 shows a series of constant-bias (V_{bias} = 2V) gate sweeps from room temperature to 1.5K. The drain current was highly non-linear in bias voltage, and large V_{bias} was required to establish a moderate drain current. The non-linearity and high resistance may arise from overcome high contact resistances (a problem for CNTs lying on top of electrodes) or another mechanism, such as space-charge limited current injection in the absence of significant capacitance to the gate near the electrodes. The gap-like structure of the non-linearity may suggest Coulomb blockade, but no evidence was seen for such in sweeps of the gate voltage. The I_d-V_g sweeps show little change in temperature until for T < 50K in Figure 44a). Figure 44b) plots the current minimum for each temperature in Figure 44a) on an Arrhenius plot and reveals two breaks in slope.

Evaluating the two regions 50 K < T < 150 K and T>150 K, we find activation energies E_{ac} = 5 and 15 meV. The origin of the small energy scale is not clear. E_{ac} may estimate the gap energy in a small band-gap semiconducting CNT[75] with the activated behavior arising from thermal activation of carriers over the bandgap. E_{ac} may also represent an effective Schottky barrier height (f_b) after the barrier width, x_m, has been thinned by V_{bias} to allow current to flow.

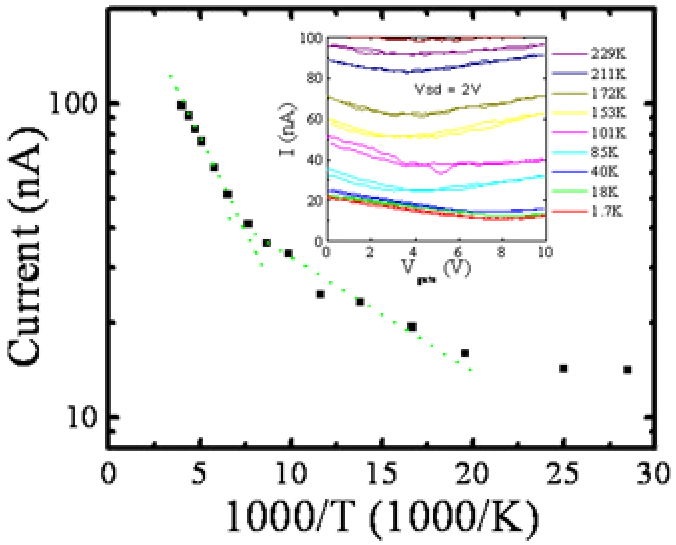

Figure 44. Arrhenius plot of drain current taken from current minima in the inset plot. Plot shows an activated behavior giving E_{ac} = 5 and 15meV for temperature ranges 50 K < T < 150 K, and T > 150 K respectively, with little change in current for temperatures < 30 K. Inset plot was generated following procedure outlined in text for Figure 43. Current plots vs. gate voltage were taken at a fixed position of the movable gate probe.

Tethered long, suspended carbon nanotubes

The same growth described here for long, suspended CNTs across trenches can be extended to the growth of long, suspended CNTs anchored by silica microspheres at each end. This allows the microspheres to act as anchors which may allow for the manipulation and investigation of CNTs using optical trapping methods. A schematic of such a geometry is shown in Figure 45. The microsphere anchors

provide the mechanical contact point while the CNT acts as a tether between the spheres. These can also adhere to a macroscopic substrate capable of withstanding human handling. They are also important for mechanical and soft-matter studies as the CNT can be coated with fluorescing molecules which then allow for a direct, dynamic evaluation of CNT behavior.

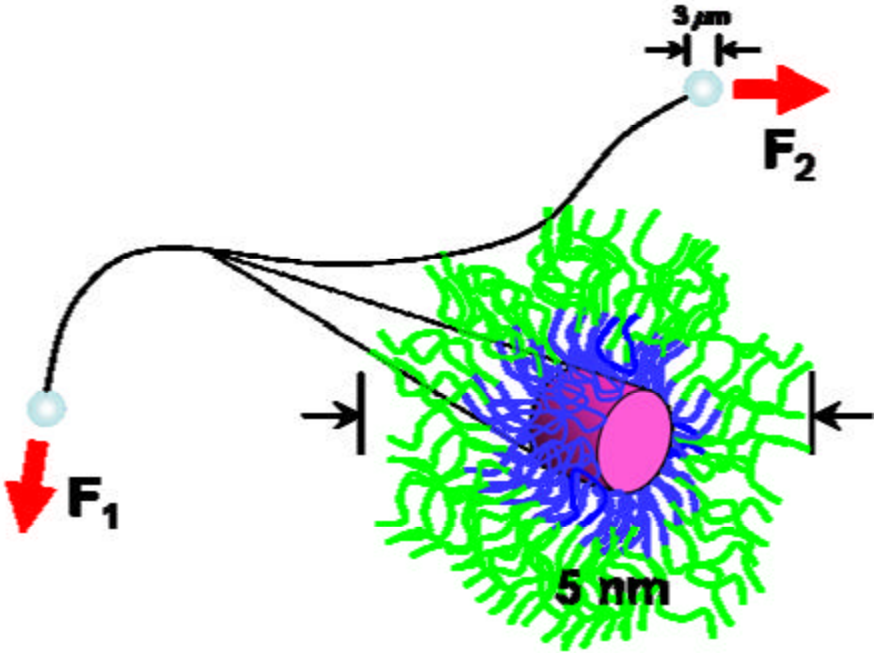

Figure 45. Schematic showing encapsulated carbon nanotubes (CNTs) attached to silica microspheres and suspended in solution. Blue-green strands represent fluorescing macromolecules wrapping the CNT, represented in zoom by the purple cylinder. The thin, black line depicts the long (length > 10 μm) CNT stretched between the blue silica microspheres. External forces acting on the beads are denoted F_1 and F_2 (courtesy of Erik Hobbie).

The manufacture of such CNT-microsphere devices follows closely from all the growth procedures described previously. Here, the microspheres are 'loaded' with catalyst particles before growth. This is accomplished by mixing of a microsphere containing solution with iron (III) nitrate in isopropyl alcohol, followed by a mixing with hexanes. This has the same result as the 'dipping' method of

Chapter 2: iron (III) nitrate preferentially precipitates onto the silica microspheres. TEM grids are then mechanically agitated in the catalyst-laden microsphere solution such that the microspheres adsorb to the surface of the copper grid. The TEM grids are then placed on a rigid substrate and inserted into the growth oven. Growth follows that described previously in this chapter.

An SEM image of the resulting structure is shown in Figure 46. The microscopheres act as microscopic substrates for the catalyst, and CNTs grow from these 'substrates.' As stated, these anchored CNTs can ostensibly be handled and manipulated utilizing conventional micromanipulators or SEM-based 'nanomanipulators.' The growth of CNTs in 'free space' is achieved with nominal alterations to the growth technique, but it has important implications for use of CNTs in electromechanical devices.

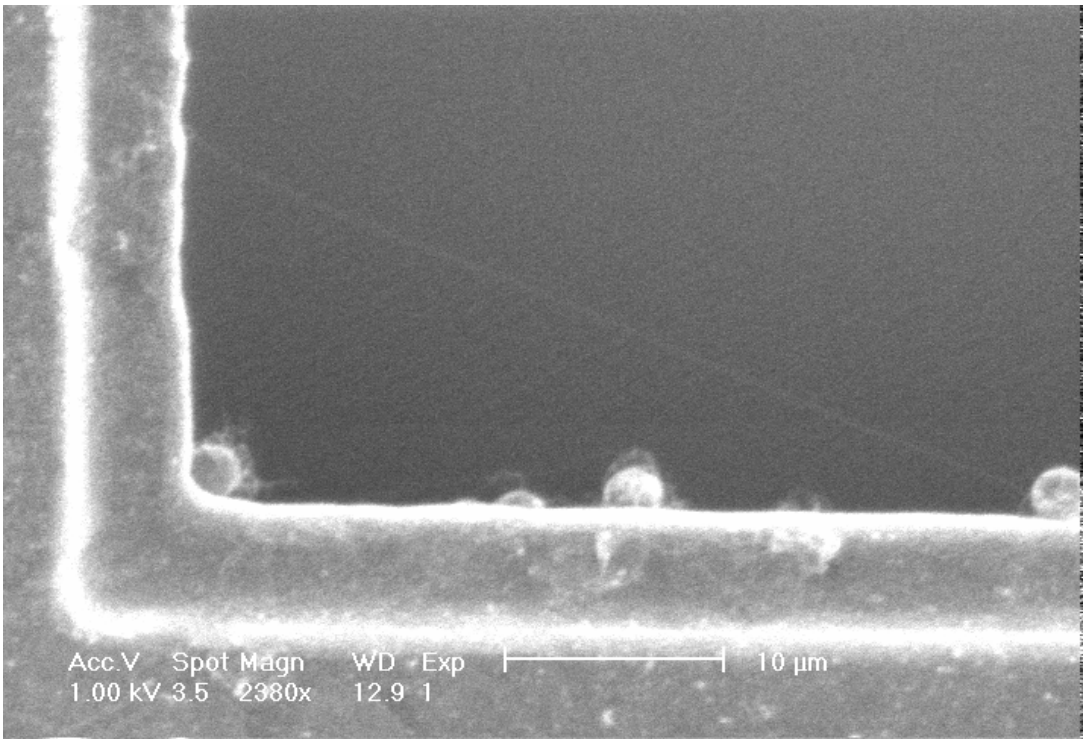

Figure 46. Carbon nanotubes growing from silica microscopheres. Following catalyst deposition, the microspheres are deposited onto a copper grid, here, a conventional transmission electron microscopy grid, visible at the left and bottom of the image. Following the typical growth procedure described in this chapter for flat substrates, CNTs can be imaged using a scanning electron microscope. The CNT can be seen originating from the microsphere at bottom right and crossing the empty portion of the TEM grid. A mass of shorter CNTs can be seen on the 3-4 microspheres in the middle of the micrograph.

We have here demonstrated the growth of individually addressable, long, suspended CNT devices without the use of etchants or resist. Scanning electron microscopy indicates the growth process to leave long suspended CNTs under tension between two individually mounted substrates. A wide-range, movable gate probe is used to study electrical transport in these devices. Measurements suggest that while the devices evidence poor contact resistances, perhaps due to large contact resistance, transport in suspended semiconducting nanotubes is highly ambipolar and symmetric,

and temperature scaling suggests a small-gap semiconducting carbon nanotube forms the channel in this field-effect geometry. We present this method to also demonstrate the robustness of CNTs to a growth process that includes adhesives joining three separate substrates. The growth process used to prepare suspended CNTs should leave the CNTs in a pristine state as no processing follows CNT growth, and should allow for measurement of CNT properties absent interference from substrate interactions and residual adsorbates.

Summary

Drawing together results from different experiments, it has been shown how carbon nanotubes behave in a uniquely 'nanoscopic' fashion. With diameters less than two nanometers, carbon nanotubes are still readily identifiable on insulating substrates in a scanning electron microscope. This is the result of the carbon nanotubes ability to move charge away from the charged portions of an insulating substrates. When carbon nanotube field effect transistors are manufactured on strontium titanate, one sees how a carbon nanotube can allow for a vertical narrowing of the Schottky barrier for exceptional device performance. In a device geometry with focused-electron-beam induced contacts, contact resistances approach the quantum of conductance which suggests that applications which are unacceptable (with resistivities that are orders of magnitude larger than bulk values for FEBID deposited metals) for macroscopic systems may prove viable for nanoscale ones. Lastly, the ability to grow self-supporting carbon nanotube structures with 10^5:1

aspect ratios is an exciting aspect of carbon nanotube research. Possibly more important, the minimal hysteresis shown in >20μm long, suspended CNT devices that are symmetrically ambipolar indicates that the intrinsic behavior of carbon nanotubes absent supporting substrates may yet be probed. Carbon nanotube devices may still display signs of scattering and charge traps dominating the electrical transport. Thus, the strive towards better carbon nanotube devices, improved performance, and more interesting physics continues.

Appendix A: **Lithography**

Lithography, as described in this dissertation, uses a beam of energetic particles to alter the properties of a material, called *resist*, which uniformly covers a flat substrate after a process called *spinning*. The path of the beam is controlled either by a computer following a pattern defined by a computer assisted design (CAD) program or through a physical *mask*. After *exposing* these defined regions in the resist, the substrates are put into a developer. In the case of a *positive* resist, the developer dissolves the exposed regions; for *negative* resist, the unexposed regions are dissolved. With positive resist, a material is then *deposited* into the exposed regions, whether by evaporation, casting or some process which leaves the desired material attached to the surface in the desired areas. This material adheres to the substrate and the remaining resist is dissolved in a solvent in a step referred to as *lift-off*, as the remaining deposited material on top of the resist is "lifted off" the substrate. This leaves the evaporated/cast material on the substrate only in the patterned regions exposed the by the electron beam.

Figure 47 shows the above steps as used in SWCNT device manufacture. In this dissertation, the focus is on electron beam lithography (EBL) followed by shorter descriptions of the process for optical lithography and shadow masking. Figure 47a shows the bare substrate, either single-crystal quartz or thermally grown silicon dioxide on top of degenerately-doped silicon. Figure 47b shows both resists after being sequentially spun onto the substrate at 4000 rpm for 45 sec, followed by a bake at 150°C for 5 min. For EBL resist, polymethyl methacrylate (PMMA) from

Microchem (www.microchem.com) is typically used. To increase the undercut, or slope of the resist sidewalls, a second resist, methyl acrylacetate methyl methacrylate (MAA9.5MMA) or co-PMMA, is used. This second resist is more sensitive to the electron beam and leaves an expanded exposed region beneath the top layer of PMMA, as seen in Figure 47b). This aids in lift-off as there is less resist near to the evaporated metals and is known as a bilayer resist. The spinning ensures uniformity of the resist thickness, and the baking hardens the resist. For optical resist, I use 'Shipley' S1813 which is spun at 3000rpm for 45 seconds and baked at 115°C for 60 seconds.

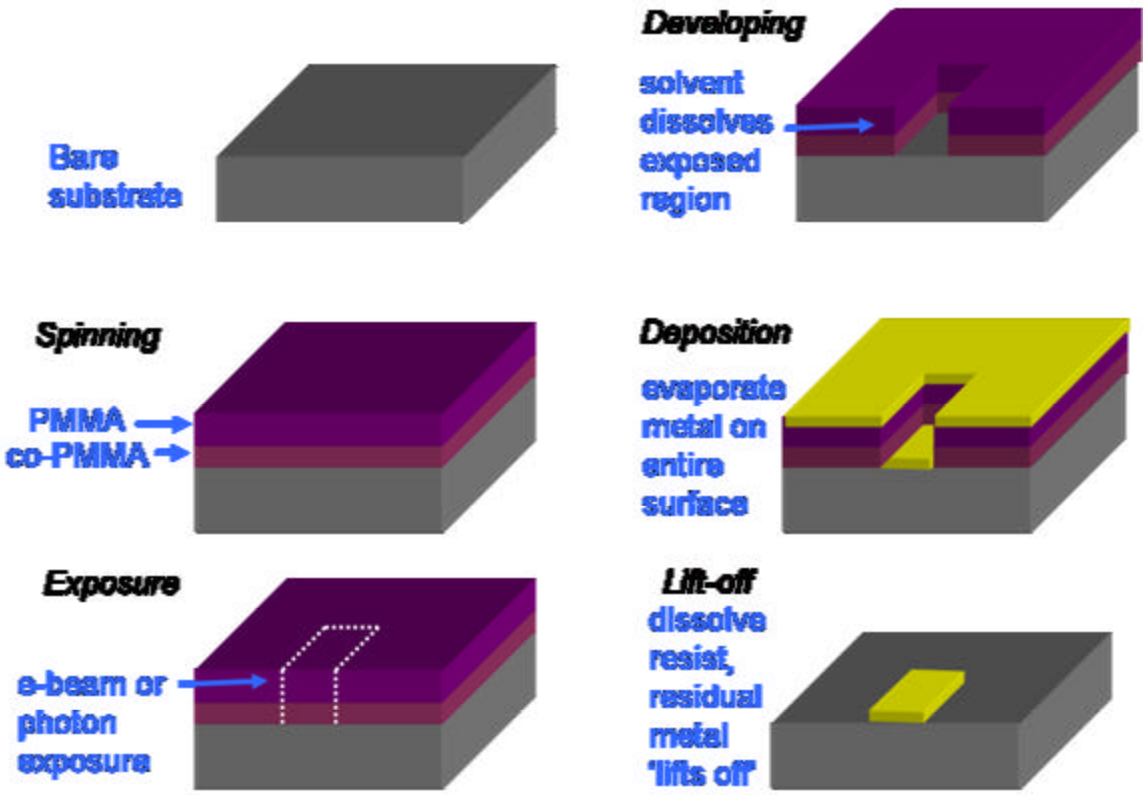

Figure 47. Schematic of steps required in typical electron beam lithography: The substrate is first covered with one or more (two in this case) resists which are sensitive to exposure by an electron beam. After exposing the resist to a user-defined pattern, the sample is immersed in a solvent which dissolve the electron-beam-exposed resist. After development, metal can be thermally evaporated on top of the exposed resist. Lastly, the entire sample is placed in a solvent which dissolves the remaining resist while leaving the metal adhered to the substrate.

The resist-covered substrate is then place in a scanning electron microscope (SEM) for electron beam *exposure*. Herein, both a JEOL 5400 and an XL30 are used for EBL. The substrate is then exposed using a DesignCAD software together with the nanopattern generation system (NPGS) which controls the beam during patterning, or writing. The exposure doses, given in $\mu C/cm^2$, are optimized for the particular resist and microscope, Microchem 950C2 and a Philips XL30 in this case. A JEOL5400 SEM was also used for some of the earlier work. Regardless of the microscope, doses are typically ~200$\mu C/cm^2$, with optimization only being necessary for the narrowest lines. The exposure using optical lithography is typically at a power 300W/cm^2 for 12 seconds.

After exposure, the samples are placed into a developer which causes the exposed regions of resist to dissolve. With this PMMA, I use methyl isobutyl ketone (MIBK) which has been pre-diluted (1:3 by volume) with isopropyl alcohol (IPA), also from Microchem. The developing time depends on the dose as well as the area of the exposed region. It must also be optimized for the narrowest lines and for radically different exposure areas. The change in rate with exposure area, in turn, happens due to slightly different doses for different beam size and magnification as well as nonuniformities in the spun resist. For the optical resist, a resist-specific developer is used.

Following developing, a deposition step is performed in which a material is placed in the exposed and developed regions of the pattern. This is typically a metal which is thermally evaporated in a vacuum chamber. Thermal evaporation here means that substances are placed in a boat (typically tungsten) which is heated

through Joule heating until the vapor pressure of the metal to be evaporated becomes high enough to produce the desired rate of deposition on the substrate. This results in metal coating the surface of the resist-covered substrate; the line-of-sight from the evaporation source to the substrate determines how the metal deposits on the resist. Thermal evaporation was used in this thesis to prepare electrodes of chromium and gold; typically consisting of 2-3nm of chromium, which acts as an adhesion layer, followed by 20-70nm of gold. The adhesion layer is necessary because gold does not adhere well to silicon dioxide, the most common substrate in my experiments.

For platinum, palladium, and tungsten, electron-beam evaporation was used. This technique again relies on heating the material to be deposited to achieve a significant vapor pressure, but it employs a directed beam of electrons to achieve local heating of the deposition material as opposed to Joule heating over the entire sample. This technique allows for a more controlled deposition of metals that have low vapor pressures. This evaporation technique is used for platinum and palladium electrodes, as well as tungsten as an adhesion layer.

After depositing metals, the last step is lift-off in which the resist is removed along with the metal which lies on top of resist in the undeveloped regions. This is done by placing the substrate, resist and evaporated metal included, into a solvent which dissolves the resist. At this point the evaporated metal on top of the resist is 'floating' on top of the dissolved, liquid resist. All the resist and solid metal on top of it is then washed away in a rinse, typically with the same solvent used to dissolve the resist. In some cases, the superfluous metal (that is not intended to remain on the substrate) adheres to the surface despite the intervening layer of dissolved resist. In

this case, it sometimes becomes necessary to briefly ultrasonicate the substrate to detach these unwanted metals from the surface.

All the steps above focus on the general procedure for EBL with passing references to optical lithography. Briefly, the fundamental difference between the methods is the exciting particles and resist: photons vs. energetic accelerated electrons and optical resist vs. PMMA. The materials have different properties and are handled differently, but the technique remains the same. In addition to the different resists for each method, one of the most important practical differences between EBL and optical lithography is that EBL is serial and optical is parallel. Thus, optical lithography can pattern entire wafers in one step, in ambient conditions. EBL requires an SEM which must be evacuated before the electron beam is serially scanned over the desired pattern; the time to create the pattern scales roughly linear with the area to be patterned. The big advantage to EBL, however, is its reduced feature size compared to optical lithography. Typical optical lithography patterns do no better than 1μm feature size with the state-of-the-art producing ~100nm features through expensive, multi-layer and multi-exposure lithography; however, with an inexpensive SEM, designers can rely on EBL producing minimum feature sizes <50nm, and with specialized resists and specialized high-energy electron-beam lithography tools, feature sizes can be significantly smaller than 10 nm. Another advantage to EBL is its versatility to new types of designs: EBL only requires changes to the CAD program controlling the electron beam. With optical lithography, a new physical mask must be made to pattern the resist.

Yet another type of lithography is shown in Figure 48. This is referred to as shadow or stencil masking. Unlike the previously described techniques in which the resist adheres to the surface, this uses a rigid stencil mask to leave the desired pattern. This avoids the use of spinning resist on the sample. The material is simply evaporated through the holes in the mask, leaving metal in the desired positions on the substrate. There are several drawbacks however. There are less well-defined, larger features due to diffusion around a mask which is not in contact with the substrate. The smallest mask openings can slowly 'clog' with metals adhering to the edge of the mask, and alignment becomes difficult with mechanical alignment between the mask and substrate becoming necessary. Stencil masking also requires that new physical masks must be made each time the pattern is altered, as with optical lithography. Still, shadow masking is a straightforward method of lithography that avoids the use of resists, and it can be used in some processes where 'conventional' lithography is not possible.

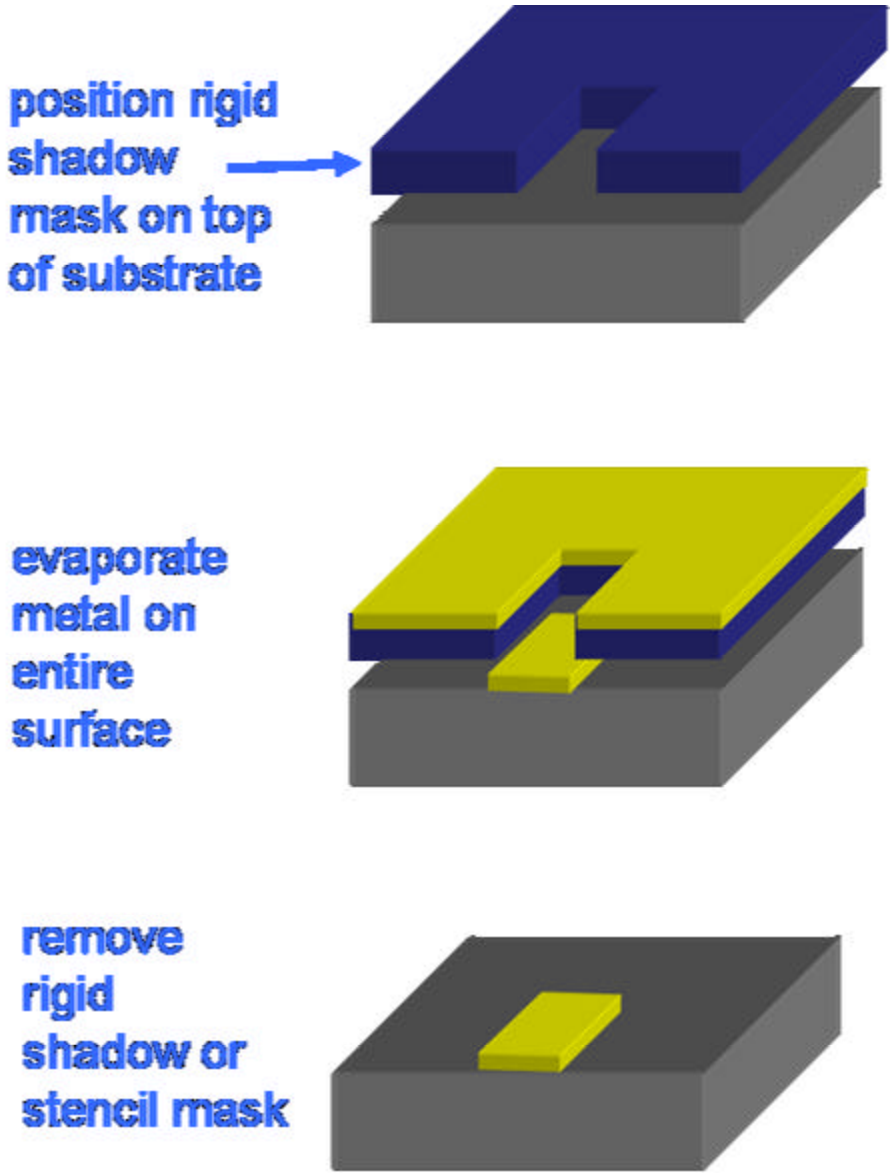

Figure 48. Steps outlining use of a stencil mask for lithography. While no resist is used and the term lithography may not be entirely applicable, the results are the same: materials deposited on a given substrate in defined locations.

Masks are created through a variety of techniques in a variety of materials. The conventional EBL steps described above can be employed to define regions on a metallic mask substrate which are later etched away, or the stencil masks can also be 'cut' using a high powered laser. In EBL processing, feature sizes are limited by the thickness of the material and etch processing. In laser cutting, the minimum hole

width and separation of such masks are limited by the laser resolution, nominally >10μm. These techniques both have the advantage of being entirely flexible to any type of layout. These custom-made masks require user expertise, production time, and financial outlays however.

Another possibility which allows for less flexibility, but which is substantially easier and cheaper, is the use of transmission electron microscopy (TEM) grids as shadow masks. The technique does not fundamentally differ from the techniques described above in procedure; 'off-the-shelf' TEM grids are ostensibly the same as user defined and manufactured metal stencil masks. A TEM grid stencil was used to produce the array of rectangular gold electrodes on quartz for CNT devices in Chapter 2. In practice however, the standardization of processing and quality control by commercial providers allows for a substantial reduction in development time for the researcher. Again, the drawback is in the fixed geometry of available TEM grids.

Appendix B: **Scanning Probe Microscopy and Electrostatic Force Microscopy Technique**

As mentioned in Chapter 2 and as seen in Chapter 5, scanning probe microscopy is a useful tool for studying nanoscopic systems. Continuing from the brief introduction in Chapter 2, this Appendix is intended to describe the details of scanning probe microscopy to an extent not possible within an expository section of the dissertation.

The cantilever/tip's interaction with the surface and the feedback used to monitor this interaction make up the entirety of what is practically known as SPM. We shall focus here on the use of oscillating cantilevers for "TappingMode™", "intermittent-contact", and "ac mode" scanning of surface for CNT devices. One can also drag the cantilever across the sample and use feedback to keep the cantilever focused on the middle of the photodiode, called "contact" mode, but this is more invasive and more difficult to quantify due to lateral forces and losses. With CNT imaging in particular, "contact" mode has the ability to move CNTs across the surface. This has been shown to be useful, but the complexity of the process and unknown damage to the CNT has led to little recent research on the technique.

Atomic force microscopy using ac mode with an oscillating cantilever has the advantage of little lateral interaction as the tip repeatedly strikes normal to sample surface. Also, there is the added benefit of a phase value which can give useful qualitative information and is particularly useful in identifying changes in the surface which are not detected in topography. A diagram is shown in Figure 49. This

provides the basis for most other scanning probe techniques as topography must always be accounted for.

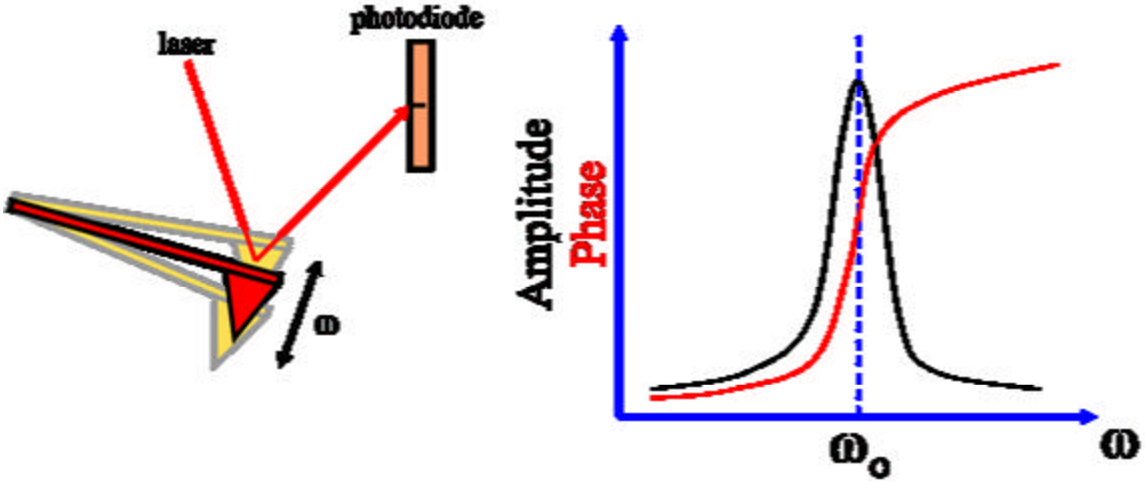

Figure 49. Atomic force microscopy (AFM): Reflecting cantilever oscillates at resonant frequency which is detected at photodiode. A plot of amplitude and phase for a given frequency is the starting point for all studies of AFM.

This detection method does not require conducting samples, and thus is more widely applicable. In this work, the AFM imaging used is called alternatively "TappingMode™", "intermittent-contact", and "ac mode". This mode utilizes a cantilever which is excited at a frequency slightly lower than its resonant frequency, such that when it is brought into contact with the surface and feels the repulsive tip-surface potential, the resonance frequency increases, and the amplitude decreases. The piezos then act to move the sample and cantilever apart until a previously defined setpoint is reached. In cases of depressions on the surface, the total amplitude increases and the piezo tube acts to bring the sample and cantilever closer together. The topography of a surface is then given by the voltage (which then corresponds to a distance) on the piezo tube for each point in the 2-dimensional region being scanned.

Using this topography scan, the piezos can be controlled such that the tip remains at a set distance above the surface: the “lift” scan described in Chapter 2, Figure 50. This then allows for non-contact measurements. I will focus here on electrostatic force microscopy, especially the method used to subtract the background signals such that an accurate value can be obtained for the potential at a given point on the surface.

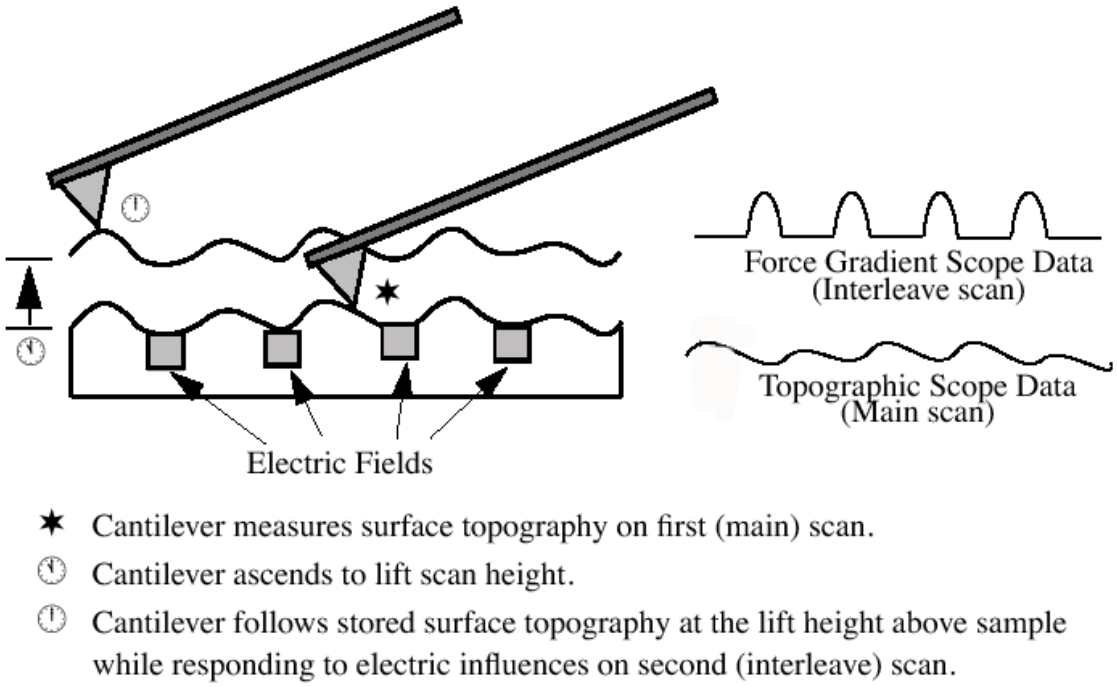

Figure 50. Schematic describing the "lift" scan which enables electrostatic force microscopy (EFM): In a separate "interleave" scan following a conventional topography scan, the cantilever traces out the topography of the previous scan at a fixed above the sample surface. Image courtesy of Digital Instruments Veeco Metrology group.

Figure 51 shows the microscope used to do most of the scanning probe microscopy presented here. The stage along with the micropositioners allows for electrical probing of surfaces while on the stage of the microscope. This enables

electrostatic force microscopy as described in Chapter 2. I will briefly describe here how the electrostatic force microscopy data was acquired.

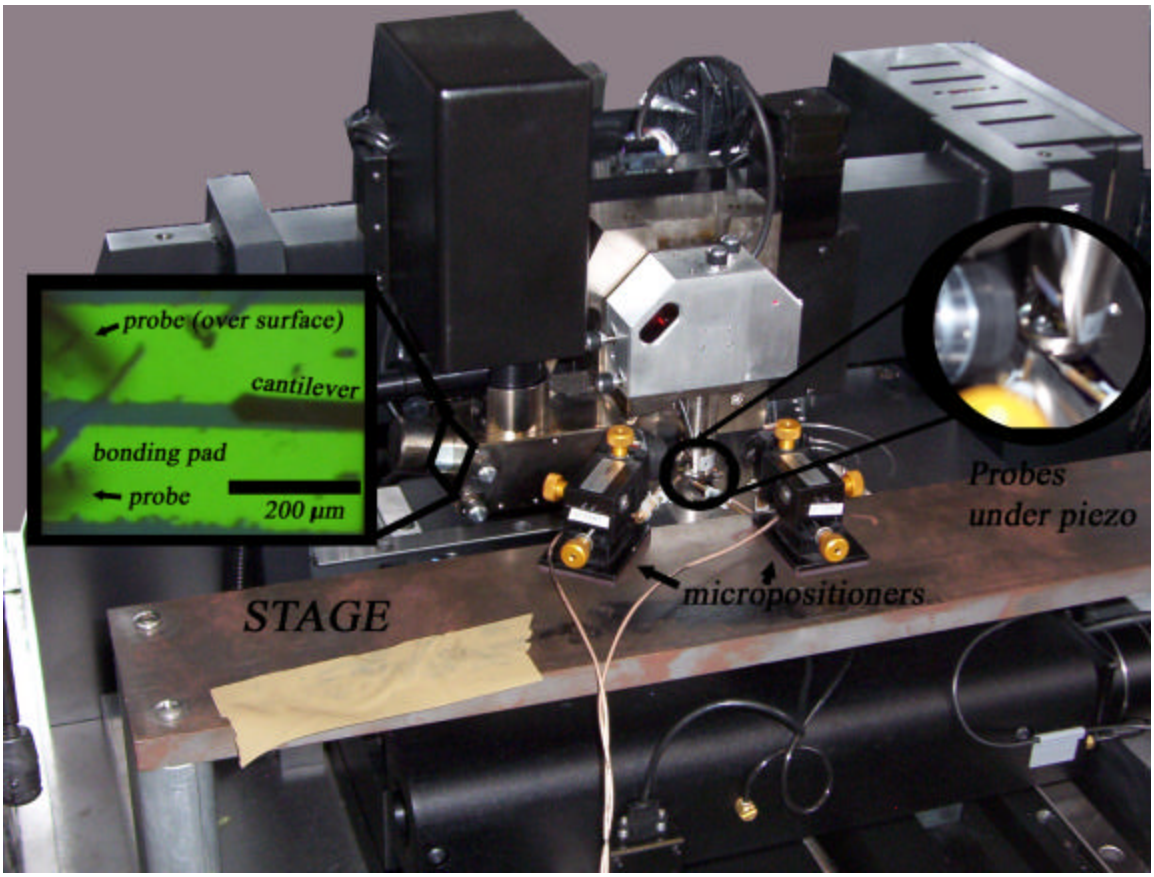

Figure 51. Photograph of Digital Instruments D5000 scanning probe microscope with stage for electrical probing. The micropositioners on the stage allow for the placement of electrical probes on the surface of the sample. A zoomed view of the probes underneath the piezo tubes is shown in the inset to the right. The inset on the left shows an image as seen through the optical system. This image is normal to the surface and is used to place the probes at a given position as well as for finding a given location on the sample surface. The cantilever is visible on the right of the inset, while the shadows from the probes are visible on the left. The large gold pads at the top and bottom are used to make electrical contact to the sample.

As described in Chapter 2, EFM is done utilizing the 'lift mode' of the microscope while biasing the sample at a small voltage at the cantilever's resonant frequency. An example of EFM vs. AFM is given in Figure 52. The left portion is a topography image showing a ~20nm gold electrode at the top of the scan area. A nanotube is visible as it extends up to, and underneath the electrode. An averaged

line scan shows the CNT height to be <1nm. The right of the image is the EFM image with the CNT biased at 400mV while the top electrode is grounded. One sees a large response to the electrostatic potential over the CNT while there is little response at the electrode. This indicates that the entirety of the potential is dropping at the electrode. This is an example of extremely poor contact resistance.

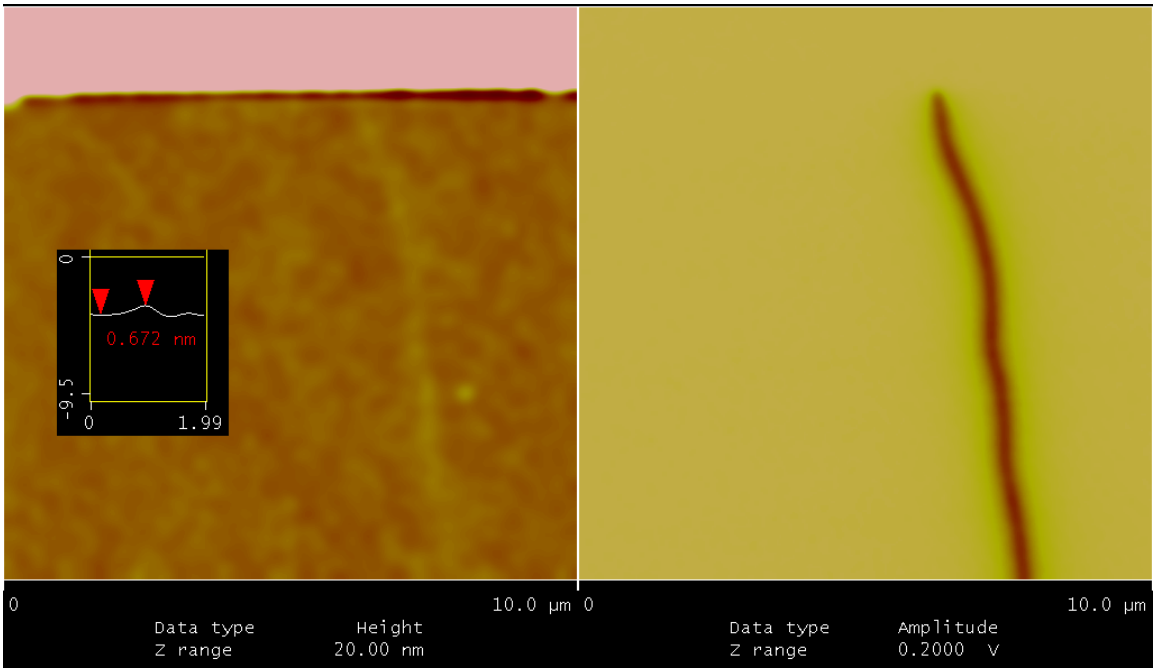

Figure 52. Carbon nanotube device: topography and electrostatic potential graph. The left image displays a carbon nanotube (in the middle of the image) and an electrode (bright region at top). An inset gives the nanotube height as determined by an average height along its length. The right image is the electrostatic potential as determined by electrostatic force microscopy. The CNT appears dark because it is biased at 400mV by an electrode outside the field of view. The top electrode is grounded. This shows that all the resistance in the CNT device is at the contact to the top electrode because this is where all the potential drop happens.

For cases in which the contact resistance is not so readily evident, I do several steps to ensure that I have subtracted any background signals due to the cantilever capacitively coupling to the electrodes. The first step is ensuring that the cantilever is responding linearly to the electrostatic potential, such that:

$$A \sim F(w) \sim (V_{DC} + \Delta\Phi)V_{AC}(w)$$

holds true. This is achieved in a series of scans over the same portion of the sample as the ac bias is varied. Not shown here, the amplitude of the cantilever has a linear dependence on the ac bias voltage.

The next step is to bias the entire sample to see what the capacitive coupling to the electrodes produces. An example of this is given in Figure 53. This is another image of the sample shown in Chapter 5. Here, the electrodes at the top left and bottom of the image are being biased at 400mV. The line scans depicted in the image are shown as traces in the graph in the top of the figure. These values give the cantilever response for a 400mV bias on the sample. This step is important to ensure that the increased coupling to the electrodes is not mistakenly understood as higher field. This is seen in the line scans in which the photodetector voltage is significantly higher over the electrodes than over the CNT. This is due to the increased capacitive coupling to the large electrodes. The photodetector voltage, A_{400mV}, over the CNT gives shows the response of the cantilever when it is over a region of the CNT that is at 400mV.

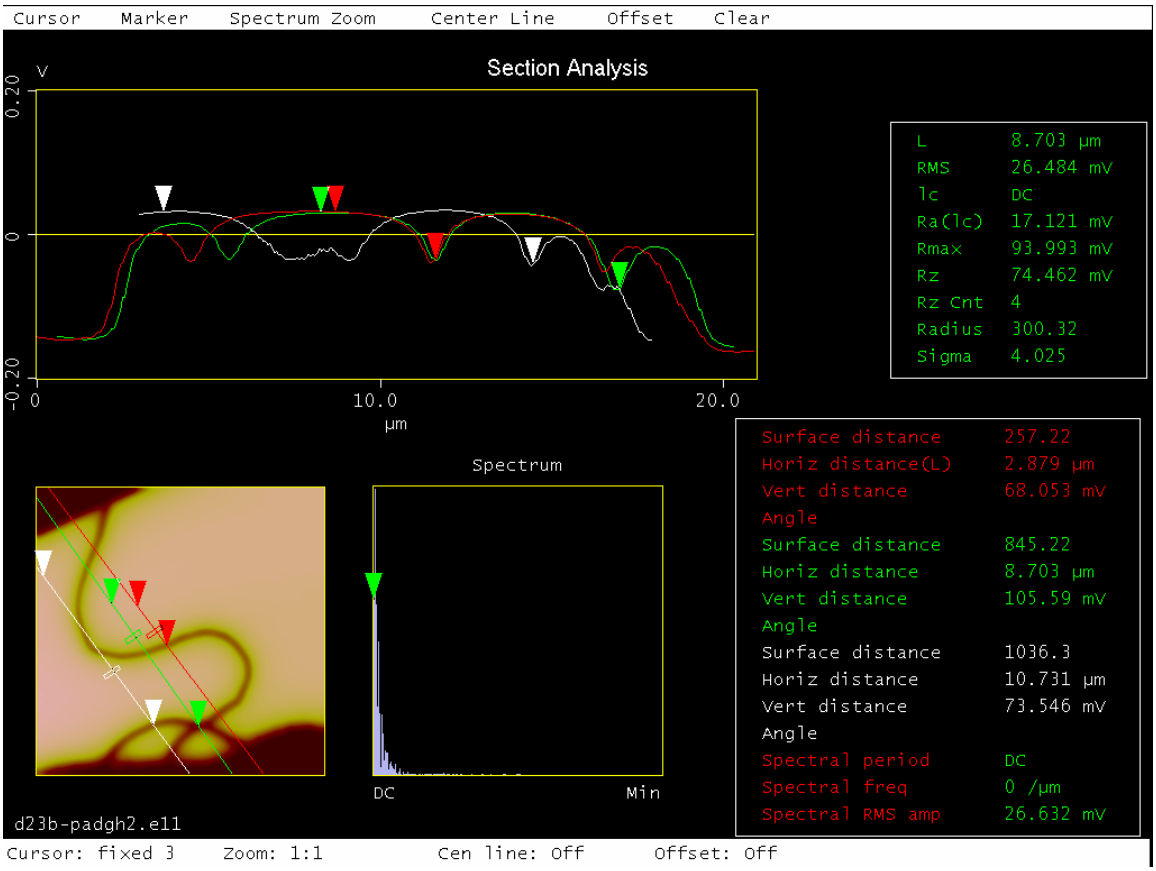

Figure 53. Electrostatic force microscopy image while both electrodes are biased at 400mV: The line scans visible in the image are shown on a plot above. These demonstrate how the photodetector response is greater over the electrodes than over the CNT. This image also provides a value for the response of the cantilever at 400mV.

To obtain the potential at each given point on the CNT while one electrode is biased and the other grounded, the zero for the cantilever response is taken at a distance far from the electrodes. Figure 54 gives an example of several of these slices. The response of the electrode as the cantilever is positioned over the CNT can be used to plot the potential of the CNT at that point, using $V(x,y) = V_{bias}(A(x,y)/A_{bias})$. These values can then be plotted along the length of the tube to give a graph such as Figure 40.

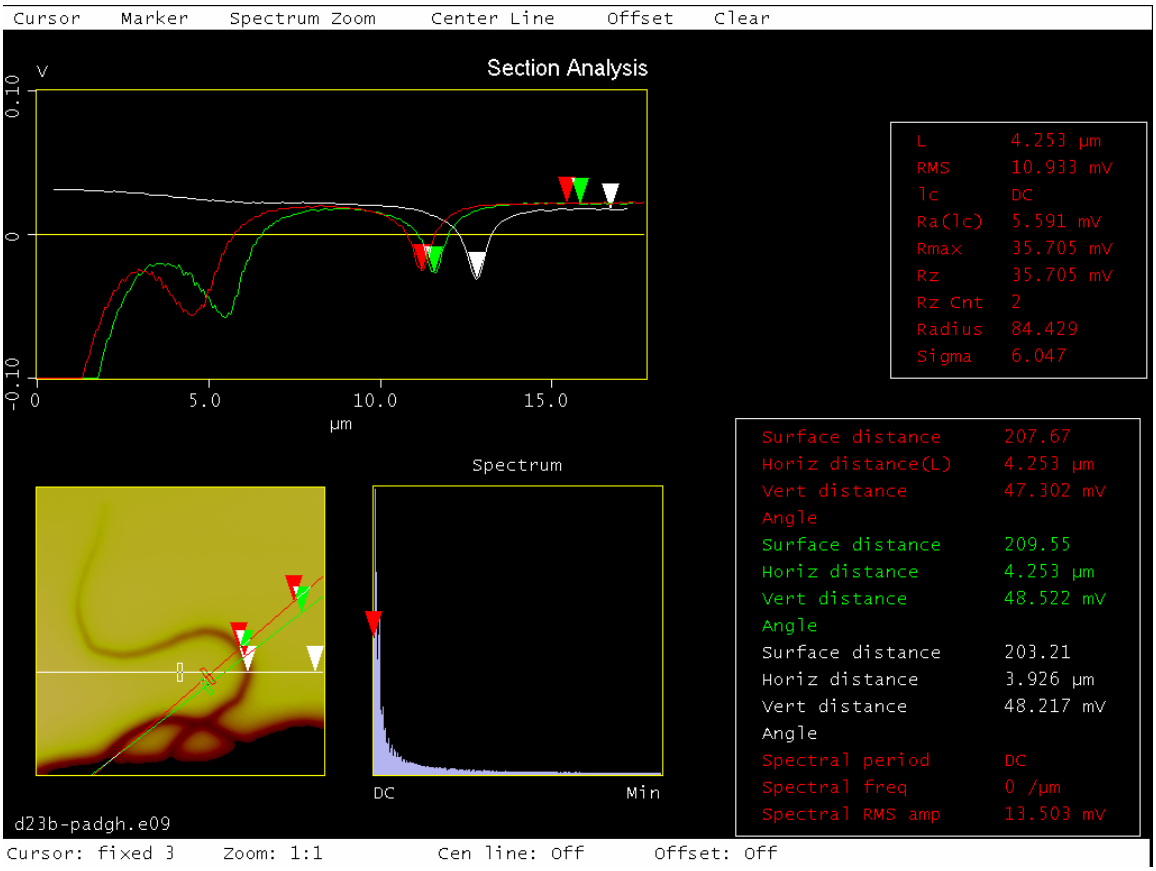

Figure 54. Electrostatic force microscopy image while one electrode is biased while the other is grounded. The drop along the CNT visible in the image is given quantitatively in the line scans visible in the plot above. These values can then be plotted vs. position along the CNT to give potential plots such as that found in Figure 40.

Bibliography

1. M.S. Dresselhaus, G. Dresselhaus, and P.C. Eklund, *Science of fullerenes and carbon nanotubes*. (Academic Press, San Diego, 1996), pp.xviii.
2. R.E. Smalley, Great Balls of Carbon - the Story of Buckminsterfullerene, Sci.-New York **31**, 22 (1991).
3. M. Endo, K. Takeuchi, S. Igarashi, K. Kobori, M. Shiraishi, and H.W. Kroto, The production and structure of pyrolytic carbon nanotubes (PCNTs), J. Phys. Chem. Solids (UK) **54**, 1841 (1993).
4. S. Iijima, Growth of Carbon Nanotubes, Mat Sci Eng B-Solid **19**, 172 (1993).
5. S. Iijima, Helical microtubules of graphitic carbon, Nature **354**, 56 (1991).
6. J.W. Mintmire, B.I. Dunlap, and C.T. White, Are fullerene tubules metallic?, Physical Review Letters **68**, 631 (1992).
7. R. Saito, M. Fujita, G. Dresselhaus, and M.S. Dresselhaus, Electronic structure of chiral graphene tubules, Applied Physics Letters **60**, 2204 (1992).
8. N. Hamada, S. Sawada, and A. Oshiyama, New one-dimensional conductors: graphitic microtubules, Physical Review Letters **68**, 1579 (1992).
9. A. Oberlin, M. Endo, and T. Koyama, High-Resolution Electron-Microscope Observations of Graphitized Carbon-Fibers, Carbon **14**, 133 (1976).
10. A. Oberlin, M. Endo, and T. Koyama, Filamentous Growth of Carbon through Benzene Decomposition, Journal of Crystal Growth **32**, 335 (1976).
11. M. Endo, A. Oberlin, and T. Koyama, High-Resolution Electron-Microscopy of Graphitizable Carbon-Fiber Prepared by Benzene Decomposition, Japanese Journal of Applied Physics **16**, 1519 (1977).
12. P.R. Wallace, The Band Theory of Graphite, Phys Rev **71**, 476 (1947).
13. R. Saito, M. Fujita, G. Dresselhaus, and M.S. Dresselhaus, Electronic structure of graphene tubules based on C/sub 60/, Phys. Rev. B, Condens. Matter (USA) **46**, 1804 (1992).
14. S. Datta, *Electronic transport in mesoscopic systems*. (Cambridge University Press, Cambridge ; New York, 1995), pp.xv.
15. Y. Imry, *Introduction to mesoscopic physics*, 2nd ed. (Oxford University Press, Oxford ; New York, 2002), pp.xiii.
16. A.M. Fennimore, T.D. Yuzvinsky, W.-Q. Han, M.S. Fuhrer, J. Cumings, and A. Zettl, Rotational actuators based on carbon nanotubes, Nature **424**, 408 (2003).
17. M.F. Yu, O. Lourie, M.J. Dyer, K. Moloni, T.F. Kelly, and R.S. Ruoff, Strength and breaking mechanism of multiwalled carbon nanotubes under tensile load, Science **287**, 637 (2000).
18. M.F. Yu, B.S. Files, S. Arepalli, and R.S. Ruoff, Tensile loading of ropes of single wall carbon nanotubes and their mechanical properties, Physical Review Letters **84**, 5552 (2000).
19. E.W. Wong, P.E. Sheehan, and C.M. Lieber, Nanobeam mechanics: elasticity, strength and toughness of nanorods and nanotubes, Science **277**, 1971 (1997).

20. D.A. Walters, L.M. Ericson, M.J. Casavant, J. Liu, D.T. Colbert, K.A. Smith, and R.E. Smalley, Elastic strain of freely suspended single-wall carbon nanotube ropes, Applied Physics Letters **74**, 3803 (1999).
21. M.M.J. Treacy, T.W. Ebbesen, and J.M. Gibson, Exceptionally high Young's modulus observed for individual carbon nanotubes, Nature **381**, 678 (1996).
22. B.I. YakobsonandP. Avouris, in *Topics in Applied Physics*, edited by M. S. Dresselhaus, G. Dresselhaus, and Ph. Avouris (Springer, Berlin, 2001), Vol. 80, pp. 287.
23. M.-F. Yu, O. Lourie, M.J. Dyer, K. Moloni, T.F. Kelly, and R.S. Ruoff, Strength and Breaking Mechanism of Multiwalled Carbon Nanotubes Under Tensile Load, Science **287**, 637 (2000).
24. Y. Xia, M. Zhao, Y. Ma, M. Ying, X. Liu, P. Liu, and L. Mei, Tensile strength of single-walled carbon nanotubes with defects under hydrostatic pressure, Physical Review B (Condensed Matter and Materials Physics) **65**, 155415 (2002).
25. F. Li, H.M. Cheng, S. Bai, G. Su, and M.S. Dresselhaus, Tensile strength of single-walled carbon nanotubes directly measured from their macroscopic ropes, Applied Physics Letters **77**, 3161 (2000).
26. R.L. Jaffe and B. Jarvis, Models of carbon nanotube reactivity., Abstr Pap Am Chem S **221**, U591 (2001).
27. J. Hone, M.C. Llaguno, M.J. Biercuk, A.T. Johnson, B. Batlogg, Z. Benes, and J.E. Fischer, Thermal properties of carbon nanotubes and nanotube-based materials, Applied Physics a-Materials Science & Processing **74**, 339 (2002).
28. J. Hone, in *Carbon Nanotubes* (2001), Vol. 80, pp. 273.
29. M. Fujii, X. Zhang, H.Q. Xie, H. Ago, K. Takahashi, T. Ikuta, H. Abe, and T. Shimizu, Measuring the thermal conductivity of a single carbon nanotube, Physical Review Letters **95**, 065502 (2005).
30. E. Brown, L. Hao, J.C. Gallop, and J.C. Macfarlane, Ballistic thermal and electrical conductance measurements on individual multiwall carbon nanotubes, Applied Physics Letters **87**, 023107 (2005).
31. T.Y. Choi, D. Poulikakos, J. Tharian, and U. Sennhauser, Measurement of thermal conductivity of individual multiwalled carbon nanotubes by the 3-omega method, Applied Physics Letters **87**, 013108 (2005).
32. I. Palaci, S. Fedrigo, H. Brune, C. Klinke, M. Chen, and E. Riedo, Radial elasticity of multiwalled carbon nanotubes, Physical Review Letters **94** 175502 (2005).
33. X.W. Wang, Z.R. Zhong, and J. Xu, Noncontact thermal characterization of multiwall carbon nanotubes, Journal of Applied Physics **97**, 064302 (2005).
34. T. Yamamoto, S. Watanabe, and K. Watanabe, Low-temperature thermal conductance of carbon nanotubes, Thin Solid Films **464-65**, 350 (2004).
35. S. Berber, Y.K. Kwon, and D. Tomanek, Unusually high thermal conductivity of carbon nanotubes, Physical Review Letters **84**, 4613 (2000).
36. Y.K. Kwon, S. Berber, and D. Tomanek, Thermal contraction of carbon fullerenes and nanotubes, Physical Review Letters **92**, 015901 (2004).
37. J.W. Che, T. Cagin, and W.A. Goddard, Thermal conductivity of carbon nanotubes, Nanotechnology **11**, 65 (2000).

38. J.W. Che, T. Cagin, W.Q. Deng, and W.A. Goddard, Thermal conductivity of diamond and related materials from molecular dynamics simulations, J. Chem. Phys. **113**, 6888 (2000).
39. T. Brintlinger, Y.F. Chen, T. Dürkop, E. Cobas, M.S. Fuhrer, J.D. Barry, and J. Melngailis, Rapid imaging of nanotubes on insulating substrates, Applied Physics Letters **81**, 2454 (2002).
40. T. Durkop, B.M. Kim, and M.S. Fuhrer, Properties and applications of high-mobility semiconducting nanotubes, Journal of Physics-Condensed Matter **16**, R553 (2004).
41. T. Dürkop, T. Brintlinger, and M.S. Fuhrer, presented at the XV International Winterschool/Euroconference, Kirchberg, Tirol, Austria, 2002 (unpublished).
42. T. Dürkop, T. Brintlinger, and M.S. Fuhrer., in *Structural and Electronic Properties of Molecular Nanostructures*, edited by H. Kuzmany, J. Fink, M. Mehring et al. (AIP Conference Proceedings, New York, 2002), pp. 242.
43. M.S. Fuhrer, B.M. Kim, T. Dürkop, and T. Brintlinger, High-mobility nanotube transistor memory, Nano Letters **2**, 755 (2002).
44. B.M. Kim, T. Brintlinger, E. Cobas, M.S. Fuhrer, H.M. Zheng, Z. Yu, R. Droopad, J. Ramdani, and K. Eisenbeiser, High-performance carbon nanotube transistors on SrTiO3/Si substrates, Applied Physics Letters **84**, 1946 (2004).
45. T. Brintlinger, J. Melngailis, M.S. Fuhrer, I. Utke, T. Bret, A. Perentes, P. Hoffmann, M. Abourida, and P. Doppelt, Electrodes for Carbon Nanotube Devices by Focused-Electron-Beam Induced Deposition of Pure Gold, to appear in Journal of Vacuum Science and Technology B Vol. 23 (2005).
46. J. Appenzeller, J. Knoch, V. Derycke, R. Martel, S. Wind, and P. Avouris, Field-modulated carrier transport in carbon nanotube transistors, Physical Review Letters **89**, 126801 (2002).
47. T. Brintlinger, B.M. Kim, E. Cobas, and M.S. Fuhrer, presented at the Electronic Properties of Synthetic Nanostructures, Kirchberg, Austria, 2004.
48. T. Dürkop, Ph. D. dissertation, University of Maryland, College Park, 2004.
49. H.W. Kroto, J.R. Heath, S.C. O'Brien, R.F. Curl, and R.E. Smalley, Nature **318**, 162 (1985).
50. W. Kratschmer, L.D. Lamb, K. Fostiropoulos, and D.R. Huffman, Solid C-60 - a New Form of Carbon, Nature **347**, 354 (1990).
51. Q.M. Gong, L. Zhi, X.D. Bai, D. Li, and J. Liang, The effect of carbon nanotubes on the microstructure and morphology of pyrolytic carbon matrices of C-C composites obtained by CVI, Compos. Sci. Technol. **65**, 1112 (2005).
52. H.O. Pierson and M.L. Lieberman, Chemical Vapor-Deposition of Carbon on Carbon-Fibers, Carbon **13**, 159 (1975).
53. W. Kratschmer, K. Fostiropoulos, and D.R. Huffman, Chem. Phys. Lett. **170**, 167 (1990).
54. D.T. Colbert, J. Zhang, S.M. McClure, P. Nikolaev, Z. Chen, J.H. Hafner, D.W. Owens, P.G. Kotula, C.B. Carter, J.H. Weaver, A.G. Rinzler, and R.E. Smalley, Growth and sintering of fullerene nanotubes, Science **266**, 1218 (1994).

55. D.S. Bethune, C.H. Klang, M.S. de Vries, G. Gorman, R. Savoy, J. Vazquez, and R. Beyers, Cobalt-catalysed growth of carbon nanotubes with single-atomic-layer walls, Nature **363**, 605 (1993).
56. T.W. EbbesenandP.M. Ajayan, Large-scale synthesis of carbon nanotubes, Nature **358**, 220 (1992).
57. Y. Maeda, S. Kimura, M. Kanda, Y. Hirashima, T. Hasegawa, T. Wakahara, Y.F. Lian, T. Nakahodo, T. Tsuchiya, T. Akasaka, J. Lu, X.W. Zhang, Z.X. Gao, Y.P. Yu, S. Nagase, S. Kazaoui, N. Minami, T. Shimizu, H. Tokumoto, and R. Saito, Large-scale separation of metallic and semiconducting single-walled carbon nanotubes, J. Am. Chem. Soc. **127**, 10287 (2005).
58. F. Hennrich, R. Krupke, M.M. Kappes, and H.V. Lohneysen, Frequency dependence of the dielectrophoretic separation of single-walled carbon nanotubes, Journal of Nanoscience and Nanotechnolo gy **5**, 1166 (2005).
59. S. Banerjee, T. Hemraj-Benny, and S.S. Wong, Routes towards separating metallic and semiconducting nanotubes, Journal of Nanoscience and Nanotechnology **5**, 841 (2005).
60. J.Q. Li, Q. Zhang, N. Peng, and Q. Zhu, Manipulation of carbon nanotubes using AC dielectrophoresis, Applied Physics Letters **86**, 153116 (2005).
61. D.S. Lee, D.W. Kim, H.S. Kim, S.W. Lee, S.H. Jhang, Y.W. Park, and E.E.B. Campbell, Extraction of semiconducting CNTs by repeated dielectrophoretic filtering, Applied Physics a-Materials Science & Processing **80**, 5 (2005).
62. R.H.M. Chan, C.K.M. Fung, and W.J. Li, Rapid assembly of carbon nanotubes for nanosensing by dielectrophoretic force, Nanotechnology **15**, S672 (2004).
63. S. Baik, M. Usrey, L. Rotkina, and M. Strano, Using the selective functionalization of metallic single-walled carbon nanotubes to control dielectrophoretic mobility, Journal of Physical Chemistry B **108**, 15560 (2004).
64. R. Krupke, F. Hennrich, M.M. Kappes, and H.V. Lohneysen, Surface conductance induced dielectrophoresis of semiconducting single-walled carbon nanotubes, Nano Letters **4**, 1395 (2004).
65. R.C. Haddon, J. Sippel, A.G. Rinzler, and F. Papadimitrakopoulos, Purification and separation of carbon nanotubes, Mrs Bulletin **29**, 252 (2004).
66. C.F. ChouandF. Zenhausern, Electrodeless dielectrophoresis for micro total analysis systems, IEEE Engineering in Medicine and Biology Magazine **22**, 62 (2003).
67. S.W. Lee, D.S. Lee, H.Y. Yu, E.E.B. Campbell, and Y.W. Park, Production of individual suspended single-walled carbon nanotubes using the ac electrophoresis technique, Applied Physics a-Materials Science & Processing **78**, 283 (2004).
68. K. Keren, R.S. Berman, E. Buchstab, U. Sivan, and E. Braun, DNA-templated carbon nanotube field-effect transistor, Science **302**, 1380 (2003).
69. R.B. Weisman, Carbon nanotubes - Four degrees of separation, Nature Materials **2**, 569 (2003).
70. R. Krupke and F. Hennrich, Separation techniques for carbon nanotubes, Advanced Engineering Materials **7**, 111 (2005).

71. D.E. Johnston, M.F. Islam, A.G. Yodh, and A.T. Johnson, Electronic devices based on purified carbon nanotubes grown by high-pressure decomposition of carbon monoxide, Nature Materials **4**, 589 (2005).
72. J. Kong, H.T. Soh, A.M. Cassell, C.F. Quate, and H.J. Dai, Synthesis of individual single-walled carbon nanotubes on patterned silicon wafers, Nature **395**, 878 (1998).
73. J.H. Hafner, M.J. Bronikowski, B.R. Azamian, P. Nikolaev, A.G. Rinzler, D.T. Colbert, K.A. Smith, and R.E. Smalley, Catalytic growth of single-wall carbon nanotubes from metal particles, Chem. Phys. Lett. **296**, 195 (1998).
74. L. Shi, D. Li, C. Yu, W. Jang, D. Kim, Z. Yao, P. Kim, and A. Majumdar, Measuring Thermal and Thermoelectric Properties of One-Dimensional Nanostructures Using a Microfabricated Device, Journal of Heat Transfer **125**, 881 (2003).
75. W. Kim, H.C. Choi, M. Shim, Y. Li, D. Wang, and H. Dai, Synthesis of Ultralong and High Percentage of Semiconducting Single-walled Carbon Nanotubes, Nano Letters **2**, 703 (2002).
76. A.B. Dalton, S. Collins, J. Razal, E. Munoz, V.H. Ebron, B.G. Kim, J.N. Coleman, J.P. Ferraris, and R.H. Baughman, Continuous carbon nanotube composite fibers: properties, potential applications, and problems, J. Mater. Chem. **14**, 1 (2004).
77. M. Zhang, K.R. Atkinson, and R.H. Baughman, Multifunctional carbon nanotube yarns by downsizing an ancient technology, Science **306**, 1358 (2004).
78. Y.L. Li, I.A. Kinloch, and A.H. Windle, Direct spinning of carbon nanotube fibers from chemical vapor deposition synthesis, Science **304**, 276 (2004).
79. M. Motta, Y.-L. Li, I. Kinloch, and A. Windle, Mechanical Properties of Continuously Spun Fibers of Carbon Nanotubes, Nano Lett. **5**, 1529 (2005).
80. K. Hata, D.N. Futaba, K. Mizuno, T. Namai, M. Yumura, and S. Iijima, Water-Assisted Highly Efficient Synthesis of Impurity-Free Single-Walled Carbon Nanotubes, Science **306**, 1362 (2004).
81. Y. Wang, M.J. Kim, H. Shan, C. Kittrell, H. Fan, L.M. Ericson, W.-F. Hwang, S. Arepalli, R.H. Hauge, and R.E. Smalley, Continued Growth of Single-Walled Carbon Nanotubes, Nano Lett. **5**, 997 (2005).
82. M. Oron-Carl, F. Hennrich, M.M. Kappes, H.V. Lohneysen, and R. Krupke, On the electron-phonon coupling of individual single-walled carbon nanotubes, Nano Letters **5**, 1761 (2005).
83. S.M. Bachilo, L. Balzano, J.E. Herrera, F. Pompeo, D.E. Resasco, and R.B. Weisman, Narrow (n,m)-distribution of single-walled carbon nanotubes grown using a solid supported catalyst, J. Am. Chem. Soc. **125**, 11186 (2003).
84. G.H. Jeong, A. Yamazaki, S. Suzuki, H. Yoshimura, Y. Kobayashi, and Y. Homma, Cobalt-filled apoferritin for suspended single-walled carbon nanotube growth with narrow diameter distribution, J. Am. Chem. Soc. **127**, 8238 (2005).
85. L. Tapaszto, K. Kertesz, Z. Vertesy, Z.E. Horvath, A.A. Koos, Z. Osvath, Z. Sarkozi, A. Darabont, and L.P. Biro, Diameter and morphology dependence on experimental conditions of carbon nanotube arrays grown by spray pyrolysis, Carbon **43**, 970 (2005).

86. N. Chopra and B. Hinds, Catalytic size control of multiwalled carbon nanotube diameter in xylene chemical vapor deposition process, Inorg Chim Acta **357**, 3920 (2004).
87. A. Senefelder and J.W. Muller, *The invention of lithography*. (The Fuchs & Lang Manufacturing Company, New York,, 1911), pp.xii.
88. A. Senefelder and N. Ponce, *L'art de la lithographie, ou Instruction pratique contenant la description claire et succincte des differens procedš a suivre pour dessiner, graver et imprimer sur pierre; proceduree d'une histoire de la lithographie et de ses divers progres\0300*. (Chez l'auteur, Munich,, 1819), pp.3 .
89. Raucourt, *A manual of lithography, or, Memoir on the lithographical experiments made in Paris, at the Royal School of the roads and bridges clearly explaining the whole art, as well as all the accidents that may happen in printing, and the different methods of avoiding them*. (Printed for Rodwell and Martin, London, 1820), pp.xix.
90. G.R. Brewerand and J.P. Ballantyne, *Electron-beam technology in microelectronic fabrication*. (Academic Press, New York, 1980), pp.xi.
91. K. Suzuki, S. Matsui, and Y. Ochiai, *Sub-half-micron lithography for ULSIs*. (Cambridge University Press, Cambridge ; New York, 2000), pp.xvii.
92. K.B.A. Valiev, *The physics of submicron lithography*. (Plenum Press, New York, 1992), pp.xi.
93. G.T. Kim, U. Waizmann, and S. Roth, Simple efficient coordinate markers for investigating synthetic nanofibers, Applied Physics Letters **79**, 3497 (2001).
94. G. Binnig, H. Rohrer, C. Gerber, and E. Weibel, Tunneling through a Controllable Vacuum Gap, Applied Physics Letters **40**, 178 (1982).
95. G. Binning, H. Rohrer, C. Gerber, and E. Weibel, Surface Studies by Scanning Tunneling Microscopy, Physical Review Letters **49**, 57 (1982).
96. B. Bhushan, H. Fuchs, and S. Hosaka, *Applied scanning probe methods*. (Springer, Berlin ; New York, 2004), pp.xx.
97. M. Miles, SCANNING PROBE MICROSCOPY: Probing the Future Science **277**, 1845 (1997).
98. R. Wiesendanger, *Scanning probe microscopy and spectroscopy : methods and applications*. (Cambridge University Press, Cambridge England ; New York, 1994), pp.xxii.
99. D.A. Bonnell, *Scanning probe microscopy and spectroscopy : theory, techniques, and applications*, 2nd ed. (Wiley-VCH, New York, 2001), pp.xiv.
100. A. Bachtold, M.S. Fuhrer, S. Plyasunov, M. Forero, E.H. Anderson, A. Zettl, and P.L. McEuen, Scanned Probe Microscopy of Electronic Transport in Carbon Nanotubes, Physical Review Letters **84**, 6082 (2000).
101. O.C. Wells, *Scanning Electron Microscopy*. (McGraw-Hill, New York, 1974).
102. I.A. Glavatskikh, V.S. Kortov, and H.-J. Fitting, Self-consistent electrical charging of insulating layers and metal-insulator-semiconductor structures, Journal of Applied Physics **89**, 440 (2001).
103. J.P. Vigouroux, J.P. Duraud, A. Lemoel, C. Legressus, and D.L. Griscom, Electron Trapping in Amorphous Sio2 Studied by Charge Buildup under Electron-Bombardment, Journal of Applied Physics **57**, 5139 (1985).

104. Y.-F. Chen and M.S. Fuhrer, Electric Field-Dependent Charge-Carrier Velocity in Semiconducting Carbon Nanotubes, Phys. Rev. Lett. **95**, 236803 (2005).
105. S.D. Li, Z. Yu, S.F. Yen, W.C. Tang, and P.J. Burke, Carbon nanotube transistor operation at 2.6 GHz, Nano Letters **4**, 753 (2004).
106. T. Dürkop, S.A. Getty, E. Cobas, and M.S. Fuhrer, Extraordinary Mobility in Semiconducting Carbon Nanotubes, Nano Letters **4**, 35 (2004).
107. Go to www.itrs.org for the most recent International Technical Roadmap for Semiconductors.
108. A. Bachtold, P. Hadley, T. Nakanishi, and C. Dekker, Logic circuits with carbon nanotube transistors, Science **294**, 1317 (2001).
109. A. Javey, H. Kim, M. Brink, Q. Wang, A. Ural, J. Guo, P. McIntyre, P. McEuen, M. Lundstrom, and H.J. Dai, High-kappa dielectrics for advanced carbon-nanotube transistors and logic gates, Nature Materials **1**, 241 (2002).
110. S. Rosenblatt, Y. Yaish, J. Park, J. Gore, V. Sazonova, and P.L. McEuen, High performance electrolyte gated carbon nanotube transistors, Nano Letters **2**, 869 (2002).
111. A. Javey, J. Guo, Q. Wang, M. Lundstrom, and H.J. Dai, Ballistic carbon nanotube field-effect transistors, Nature **424**, 654 (2003).
112. Y. Yaish, J.-Y. Park, S. Rosenblatt, V. Sazonova, M. Brink, and P.L. McEuen, Electrical Nanoprobing of Semiconducting Carbon Nanotubes using an Atomic Force Microscope, Physical Review Letters **92**, 046401 (2003).
113. S.J. Tans, R.M. Verschueren, and C. Dekker, Room temperature transistor based on a single carbon nanotube, Nature **393**, 49 (1998).
114. R. Martel, T. Schmidt, H.R. Shea, T. Hertel, and P. Avouris, Single- and multi-wall carbon nanotube field-effect transistors, Applied Physics Letters **73**, 2447 (1998).
115. S.J. Wind, J. Appenzeller, R. Martel, V. Derycke, and P. Avouris, Fabrication and electrical characterization of top gate single-wall carbon nanotube field-effect transistors, Journal of Vacuum Science & Technology B **20**, 2798 (2002).
116. A. Javey, J. Guo, D.B. Farmer, Q. Wang, D.W. Wang, R.G. Gordon, M. Lundstrom, and H.J. Dai, Carbon nanotube field-effect transistors with integrated ohmic contacts and high-k gate dielectrics, Nano Letters **4**, 447 (2004).
117. K. Eisenbeiser, J.M. Finder, Z. Yu, J. Ramdani, J.A. Curless, J.A. Hallmark, R. Droopad, W.J. Ooms, L. Salem, S. Bradshaw, and C.D. Overgaard, Field effect transistors with SrTiO3 gate dielectric on Si, Applied Physics Letters **76**, 1324 (2000).
118. R.A. McKee, F.J. Walker, and M.F. Chisholm, Crystalline oxides on silicon: The first five monolayers, Physical Review Letters **81**, 3014 (1998).
119. Z. Yu, R. Droopad, J. Ramdani, J.A. Curless, C.D. Overgaard, J.M. Finder, K.W. Eisenbeiser, J. Wang, J.A. Hallmark, and W.J. Ooms, Srontium titanate on Silicon, Material Research Society Symposium Proceedings **567**, 427 (1999).
120. G.Y. Yang, J.M. Finder, J. Wang, Z.L. Wang, Z. Yu, J. Ramdani, R. Droopad, K.W. Eisenbeiser, and R. Ramesh, Study of microstructure in $SrTiO_3$/Si by

high-resolution transmission electron microscopy, Journal of Materials Research **17**, 204 (2002).
121. J. Kong, A.M. Cassell, and H. Dai, Chemical vapor deposition of methane for single-walled carbon nanotubes, Chem. Phys. Lett. **292**, 567 (1998).
123. S. Luryi, Quantum Capacitance Devices, Applied Physics Letters **52**, 501 (1988).
124. N. Kumar, A Calculable Quantum Capacitance, Curr Sci India **68**, 945 (1995).
125. B.G. Wang, X. Zhao, J. Wang, and H. Guo, Nonlinear quantum capacitance, Applied Physics Letters **74**, 2887 (1999).
126. D.L. John, L.C. Castro, and D.L. Pulfrey, Quantum capacitance in nanoscale device modeling, Journal of Applied Physics **96**, 5180 (2004).
127. S. Heinze, M. Radosavljevic, J. Tersoff, and P. Avouris, Unexpected Scaling of the Performance of Carbon Nanotube Transistors, Physical Review B **68**, 235418 (2003).
128. J. Guo, S. Goasguen, M. Lundstrom, and S. Datta, Metal-insulator-semiconductor electrostatics of carbon nanotubes, Applied Physics Letters **81**, 1486 (2002).
129. P.G. CollinsandP. Avouris, Nanotubes for Electronics, Scientific American **283**, 38 (2000).
130. J. CumingsandA. Zettl, Low-Friction Nanoscale Linear Bearing Realized from Multiwall Carbon Nanotubes, Science **289**, 602 (2000).
131. M. Yu, M.J. Dyer, G.D. Skidmore, H.W. Rohrs, X. Lu, K.D. Ausman, J.R.V. Ehr, and R.S. Ruoff, Three-dimensional manipulation of carbon nanotubes under a scanning electron microscope, Nanotechnology **10,** 244 (1999).
132. W. Kim, A. Javey, O. Vermesh, Q. Wang, Y. Li, and H. Dai, Hysteresis Caused by Water Molecules in Carbon Nanotube Field-Effect Transistors, Nano Letters **3**, 193 (2003).
133. J. Melngailis, Focused ion beam technology and applications, Journal of Vacuum Science & Technology B: Microelectronics and Nanometer Structures **5**, 469 (1987).
134. R. Vajtai, B.Q. Wei, Z.J. Zhang, Y. Jung, G. Ramanath, and P.M. Ajayan, Building carbon nanotubes and their smart architectures, Smart Materials and Structures **11**, 691 (2002).
135. P.M. Ajayan, V. Ravikumar, and J.C. Charlier, Surface Reconstructions and Dimensional Changes in Single-Walled Carbon Nanotubes, Physical Review Letters **81**, 1437 (1998).
136. K. Mølhave, D.N. Madsen, S. Dohn, and P. Bøggild, Constructing, connecting and soldering nanostructures by environmental electron beam deposition, Nanotechnology **15**, 1047 (2004).
137. D.N. Madsen, K. Mølhave, R. Mateiu, A.M. Rasmussen, M. Brorson, C.J.H. Jacobsen, and P. Bøggild, Soldering of Nanotubes onto Microelectrodes, Nano Letters **3**, 47 (2003).
138. H. Dai, Controlling nanotube growth, Physics World **13**, 43 (2000).
139. H.T. Soh, C.F. Quate, A.F. Morpurgo, C.M. Marcusa, K. Jing, and D. Hongjie, Integrated nanotube circuits: Controlled growth and ohmic contacting of single-walled carbon nanotubes, Applied Physics Letters **75**, 627 (1999).

140. S. Huang, X. Cai, and J. Liu, Growth of Millimeter-Long and Horizontally Aligned Single-Walled Carbon Nanotubes on Flat Substrates, J. Am. Chem. Soc. **125**, 5636 (2003).
141. J.-Y. Raty, F. Gygi, and G. Galli, Growth of Carbon Nanotubes on Metal Nanoparticles: A Microscopic Mechanism from Ab Initio Molecular Dynamics Simulations, Physical Review Letters **95**, 096103 (2005).
142. Y.H. Wang, M.J. Kim, H.W. Shan, C. Kittrell, H. Fan, L.M. Ericson, W.F. Hwang, S. Arepalli, R.H. Hauge, and R.E. Smalley, Continued growth of single-walled carbon nanotubes, Nano Letters **5**, 997 (2005).
143. S. Dittmer, J. Svensson, and E.E.B. Campbell, Electric field aligned growth of single-walled carbon nanotubes, Current Applied Physics **4**, 595 (2004).
144. I. Utke, A. Luisier, P. Hoffmann, D. Laub, and P.A. Buffat, Focused-electron-beam-induced deposition of freestanding three-dimensional nanostructures of pure coalesced copper crystals, Applied Physics Letters **81**, 3245 (2002).
145. H.W.P. Koops, R. Weiel, D.P. Kern, and T.H. Baum, High-resolution electron-beam induced deposition, Journal of Vacuum Science & Technology B: Microelectronics and Nanometer Structures **6**, 477 (1988).
146. H.W.P. Koops, C. Schossler, A. Kaya, and M. Weber, Journal of Vacuum Science & Technology B: Microelectronics and Nanometer Structures **14**, 4105 (1996).
147. P. Hoffmann, I. Utke, F. Cicoira, B. Dwir, K. Leifer, E. Kapon, and P. Doppelt, Focused Electron Beam Induced Deposition of Gold and Rhodium, Mat. Res. Soc. Symp. Proc. **624**, 171 (2000).
148. G. Boero, I. Utke, T. Bret, N. Quack, M. Todorova, S. Mouaziz, P. Kejik, J. Brugger, R.S. Popovic, and P. Hoffmann, Submicrometer Hall devices fabricated by focused electron-beam-induced deposition, Applied Physics Letters **86**, 042503 (2005).
149. I. Utke, P. Hoffmann, B. Dwir, K. Leifer, E. Kapon, and P. Doppelt, Focused electron beam induced deposition of gold, Journal of Vacuum Science & Technology B: Microelectronics and Nanometer Structures **18**, 3168 (2000).
150. K. Edinger, T. Gotszalk, and I.W. Rangelow, Journal of Vacuum Science & Technology B: Microelectronics and Nanometer Structures **19**, 2856 (2001).
151. A.J. DeMarco and J. Melngailis, Journal of Vacuum Science & Technology B: Microelectronics and Nanometer Structures **19**, 2543 (2001).
152. G.C. Gazzadi and S. Frabboni, Fabrication of 5 nm gap pillar electrodes by electron-beam Pt deposition, Journal of Vacuum Science & Technology B: Microelectronics and Nanometer Structures **23**, L1 (2005).
153. J.-Y. Park, S. Rosenblatt, Y. Yaish, V. Sazonova, H. Üstünel, S. Braig, T.A. Arias, P.W. Brouwer, and P.L. McEuen, Electron-Phonon Scattering in Metallic Single-Walled Carbon Nanotubes, Nano Letters **4**, 517 (2004).
154. B. Gao, A. Komnik, R. Egger, D.C. Glattli, and A. Bachtold, Evidence for Luttinger-Liquid Behavior in Crossed Metallic Single-Wall Nanotubes, Physical Review Letters **92**, 216804 (2004).
155. A. Javey, J. Guo, M. Paulsson, Q. Wang, D. Mann, M. Lundstrom, and H. Dai, High-Field Quasiballistic Transport in Short Carbon Nanotubes, Physical Review Letters **92**, 106804 (2004).

156. S.J. Wind, J. Appenzeller, and P. Avouris, Lateral scaling in carbon-nanotube field-effect transistors, Physical Review Letters **91**, 058301 (2003).
157. S.J. Wind, J. Appenzeller, R. Martel, V. Derycke, and P. Avouris, Vertical scaling of carbon nanotube field-effect transistors using top gate electrodes, Applied Physics Letters **80**, 3817 (2002).
158. J. Guo, S. Datta, and M. Lundstrom, A Numerical Study of Scaling Issues for Schottky Barrier Carbon Nanotube Transistors, IEEE Trans. on Electron Devices **51**, 172 (2004).
159. S.S. Wong, E. Joselevich, A.T. Woolley, C.L. Cheung, and C.M. Lieber, Covalently functionalized nanotubes as nanometre- sized probes in chemistry and biology, Nature **394**, 52 (1998).
160. K. Bradley, J.-C.P. Gabriel, A. Star, and G. Gruner, Short-channel effects in contact-passivated nanotube chemical sensors, Applied Physics Letters **83**, 3821 (2003).
161. R.J. Chen, S. Bangsaruntip, K.A. Drouvalakis, N. Wong Shi Kam, M. Shim, Y. Li, W. Kim, P.J. Utz, and H. Dai, Noncovalent functionalization of carbon nanotubes for highly specific electronic biosensors, PNAS **100**, 4984 (2003).
162. S. Chopra, K. McGuire, N. Gothard, A.M. Rao, and A. Pham, Selective gas detection using a carbon nanotube sensor, Applied Physics Letters **83**, 2280 (2003).
163. J.P. Novak, E.S. Snow, E.J. Houser, D. Park, J.L. Stepnowski, and R.A. McGill, Nerve agent detection using networks of single-walled carbon nanotubes, Applied Physics Letters **83**, 4026 (2003).
164. E.S. Snow, F.K. Perkins, E.J. Houser, S.C. Badescu, and T.L. Reinecke, Chemical Detection with a Single-Walled Carbon Nanotube Capacitor, Science **307**, 1942 (2005).
165. C. Staii, A.T. Johnson, M. Chen, and A. Gelperin, DNA-Decorated Carbon Nanotubes for Chemical Sensing, Nano Lett. **5**, 1774 (2005).
166. L. Valentini, I. Armentano, J.M. Kenny, C. Cantalini, L. Lozzi, and S. Santucci, Sensors for sub-ppm NO[sub 2] gas detection based on carbon nanotube thin films, Applied Physics Letters **82**, 961 (2003).
167. K.A. Williams, P.T.M. Veenhuizen, B.G. de la Torre, R. Eritja, and C. Dekker, Nanotechnology: Carbon nanotubes with DNA recognition, Nature **420**, 761 (2002).
168. M. Radosavljevic, M. Freitag, K.V. Thadani, and A.T. Johnson, Nonvolatile Molecular Memory Elements Based on Ambipolar Nanotube Field Effect Transistors, Nano Lett. **2**, 761 (2002).
169. P. Jarillo-Herrero, S. Sapmaz, C. Dekker, L.P. Kouwenhoven, and H.S.J. van der Zant, Electron-hole symmetry in a semiconducting carbon nanotube quantum dot, Nature **429**, 389 (2004).
170. Cao, Nano Lett. **4**, 745 (2005).
171. L.X. Zheng, M.J. O'Connell, S.K. Doorn, X.Z. Liao, Y.H. Zhao, E.A. Akhadov, M.A. Hoffbauer, B.J. Roop, Q.X. Jia, R.C. Dye, D.E. Peterson, S.M. Huang, J. Liu, and Y.T. Zhu, Ultralong single-wall carbon nanotubes, Nature Materials **3**, 673 (2004).

172. J. Vavro, J.M. Kikkawa, and J.E. Fischer, Metal-insulator transition in doped single-wall carbon nanotubes, Physical Review B (Condensed Matter and Materials Physics) **71**, 155410 (2005).
173. E. Minot, PhD, Cornell, 2004.
174. T. Hertel, R.E. Walkup, and P. Avouris, Deformation of carbon nanotubes by surface van der Waals forces, Physical Review B **58**, 13870 (1998).
175. M.Y. Sfeir, F. Wang, L.M. Huang, C.C. Chuang, J. Hone, S.P. O'Brien, T.F. Heinz, and L.E. Brus, Probing electronic transitions in individual carbon nanotubes by Rayleigh scattering, Science **306**, 1540 (2004).